ROYAL SOCIETY OF CHEMISTRY

REVIEW

Check for updates

Recent advances in perovskite air electrode materials for protonic solid oxide electrochemical cells

Cancan Peng, Xu Han, [iD] Sebete Mabaleha, Philip Kwong, Yao Zheng [iD] * and Xiaoyong Xu [iD] *

Intermediate-temperature proton-conducting solid oxide cells (P-SOCs) have emerged as a promising technology for power generation and hydrogen production. They have gained significant attention due to their lower operating temperature, higher efficiency, better safety and durability and simplified water management over conventional high-temperature oxygen-conducting solid oxide cells (O-SOCs). However, the performance of P-SOC air electrodes is hindered by the sluggish kinetics of oxygen reduction and evolution reactions, necessitating efficient conductivities of H^+, O^{2-}, and e^-. Despite critical advancements, the search for optimal air electrode materials remains challenging. This review provides a comprehensive overview of recent advancements in perovskite materials for P-SOC air electrodes, covering fundamental mechanisms, material development, theoretical modeling, and practical applications. It highlights key progress in reaction kinetics, structure–property relationships, and modification strategies across widely studied perovskite-based systems. Particular emphasis is placed on understanding the correlation between structural characteristics and the electrochemical activity and stability of electrodes, which is essential for the rational design of high-performance, durable P-SOC materials. Additionally, advanced methodologies and mechanistic insights into newly developed air electrode materials are explored, with a focus on the role of theoretical simulations, including artificial intelligence (AI)-driven machine learning (ML) techniques. Finally, perspectives are provided on the future development of high-performance P-SOC air electrodes for industrial applications.

Broader context

As the climate and environmental crisis deepens, the development of clean energy sources has become increasingly critical. Intermediate-temperature proton-conducting solid oxide cells (P-SOCs) show immense potential for power generation and hydrogen production due to their favorable thermodynamics, efficient kinetics, high energy efficiency, low carbon emissions, high tolerance to fuel impurities, modularity, and reversible operation capabilities. In contrast, commercially available oxygen-ion SOCs (O-SOCs) typically operate at temperatures exceeding 750 °C, where the extreme conditions accelerate material degradation and pose significant reliability challenges. To address these issues, researchers are increasingly focusing on P-SOCs, which operate at reduced temperatures of approximately 400–600 °C, enabled by their higher proton conductivity and lower activation energy. Despite these advances, several challenges persist. Even at 500 °C, the air electrode performance of P-SOCs lags that of O-SOCs due to substantial polarization resistance associated with redox reactions at the air electrode. Among potential air electrode materials, perovskite oxides emerge as promising candidates due to their unique electronic structure, superior catalytic properties for oxygen reactions, high thermal stability, and relative ease of synthesis. This review explores cutting-edge P-SOC technologies utilizing perovskite air electrode materials and provides a detailed outlook on future research directions. More broadly, this review provides a valuable reference for designing advanced air electrodes for next-generation P-SOCs.

1. Introduction

Amid the urgent push toward carbon neutrality and the global transition to sustainable development, electrochemical energy conversion and storage technologies have gained substantial

School of Chemical Engineering, The University of Adelaide, Adelaide, South Australia, 5005, Australia. E-mail: yao.zheng01@adelaide.edu.au, xiaoyong.xu@adelaide.edu.au

attention.[1] Their unique capability to integrate renewable energy sources into existing infrastructures offers a powerful solution for reducing reliance on fossil fuels and supporting a resilient energy ecosystem.[2] Among these electrochemical technologies, solid oxide fuel cells (SOFCs) and solid oxide electrolysis cells (SOECs) hold particular promise due to their rapid reaction kinetics, high round-trip efficiency, fuel flexibility, and cost-effectiveness in terms of materials.[3] However, the commercialization of their conventional versions, that rely on

This journal is © The Royal Society of Chemistry 2025

Energy Environ. Sci., 2025, **18**, 4555–4595 | **4555**

oxygen-ion conducting electrolytes, faces substantial challenges associated with high operation temperature, high operational costs, and low reliability detrimental to sustainability. Significant efforts have, consequently, been dedicated to enhancing their sustainability through improvement of cell durability and simplification of management system on oxygen-ion-based SOFCs/SOECs (O-SOFCs/SOECs) by reducing the operating temperatures to manageable levels (400–600 °C).[4,5] However, achieving these lower temperatures without compromising efficiency and performance remains challenging, as lower temperatures can hinder reaction kinetics and reduce ionic conductivity. Proton (H^+) migration is believed to be much faster and has significantly lower activation energy (0.4–0.6 eV) than O^{2-} (>1 eV) as the smaller size and mass of the H^+ allow it easily hop in the lattice.[6,7] Thus, protonic solid oxide electrochemical cells (P-SOCs) hold a greater promise for lower temperature operation.

P-SOCs is a sustainable hydrogen production and power generation technology that integrates economy, efficiency, and safety (Fig. 1(a)). Compared to low-temperature proton exchange membrane systems (PEM, Fig. 1(b1)) which typically operate at 50–80 °C, P-SOCs provide superior thermodynamic performance—including improved catalytic activity, reaction kinetics, and efficiency. Thermal energy compensation ($T\Delta S$) for total energy (ΔH) in P-SOC systems lead to lower electrical energy (ΔG) requirements compared to low-temperature catalysts, as shown by eqn (1).[8–10]

$$\Delta H = \Delta G + T\Delta S \tag{1}$$

Unlike PEM water electrolyzers, P-SOCs facilitate direct production of pure, dry hydrogen in electrolysis mode without a need for external gas purification and dehumidification, thereby making it substantially cost effective. Furthermore, the application of low-temperature PEM systems is constrained by the high cost of platinum group metal catalysts and the stringent raw material requirements, including specific levels of acidity, conductivity, and resistivity. Compared with O-SOFCs (Fig. 1(b2)), water generation at the P-SOFC (Fig. 1(b3)) prevents fuel dilution which contributes to enhanced efficiency and better fuel utilization. High temperatures, according to Stefan–Boltzmann law, increase thermal radiation losses and impose stricter requirements on the cells, interconnectors, and glass sealant to withstand high thermal stresses.[11] Consequently, it is economically imprudent to employ them amid their potential to decreases hydrogen production efficiency, shorten device lifespans, and accelerate degradation, in addition.[12,13] The "intermediate-temperature" P-SOCs with their fairly manageable temperatures are, therefore, better alternatives for efficient hydrogen generation via water electrolysis and power production through fuel cell mode (Fig. 1(c)).[14]

A typical P-SOC includes a dense electrolyte that enables proton conduction and is sandwiched between two porous electrodes: an air electrode and a fuel electrode. The electrolyte supports efficient proton transport, while the porous electrodes fulfil specific roles: the air electrode assists in oxygen reduction and evolution reactions (ORR/OER), and the fuel electrode is involved in the oxidation and reduction of fuel (H_2).[15] It is imperative to develop solutions that are cost-effective, reliable, and long-lasting for P-SOC technology to be effectively applied, the solutions that include finding catalytic materials with high feed conversion and stability at typical elevated reaction temperatures. Consequently, advances through material design, e.g., modifying material structure/composition alongside SOC
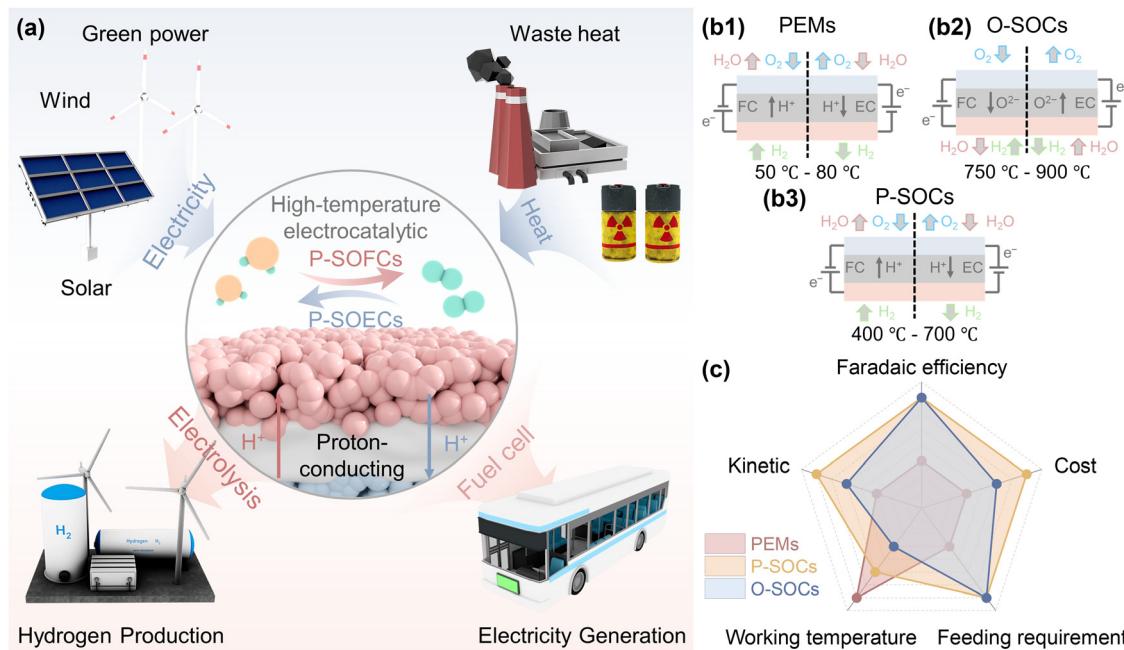

Fig. 1 (a) Schematic of steam electrocatalysis and power generation in P-SOCs. (b) Principal schemes of (b1) PEMs, (b2) O-SOCs, and (b3) P-SOCs. (c) Comparison among low-temperature PEM, intermediate-temperature P-SOCs, and high-temperature O-SOCs.

4556 | Energy Environ. Sci., 2025, 18, 4555–4595

This journal is © The Royal Society of Chemistry 2025

technology design are essential and key to the technology.[16] The simultaneous involvement of O^{2-}, H^+, and e^- in reactions at the air electrode necessitates the corresponding conductivities for all these three charge carriers. However, materials with this unique triple-conductive capability is rare, highlighting their development an imperative.[17,18] Engineering of air electrodes for P-SOCs is highly complex as they play a crucial role in determining overall performance. This complexity has drawn significant attention to their development. The sluggish kinetics of the proton-involved ORR and OER at the air electrode within the range of 400 °C to 700 °C severely limit the electrochemical performance and energy efficiency.[5,19] This effectively necessitates development of more electrocatalytically active and stable materials, currently a major challenge, for sustainable future of P-SOCs.[20,21]

Researchers have dedicated considerable effort to develop advanced air electrode materials for P-SOCs. Metal oxide electrodes (*e.g.*, $LiCoO_2$) are cost-effective and chemically stable but suffer from low electronic conductivity and phase instability in humid or CO_2-rich environments, limiting their long-term performance. Precious metal electrodes (*e.g.*, Pt, Ru) offer exceptional catalytic activity and high electronic conductivity, ensuring fast reaction kinetics, but their high cost, limited availability, and susceptibility to sintering make them less viable for large-scale applications.[5,8] In contrast, perovskite oxides are the dominant choice for air electrodes, owing to their distinctive electronic structure, catalytic properties in oxygen-related reactions, high thermal stability, and ease of raw material synthesis. Over time, studies on perovskite air electrodes have covered various categories, including oxide materials exhibiting dual O^{2-}/e^- conductivity, composites that combine proton conductors with dual O^{2-}/e^- conductors, and newly developed single-phase materials that achieve triple $H^+/O^{2-}/e^-$ conductivity. Herein, the recent progress and challenges associated with perovskite air electrode materials for P-SOCs are systematically reviewed. This review aims to provide an in-depth examination of the recent advancements and ongoing challenges in perovskite air electrode materials for P-SOCs. The state-of-the-art research is categorized into several representative air electrode material types—(Ba/Sr/Pr)$MO_{3-\delta}$-type, $LnBaM_2O_{5+\delta}$-type, and $Ln_2NiO_{4+\delta}$-type—with modification methods spanning bulk structures, interfaces, and composites (Fig. 2). Moreover, the application of advanced computational techniques, particularly artificial intelligence (AI)-driven machine learning (ML), is explored for materials design and theoretical explanation. Commercial considerations and future research directions for P-SOCs air electrodes are also discussed, providing a comprehensive perspective on advancing P-SOCs technology.

2. Perovskite air electrode materials for P-SOCs

P-SOCs represent a significant advancement in the fields of hydrogen production and energy conversion, operating efficiently in both fuel cell (FC) and electrolysis cell (EC) modes. Their operational versatility makes them crucial technologies in sustainable energy systems, leading to great interest in recent years. This section discusses the electrochemical processes involved in hydrogen generation and power generation and then analyzes the role and requirements of perovskite air electrode materials and the corresponding evaluation methods.

2.1. Fundamentals of protonic solid oxide electrochemical cells

A typical P-SOC single cell features a sandwich-like structure with the configuration of air electrode/proton-conducting electrolyte/fuel electrode (Fig. 3(a)). The electrolyte functions as a dense electron-blocking layer, preventing direct combustion between the fuel (H_2) and air (primarily O_2) while facilitating
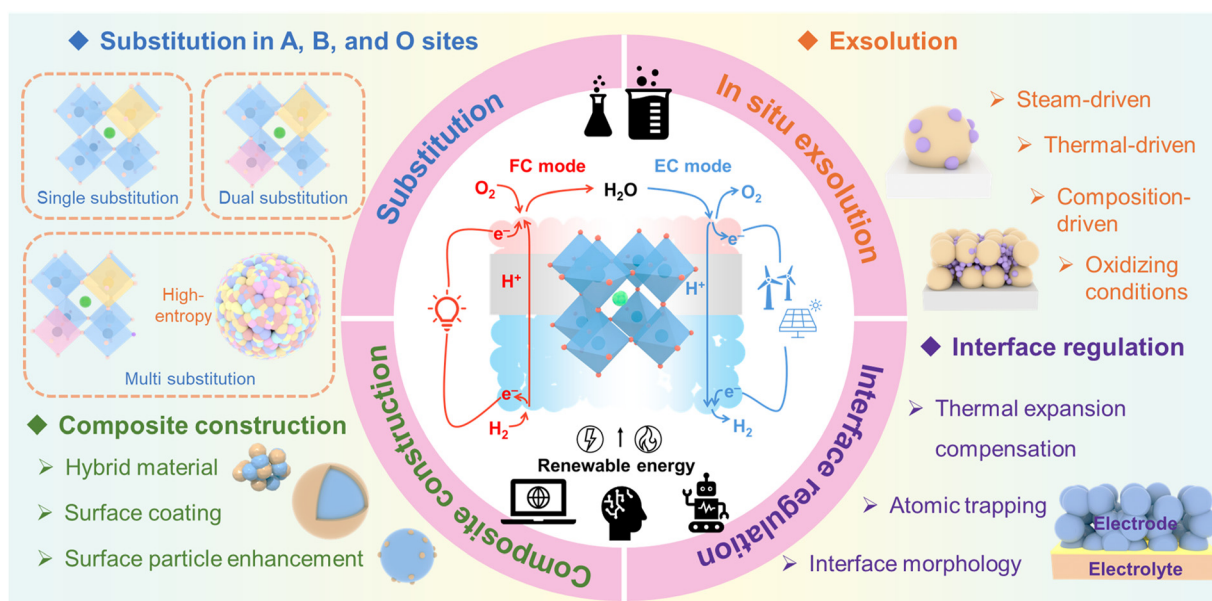

Fig. 2 Typical modifications of perovskite air electrode materials.

This journal is © The Royal Society of Chemistry 2025

Energy Environ. Sci., 2025, **18**, 4555–4595 | **4557**

rapid proton transport.[22,23] The fuel electrode materials comprising of metal (commonly Ni) and electrolyte component is where H_2 generated or consumed.[24] The air electrode serves as a site for ORR or OER.[25] During typical FC operation, electricity is generated through the electrochemical conversion of hydrogen (supplied as fuel on the fuel electrode) which serves as the proton source. Oxygen (from the air) in the air electrode reacts with the proton in the present of electrons (ORR) to form water (eqn (2) – FC mode). In EC mode, steam undergoes electrolysis to produce H_2 by flowing it through the air electrode for OER (eqn (2) – EC mode).[26] When voltage is applied, water decomposes into H^+ and O_2, releasing the electrons. H^+ then migrates through the electrolyte to generate dry H_2 which is then swept off the reaction chamber using inert gas, *e.g.*, N_2 or Ar, while electrons flow through the external circuit to the fuel electrode.[27,28] Eqn (2) and (3) show reactions at both electrodes and Fig. 3(a) exhibits their simple schematic versions.

Air electrode:

$$\frac{1}{2}O_{2,gas} + 2H^+_{electrolyte} + 2e^-_{electrode} \underset{\text{EC mode, OER}}{\overset{\text{FC mode, ORR}}{\rightleftharpoons}} H_2O_{gas} \quad (2)$$

Fuel electrode:

$$H_{2,gas} \underset{\text{EC mode, HER}}{\overset{\text{FC mode, HOR}}{\rightleftharpoons}} 2H^+_{electrolyte} + 2e^-_{electrode} \quad (3)$$
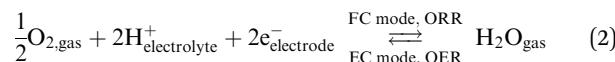
In recent years, new reversible P-SOCs have emerged that can convert fuel into electricity in FC mode and water into hydrogen in EC mode.[29] Unlike prevalent batteries, which face limitations such as self-discharge and high storage costs, the reversibility of reversible P-SOCs potentially enables long-term energy storage by coping with seasonal energy storage adjustments.[30] It operates electrolytically when additional
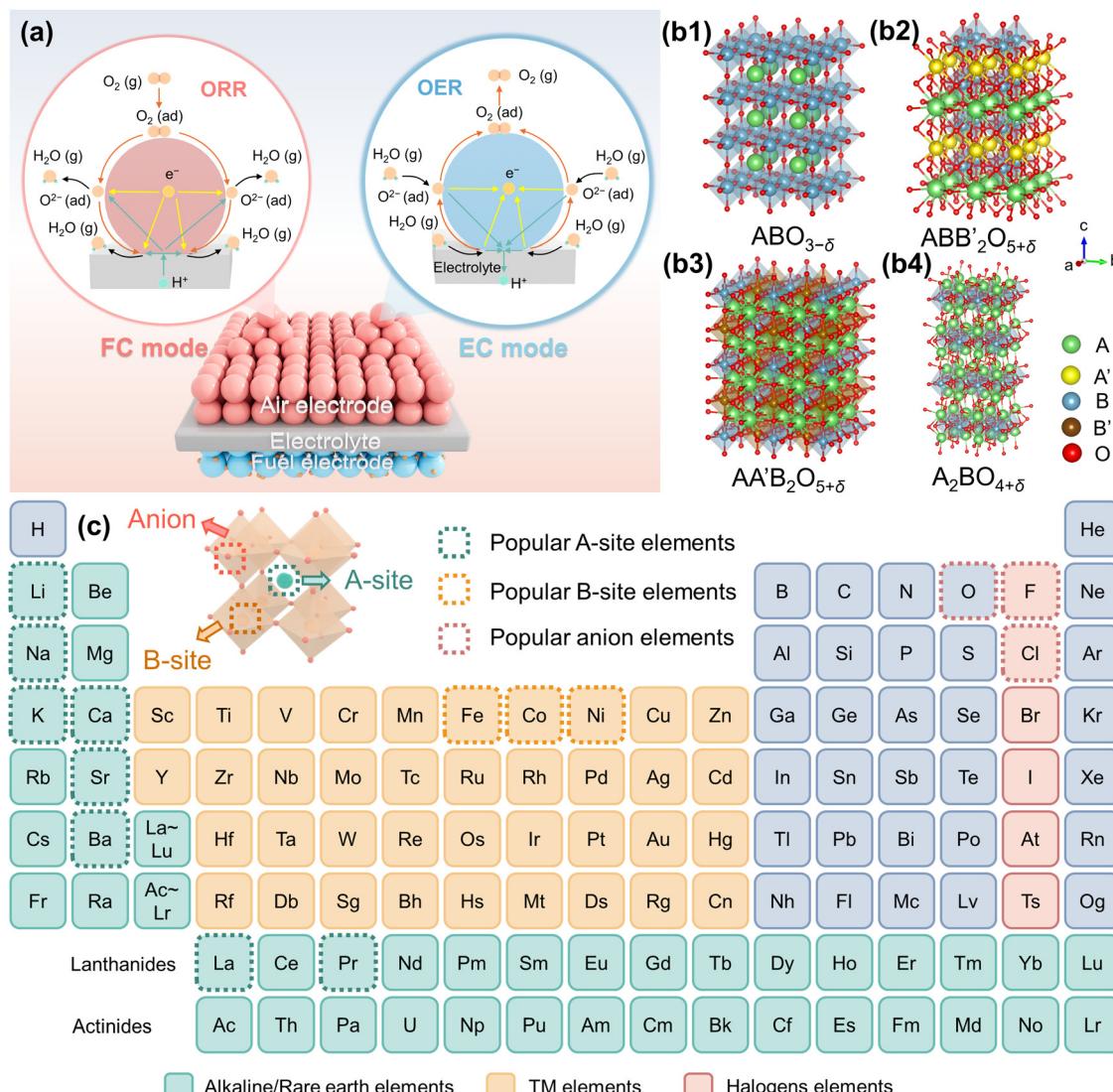

Fig. 3 Fundamentals of perovskite air electrode materials in P-SOCs. (a) Schematic of typical P-SOCs and reactions at the air electrode: ORR reaction and OER reaction (as exemplified by triple-conducting material). (b) Structure of perovskite: (b1) simple perovskite, (b2) and (b3) double perovskite, and (b4) Ruddlesden–Popper phase. (c) Typical elements in perovskite.

baseload power is needed to supplement solar and wind.[31] Since chemical fuels can be stored indefinitely or used immediately as renewable feedstocks in various industrial applications, converting renewable electricity into chemical fuels, aiding the transition to a fully sustainable energy economy.[9] The operational reversibility enables efficient energy storage during periods of renewable electricity oversupply and supports smooth electricity generation, helping to balance supply and demand while expanding the potential for large-scale SOC applications.

2.2. Key properties of perovskites for air electrodes

Essentially, the electrocatalytic process at air electrode of P-SOCs encompasses both the OER and ORR along with hydration reaction, involving the transport of O^{2-}, H^+, e^-. By virtue of multi-conducting materials, the active sites of the proton-involved ORR and OER can cover the entire electrode surface instead of being confined to the electrode/electrolyte interface. Perovskites and perovskite-like structures dominate multiphase conducting materials, sensibly making them widely utilized as air electrodes.[32–34]

2.2.1. Typical structure of perovskites. Typical perovskite has ABO_3, $A_2B_2O_5$, or A_2BO_4 structure (Fig. 3(b)), wherein A is a rare earth metal or alkaline-earth metal, e.g., lanthanide with +2 or +3 valence, and B is a catalytically active transition metal (TM) (Fig. 3(c)). In recent years, elements like Ba, Sr, La, and Pr at the A-site, along with Fe, Co, and Ni at the B-site, have become popular choices in perovskite structures. A-Site ions coordinate with B-site ions in a way that stabilizes the framework through a 12-fold cuboctahedral coordination with oxygen ions, while B-site ions are arranged in a 6-fold coordination with surrounding oxygen anion octahedra.[35] Although B-site ions primarily govern ionic and electronic conduction, A-site ions are crucial for maintaining structural integrity and can influence ionic conduction through interacting with the BO_6 octahedra and O^{2-}.[36,37] Over the past few decades, three primary types of perovskite and perovskite-related oxides with H^+ conduction capabilities have emerged and are extensively utilized as air electrodes in P-SOCs: simple perovskites, double perovskite, and Ruddlesden–Popper (RP) phases.[15,20,36,38]

Simple perovskite ($ABO_{3-\delta}$, Fig. 3(b1)), such as $BaCoO_{3-\delta}$ (BCO), $BaFeO_{3-\delta}$ (BFO), and $SrCoO_{3-\delta}$ (SCO),[39–41] feature rare earth metal or alkaline-earth metal (A site) typically coordinating with oxygen in a 12-fold cuboctahedral arrangement within BO_6 octahedra.[42] TMs (B site) are generally found in sixfold coordination within these octahedra. Double perovskite ($A'AB_2O_{5+\delta}$ and $A_2BB'O_{5+\delta}$, Fig. 3(b2) and (b3)), e.g., $PrBaCo_2O_{5+\delta}$ (PBC), $PrBa_{0.8}Sr_{0.2}Co_2O_{5+\delta}$ (PBSC), and $PrBa_{0.8}Ca_{0.2}Co_{1.95}Pd_{0.05}O_{5+\delta}$[9,43] consist of alternatively stacked layers in the form of $AO|BO_2|A'O|BO_2|$. A is typically a lanthanide ion (+3), e.g., Pr, Nd, Sm, or Gd or alkaline-earth ion (Ba or Sr), and B is often a first-row TM ion or a mixture thereof. The RP phase has general formula $A_{n+1}B_nO_{3n+1}$, where n denotes the number of perovskite-like octahedral layers (Fig. 3(b4)), exemplary materials being La_2NiO_4, $La_3Co_2O_7$, and $La_4Ni_3O_{10}$,[44–46] They exhibit a unique layered structure in which a sequence of $(ABO_3)_n$ perovskite layers is interleaved with rock-salt-type AO layers. $A_2BO_{4+\delta}$ represents the simplest RP structure. The perovskite structure is flexible, adaptable, and tunable. By modifying their properties, e.g., type, composition, phase structures, and synthesis methods, electronic conductivity, ionic conductivity, pore morphology etc., can be altered and subsequently, catalytic performance.[36,37]

2.2.2. H^+, O^{2-}, and e^- conduction mechanism. To identify and develop highly efficient perovskite air electrode materials, it is essential to understand the fundamental principles governing the generation and transport of charge carriers (H^+, O^{2-}, and e^-). The e^- conduction in perovskites is characterized by a polaron hopping mechanism. Electronic charge carriers are transported through the bond network form between B-site cations and oxygen ligands, involving aliovalent TM sites.[47–49] This process, known as small-polaron hopping mechanism (Fig. 4(a)),[50–52] requires that the concentration of multivalent TMs exceeds the bond percolation threshold—a critical region (15–29%) where conductivity markedly increases over a specific range of compositions.[53,54] Below this threshold, dispersed TM sites act as low-energy traps, resulting in a sharp decline in electronic conductivity while they establish low-energy conduction pathways above the percolation threshold.[50,55] The composition at which this critical region emerges can be reduced through ordering, aggregation, or preferential site occupancy.[54,56]
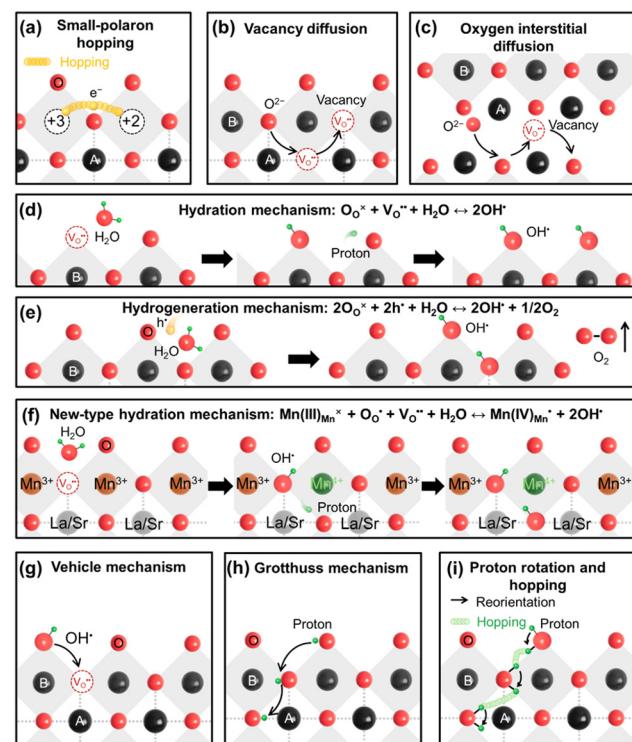
Fig. 4 Charge conduction mechanism (red spheres: O^{2-}; yellow spheres: e^-; green spheres: H^+). (a) e^- conduction mechanism: small-polaron hopping mechanism. O^{2-} conduction mechanisms: (b) vacancy diffusion mechanism and (c) oxygen interstitial diffusion mechanism. H^+ uptake mechanism: (d) hydration mechanism, (e) hydrogeneration mechanism, and (f) new-type hydration mechanism; H^+ transfer mechanism: (g) vehicle mechanism, (h) Grotthuss mechanism, and (i) H^+ reorientation and hopping for Grotthuss mechanism.

This journal is © The Royal Society of Chemistry 2025

Energy Environ. Sci., 2025, **18**, 4555–4595 | **4559**

In perovskite air electrodes for oxidizing atmospheres, O^{2-} diffusion is the primary mode of mass transport. This process is facilitated by O^{2-} vacancies $(V_O^{\bullet\bullet})$ formed through acceptor substitution which create channels for transport. As a result, the mechanism is conveniently referred to as vacancy diffusion (Fig. 4(b)).[57,58] The symbol, "$\bullet\bullet$", represents a net double negative charge while "$\times$" represents a neutral charge. On the surface, these $V_O^{\bullet\bullet}$ capture adsorbed oxygen (O_2) into lattice oxygen $(O_O^\times)$ and release holes $(h^\bullet)$, which then combine with electrons from the fuel electrode to complete the electrical circuit (eqn (4)). In single-structure perovskites, oxygen ion transport *via* the vacancy diffusion mechanism whereas some layered and spinel perovskites utilize the oxygen interstitial diffusion mechanism.[46,59–61] Oxygen ions, in the latter process, migrate through the interstitial spaces between lattice sites (Fig. 4(c)).[55,62]

$$V_O^{\bullet\bullet} + \frac{1}{2}O_2 \leftrightarrow O_O^\times + 2h^\bullet \qquad (4)$$
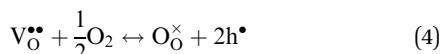
Since protons are not native to oxide lattices, proton uptake and conduction in perovskites heavily relies on hydroxide defects.[63] Three mechanisms have been proposed for proton uptake: hydration mechanism, the hydrogeneration mechanism, and a novel hydration mechanism recently introduced in the literature.[20,64,65] The Kröger–Vink notation describes the primary hydration mechanism, where H_2O decompose into hydroxide ions $(OH^\bullet)$ and H^+, with $OH^\bullet$ filling $V_O^{\bullet\bullet}$ and H^+ bonding with $O_O^\times$ (eqn (5) and Fig. 4(d)). It is predominant when hole concentration is low.[66–68] Hydrogenation mechanism, occurs when oxides have abundant $h^\bullet$, involving a redox reaction that incorporates H^+ and releases O_2, bypassing the need for $V_O^{\bullet\bullet}$ (eqn (6) and Fig. 4(e)).[69–71] Recently proposed hydration mechanism based on $La_{0.7}Sr_{0.3}MnO_{2.95}$ (LSM) suggests that water absorption and desorption are linked to the oxidation of manganese cations $(Mn(III)_{Mn}^\times)$ and the occupation of oxygen holes $(O_O^\bullet)$ by H^+ (eqn (7) and Fig. 4(f)).[72] It further suggests that oxides with significant oxygen vacancy carriers and mixed valence states, like LSM, are effective for proton conduction, making them suitable for applications requiring triple-conducting materials.[72] This theory has since been applied to a wider range of perovskite materials, including those containing cobalt cations, iron oxide ions, and others. Since water adsorption is an exothermic reaction,[73,74] proton conduction becomes the dominant mechanism at lower temperatures, leading to a reduced operating temperature for P-SOCs compared to O-SOCs.

$$V_O^{\bullet\bullet} + H_2O + O_O^\times \leftrightarrow 2OH_O^\bullet \qquad (5)$$

$$H_2O + O_O^\times + 2h^\bullet \leftrightarrow 2OH_O^\bullet + \frac{1}{2}O_2 \qquad (6)$$

$$Mn(III)_{Mn}^\times + V_O^{\bullet\bullet} + H_2O + O_O^\bullet \leftrightarrow Mn(IV)_{Mn}^\times + 2OH_O^\bullet \qquad (7)$$
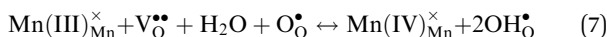
Proton transfer in perovskite can occur through the vehicle and Grotthuss mechanisms, both identified by Kreuer *et al.*[68,75,76] In the vehicle mechanism (Fig. 4(g)), protons move with the O^{2-}, a process constrained by the diffusion rate of O^{2-}, leading to higher activation energy because of the limited mobility of O^{2-} ions.[77,78] Conversely, the Grotthuss mechanism (Fig. 4(h)), which is more commonly accepted, exhibits lower activation energy (<0.4 eV) and involves protons hopping between O^{2-} ions through the alternation of $OH^\bullet$ bonds. This process consists of two steps: (1) reorientation of the $OH^\bullet$ group to reduce the energy barrier for H^+ transfer, and (2) H^+ hopping between O^{2-} ions, aided by protonic defects (Fig. 4(i)).[77,79] In P-SOCs air electrodes, the reaction kinetics are dictated by the balance between electronic and ionic conductivity. High electronic conductivity facilitates the rapid movement of electrons, ensuring that redox reactions occur efficiently at the electrode–electrolyte interface. However, excessive electronic conductivity can reduce the concentration of mobile ionic species, limiting the transport of O^{2-} or H^+. Conversely, high ionic conductivity is essential for sustaining continuous ion diffusion within the electrode bulk, but it may come at the cost of reduced electronic charge transfer, leading to increased polarization resistance and sluggish electrode kinetics.[80,81] However, optimizing one property often compromises the other. For example, $V_O^{\bullet\bullet}$ accelerate ionic transport but can deteriorate the electronic conductivity and weaken structural stability. Therefore, air electrode design is not solely about maximizing one type of conductivity but rather achieving an optimal balance between ionic and electronic transport properties to enhance overall performance.

2.3. Performance-influencing factors

Effective operation of air electrodes relies on several complex substeps including the adsorption/desorption of reactants, generation of active ions, and ion transport within the electrode. High-performance air electrodes should possess both superior ion transfer capabilities and surface catalytic activity to improve reaction kinetics.[82] Key factors influencing performance include oxygen vacancies,[83] hydration abilities,[84] oxygen/proton diffusion capabilities,[85] and surface oxygen ORR and OER activities.[86–89] Optimal performance in P-SOCs requires a balance among these various factors which this section looks into, based on recent advances.

2.3.1. Triple-phase conductivity and catalytic activity. Various perovskite-based air electrodes have been reported for P-SOCs, including conventional electronic conductors,[90,91] mixed ionic–electronic conduction,[92–95] and $H^+/O^{2-}/e^-$ composite conductors.[22,96–98] Despite these advancements, the unsatisfactory ORR and OER keep the technology unsustainable for commercial implementation. Given that ORR and OER in P-SOCs air electrodes primarily involve oxygen/water adsorption/desorption on the electrode surface, reduction of active oxygen/oxidization of water to corresponding active ions (O^{2-}, H^+/hydroxyl), surface and bulk transport of active ions, and generation of water/oxygen with the participation of electrons.[99] Highly efficient triple conduction (O^{2-}, H^+, e^-) is required. Recent advances have exhibited triple-conducting oxides with abundant surface active sites as promising materials for the role, achieving reasonable to high conversions while maintaining structural integrity at elevated temperatures.[100,101] This is partially thanks to significantly enhanced surface and bulk ion generation and transport capabilities of triple-conducting oxides, extending the effective three-phase boundaries and accelerating the electrode

4560 | *Energy Environ. Sci.*, 2025, **18**, 4555–4595

This journal is © The Royal Society of Chemistry 2025

reaction kinetics.[102] OER and ORR can occur over the entire electrode surface (double-phase boundary) rather than being confined to the electrode–electrolyte–gas triple-phase boundary.

Catalytic activity of perovskite influences generation of active ions thus influencing the concentration of charges in system.[63,103–105] The electronic structure is considered crucial for catalytic activity involve the occupancy of the e_g orbitals in surface TMs and the energy levels of the O p-band center.[106,107] To enable rapid surface oxygen-exchange kinetics and unimpeded transport of dissociated oxygen species, to controlling the redox activity of lattice oxygen in perovskites is crucial.[108] This control can generally be achieved through several strategies: substituting A-site with lower-valence cations, inducing oxygen non-stoichiometry, and replacing B-site cations with more electronegative elements.[109–113] The concentration of $V_O^{\bullet\bullet}$ affects the adsorption process of reactants in the proton-involved ORR and OER, thereby affecting the efficiency of the catalytic reaction. For instance, $V_O^{\bullet\bullet}$ concentration connected to B-site cations influences proton uptake in oxides that rely on a hydration mechanism. The micro/nano-structure of perovskite, including its surface area and exposed lattice planes, directly influences surface reaction activity.[105] Lattice planes exhibit higher activity like (110) for $PrO_{1.8}$, high surface area, and large pores, for example, improve the activity through increasing active sites dispersion, reducing the distance for bulk ionic diffusion, etc.[114–116] To advance the industrialization of P-SOCs, it is, therefore, imperative to develop electrodes with excellent triple-phase conductivity and highly electrocatalytic activity for both ORR and OER.[117,118]

2.3.2. Structural symmetry, cations ordering, and defects. High symmetry in crystal structures, such as in cubic perovskites, enhances the mobility of charge carriers (H^+, e^-, and O^{2-}) by facilitating the rotation of corner-sharing oxygen octahedra, minimizing lattice distortion needed for vacancy diffusion, promoting isotropic electron transport and greater atomic orbital overlap, which reduces small-polaron localization and binding energy.[4,32,52,119–121] However, deviations from cubic symmetry, such as transitioning from a cubic phase to orthorhombic, tetragonal, or other non-cubic structures caused by multiple cations at A- and B-sites, can increase O–O bond distances, thereby increasing the hopping distance and reducing mobility of protons. Furthermore, distortions in phase structure can create multiple inequivalent oxygen sites. These variations between adjacent sites may form isolated low-energy sites which can act as traps for protons and $V_O^{\bullet\bullet}$, thereby impeding proton conduction. Additionally, hydration enthalpies differ based on bond distances and local environments, influencing H^+ absorption and conduction. Lower hydration enthalpies generally favor enhanced H^+ conduction contrary to high enthalpies.

In addition to charge-carrier mobility which is influenced by structure of perovskites, structural stability including chemical and thermodynamic stability is significate parameters. Based on the findings of Anthony F. *et al.*, the tolerance factor (t), calculated from the ionic radii of A-site (r_A), B-site (r_B), and O site ions (r_O) (eqn (8)), accurately estimates stability of perovskite structures.[122,123]

$$t = \frac{r_A + r_O}{\sqrt{2}(r_B + r_O)} \quad (8)$$

Perovskite oxides exhibit structural stability within the range of $0.75 < t < 1$ with deviations causing varying degrees of lattice distortion.[124,125] Besides radii, the ordering of cations is also important. A-site ordering improves oxygen transport and hydration, as evidenced by materials like $GdBaMn_2O_{6-\delta}$ and $LaBaCo_2O_{6-\delta}$,[126–128] while B-site ordering and oxygen-vacancy ordering are detrimental to proton conductivity and hydration.[91,129,130]

Structural defects such as vacancies, dislocations, stacking faults, and grain boundaries play a crucial role in determining the electrochemical performance of perovskite air electrodes. $V_O^{\bullet\bullet}$, $h^\bullet$, and protonic defects are particularly important in enhancing ionic and electronic conductivity, as they facilitate O^{2-}/H^+ diffusion and e^- transfer through the electrode bulk. Dislocations, which occur due to lattice mismatches or strain during synthesis and operation, can alter charge carrier mobility and introduce localized stress points that may accelerate material degradation.[131] As an effective strain carrier, stacking faults can directly introduce strain fields and significantly affect the centre position of the d-band, thereby changing the interaction of surface adsorbates. Grain boundaries serve as pathways for ion transport but can also act as barriers that increase resistance, depending on their structure and chemical composition. However, excessive defects formation can lead to crystal lattice distortion and phase instability, negatively impacting electrode durability. Therefore, an ideal perovskite structure features symmetry cubic with a moderate defect concentration, and ordered A-site occupancy, while maintaining disorder in the B-site and anion sublattices to maximize overall conductivity.[132]

2.3.3. Electronegativity. The basicity of O^{2-} is influenced by the electronegativity of cations, which in turn affects proton uptake and transport in oxides.[20] Specifically, a reduction in cation electronegativity tends to enhance the basicity of O^{2-}, leading to increased proton absorption and the equilibrium constant of the hydration reaction.[66] For instance, substituting 50% of Sr (electronegativity = 0.95) in $Sr_{0.5}Ba_{0.5}FeO_{2.5}$ with Ba (electronegativity = 0.85) notably improved the proton concentration (C_H value) to 0.019 mol unit^{-1}, significantly higher than 0.0002 mol unit^{-1} in $SrFeO_{2.5}$.[133] Similarly, the C_H value of $Ba_{0.75}La_{0.25}FeO_{2.53}$ increased from 0.004 to 0.03 mol unit^{-1} when La (electronegativity = 1.1) was replaced with Ba. In $La_{1-x}Sr_xCoO_3$, as the value of x increased from 0.2 to 0.7, the C_H value rose from 0.005 to 0.028 mol unit^{-1}.[91] These changes in hydration capacity are attributed to Ba's lower electronegativity (0.85) compared to Sr (0.95) and La (1.1), which reduces the basicity of O^{2-} and enhances its hydration ability. Additionally, the electronegativity of elements at B-site elements (such as Mn (1.55), Fe (1.83), Co (1.88), Ni (1.91), Zn (1.65), Zr (1.33), and Ce (1.12)) plays a crucial role in improving proton uptake.[134,135] For example, inclusion of Zn at B-site increases the C_H value of $Ba_{0.95}La_{0.05}Fe_{0.8}Zn_{0.2}O_{2.4}$ to 0.1 mol unit^{-1}, compared to just 0.03 mol unit^{-1} without Zn.[91] Similarity, the C_H value of $Ba_{0.5}Sr_{0.5}Fe_{0.8}Zn_{0.2}O_{2.4}$ which features B-site cations with lower electronegativity, is approximately ten times greater than that of $Ba_{0.5}Sr_{0.5}Co_{0.8}Fe_{0.2}O_{2.4}$.

2.3.4. Local environment. Carrier concentrations in electrochemical materials are influenced by the local environment, such as composition, temperature, and atmospheric conditions.

This journal is © The Royal Society of Chemistry 2025

Energy Environ. Sci., 2025, **18**, 4555–4595 | **4561**

At high temperatures, lattice dehydration decreases proton concentration, shifting conductivity towards hole or oxygen-ion conduction.[136,137] Oxidizing environments provide oxygen filling the vacancies, reducing both O^{2-} transport and H^+ uptake while increasing hole concentration.[138] Conductivity can drop significantly under oxidizing conditions and lower temperatures, especially if p-type small polarons are involved, as they have low mobility in the lower temperature. For example, protons dominate as charge carriers in $Ba_{0.85}K_{0.15}ZrO_{3-\delta}$ in pure oxygen up to 600 °C, but at higher temperatures, holes become predominant.[139] The gas environment influences the adsorption and conduction processes in both ORR and OER, and it may also impact the material's durability. The presence of water can initially boost ORR/OER activity but may eventually inhibit oxygen adsorption, leading to degradation and material changes, particularly at lower temperatures where this issue is exacerbated.[140–142] Protons are the main carriers in hydrogen environment, as seen in $BaCe_{0.9-x}Zr_xY_{0.1}O_{3-\delta}$, whereas under oxidizing environment, both protons and oxygen ions are generated and the materials exhibits p-type triple conduction.[143] When exposed to reducing atmosphere, perovskites can experience oxygen release from the lattice, leading to an increase in lattice volume.[144] The reactivity of alkaline earth metals in environments containing water vapor must also be taken to consideration amid their high likelihood to react. Closely managing material properties relative to reaction conditions and environment, in the nutshell, is essential for a successful reaction.[145]

2.4. Evaluation methods

The development of new technologies, such as P-SOCs, typically follows a conventional progression from lab-scale research to pilot plant trials and, eventually to industrial-scale production.[16] The initial lab-scale phase is crucial, as the reliability and accuracy of the experimental data gathered at this stage heavily influence the subsequent stages of technology development. For successful scaling-up and industrialization of sustainable P-SOCs technology, it is essential to have all necessary information well documented and understood. This section gives an overview of electrochemical methods and characterizations based on recent developments, and the recommended research path for air electrodes is summarized in Fig. 5.

2.4.1. Electrochemical evaluation. Catalytic activity of air electrodes in the laboratory is evaluated by determining the area-specific resistances (ASRs) from the electrochemical impedance spectra (EIS) of an air electrode|proton-conducting electrolyte|air electrode symmetrical cell configuration (Fig. 6(a)).
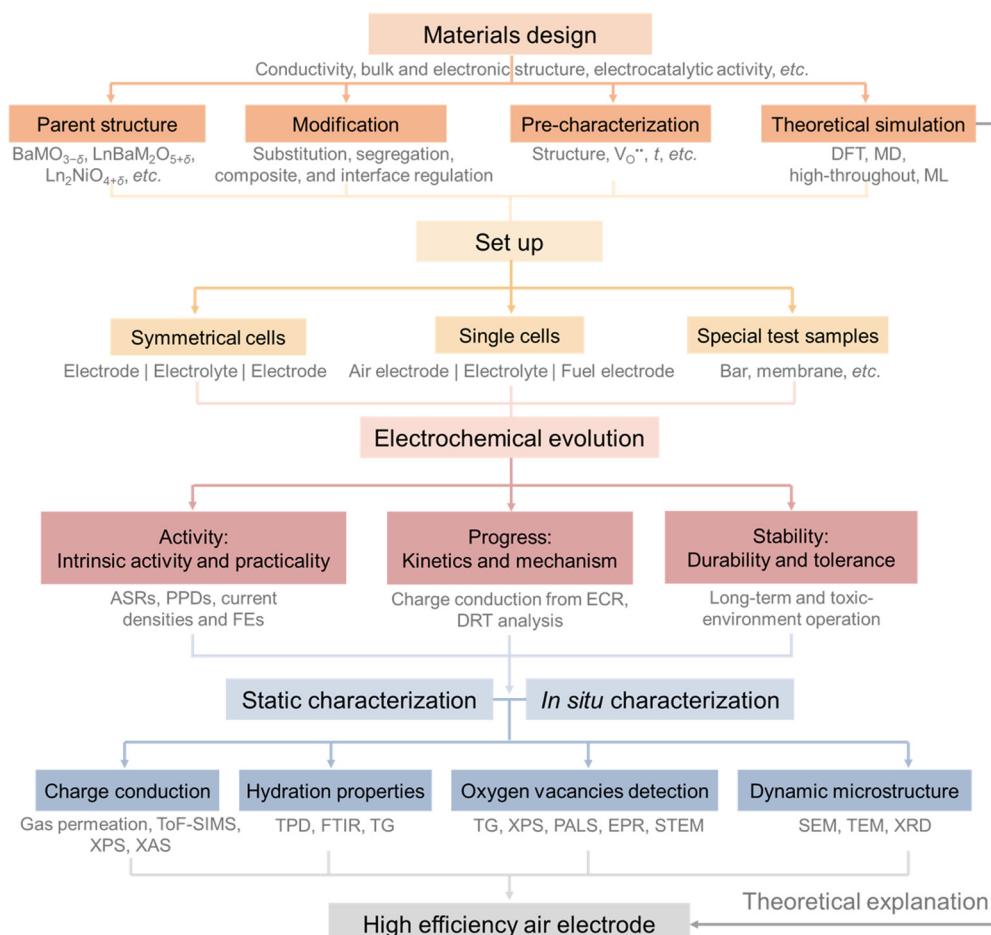

Fig. 5   Recommended research paths for air electrode materials.

4562 | *Energy Environ. Sci.*, 2025, **18**, 4555–4595

This journal is © The Royal Society of Chemistry 2025

In the Nyquist plot, the impedance spectra display distinct, separable depressed arcs associated with different electrode processes.[146,147] The Ohmic resistance (R_{ohm}) comprises the electrode Ohmic resistance, electrolyte resistance, and lead resistance, and R_{ohm} is usually ignored to focus on the performance of electrodes. The difference between intercepts on the real axis of the impedance plot is typically interpreted as electrode polarization resistance (R_p). ASR is calculated by multiplying R_p by the tested areas (A) according to eqn (9).[148,149]

$$ASR = (A \times R_p)/2 \qquad (9)$$

Distribution of relaxation time (DRT) analysis can be performed based on impedance spectra by deconvoluting the EIS response to distinguish overlapping electrode processes and activation energy (E_a) is then determined from the Arrhenius plots (Fig. 6(b)).[153,154] Catalytic activity test is typically performed in dry air or humidified air. Typically, electronic conductivity dominates because the mobility of e^- is several orders of magnitude greater than that of H^+ and O^{2-}.[155,156] The conductive mechanism of the electrode material can be inferred from its conductivity behavior (Fig. 6(c)). For instance, the conductivity of SSNCF material initially rises and then declines with increasing temperature, peaking at 375 °C, which suggests a transition in its conductive mechanism from p-type

to n-type around this temperature. Electrical conductivity relaxation (ECR) measurements, utilizing a 4-probe DC conductivity method, are employed to investigate the chemical diffusivities and surface exchange of H^+ and O^{2-}, as well as electrical conductivity.[83,157] Chemical diffusion coefficient (D_{chem}) and surface exchange coefficient (k_{chem}) are derived by fitting the transient conductivity data to the solution of Fick's second law using a non-linear least-squares fitting approach, based on the Levenberg–Marquardt algorithm.[157] D_{chem} is calculated from the transient conductivity behavior in response to changes in partial pressure. However, for samples with low proton concentrations, the accuracy of ECR measurements may be limited.[31] To isolate the conductivity attributed solely to surface protons, a common approach involves calculating the difference between conductivities measured in wet and dry atmospheres.[158] It is crucial to ensure that the volume conductivity of the target materials remains unaffected by atmospheric conditions.[159]

Electrochemical performance of air electrode materials in SOCs is typically accessed using single cell configuration featuring air electrode|BaZr$_{0.1}$Ce$_{0.7}$Y$_{0.1}$Yb$_{0.1}$O$_{3-\delta}$ (BZCYYb)|Ni-BZCYYb. In P-SOFC, H_2 serves as the fuel on the anode side, while air acts as the oxidant on the cathode side. P-SOEC utilizes steam as the feedstock for H_2 production, on the contrary. The evaluation of electrochemical properties involves measuring polarization resistance (R_p) from EIS test, determining peak power densities (PPDs)
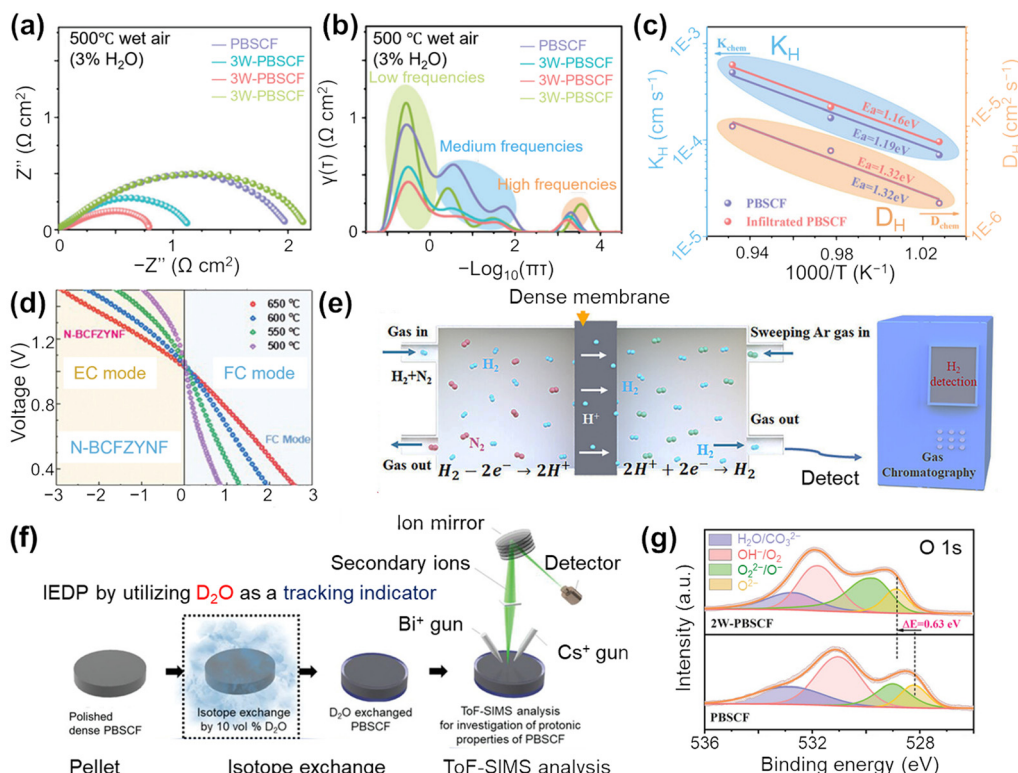
Fig. 6 Recent advances in evaluation methods of air electrode materials. (a) EIS curves, (b) DRT, and (c) k_H and D_H of PBSCF and W infiltrated PBSCF. Reproduced with permission.[150] Copyright 2024, Wiley-VCH. (d) $I-V$ curves of FC and EC modes. Reproduced with permission.[151] Copyright 2024, Wiley-VCH. (e) Scheme for the H_2 permeation test with the proton-conducting membrane. Reproduced with permission.[85] Copyright 2023, Wiley-VCH. (f) Schematic of ToF-SIMS measurement. Reproduced with permission.[152] Copyright 2021, Wiley-VCH. (g) XPS spectra of O 1s. Reproduced with permission.[150] Copyright 2024, Wiley-VCH.

This journal is © The Royal Society of Chemistry 2025

Energy Environ. Sci., 2025, **18**, 4555–4595 | **4563**

and current densities from current density–voltage (*I–V*) curve, and assessing faradaic efficiency (FE) for hydrogen production (Fig. 6(d)). Additionally, air electrode stability tests are performed to monitor any performance degradation. Tests in different atmospheres such as CO_2 or steam are also conducted to assess the chemical stability of the electrode materials.[160] Perovskite air electrodes in P-SOCs are vulnerable to humidity, which can lead to surface hydroxylation, phase decomposition, and a reduction in oxygen ion conductivity, particularly in Ba-containing perovskites. Similarly, CO_2 exposure can cause carbonate formation ($BaCO_3$, $SrCO_3$), which blocks active sites, lowers oxygen vacancy concentration, and degrades ionic transport, especially at moderate to high temperatures (500–800 °C). Currently, to enhance overall catalytic efficiency for practical production, researchers are exploring large-area cells configurations, such as 12×12 cm^2 planar cells and tubular cells, in addition to traditional button cells.[161–163]

2.4.2. Characterization. The characterization of air electrodes encompasses morphology, structure, and composition, often utilizing techniques such as X-ray diffraction (XRD), scanning electron microscopy (SEM), transmission electron microscopy (TEM), and energy-dispersive X-ray spectroscopy (EDS). Alongside conventional assessments, attention to $H^+/e^-/O^{2-}$ three-phase conductivity interactions is crucial for understanding their performance and durability in operational environments.[164]

For protonic conductivity, Shao *et al.* pioneered measuring the H_2 permeation flux through the Pd|Dense $Sr_2Sc_{0.1}Nb_{0.1}Co_{1.5}Fe_{0.3}O_{6-\delta}$ (SSNCF, air electrode)|Pd membrane.[165] Based on this, hydrogen permeation membrane technique was developed. The SSNCF powder materials are directly compressed, followed by sintering in air into dense pellets, H_2 and N_2 are fed into one side of the chamber, respectively. During the experiments, the hydrogen permeation was detected with gas chromatography (GC) (Fig. 6(e)).[85] Time-of-flight secondary ion mass spectrometry (ToF-SIMS) is widely used to quantify proton kinetic properties by analyzing the distribution of deuterium/hydrogen (D/H) isotope concentrations in a quenched air electrode (Fig. 6(f)).[152] For instance, Ren *et al.* combined ToF-SIMS and isotope exchange diffusion profile (IEDP) method to observe stronger distribution of D signal in $BaCo_{0.4}Fe_{0.4}Zr_{0.1}Y_{0.1}O_{2.9-\delta}F_{0.1}$ (BCFZYF) sample than undoped.[166] However, its implementation can be challenging due to high costs and the limited availability of specialized equipment. Additionally, the presence of a hydroxide layer on the air electrode surface can lead to an uneven distribution of the measured ion signals. Protonic conductivity of P-SOCs system *via* vehicle mechanism at low-temperature can be evaluated with a "sandwich-type" membrane conductivity test designed in PEM design. Zhou *et al.* placed a layer of the oxide between two Nafion layers, each in contact with a gas diffusion layer (GDL) electrode that features a standard polymer electrolyte membrane fuel cells Pt/C catalyst-coated membrane under 75 °C.[167] Proton conduction in the Nafion membrane occurs through hydronium ions (H_3O^+), and the conductivity can be calculated using the formula σ (S cm^{-1}) = (h (cm))/(R (ohm) $\times$ S (cm^2)), where h represents the thickness of the oxide layer,

R is the resistance, and S denotes the cross-sectional area through which H_3O^+ migrate.[168–170] The thickness of oxide layer is determined using SEM analysis. This reflects proton conducting *via* vehicle mechanism, as the Grotthuss mechanism does not involve an H_2O vehicle.

Proton conduction relies on the introduction of protons into the crystal lattice *via* hydration reactions. Therefore, beyond directly measuring the protons conductivity of air electrode materials, it is important to investigate their hydration properties, including hydration amount, enthalpy, and entropy. The proton adsorption state at elevated temperatures can be preserved by quenching from high to room temperature of H_2O-temperature-programmed desorption (TPD).[167] *In situ* H_2O-TPD has been employed to assess the hydration levels of materials like $(Ba,Sr,La)(Fe,Co,Zn,Y)O_{3-\delta}$, $(La,Sr)(Co,Mn,Ni)O_3$, and $PrBa_{0.5}Sr_{0.5}Co_{1.5}Fe_{0.5}O_{5+\delta}$ (PBSCF), in both dry and humidified condition, as a function of temperature and pH$_2$O. The hydration ability can also be accessed with Fourier transform infrared spectroscopy (FTIR), which sensitively detects adsorbed water and OH$^\bullet$, OH$^\bullet$ characteristic peak being detected between 3400 cm^{-1} and 3800 cm^{-1}.[171,172] For water uptake with special characteristics such as the absorption of water with proton defect results in a noticeable increase in sample weight, thermogravimetric (TG) analysis is employed to measure the proton defect concentration following water uptake.[73]

The oxygen conduction abilities of air electrode can be measured by oxygen permeation testing which involves measuring O_2 permeation flux detected by GC and ToF-SIMS.[85] Additionally, the oxygen adsorption behavior can be analysis *via* O_2-TPD. Chen *et al.*[151] detected the oxygen desorption properties using O_2-TPD over a temperature range of 50 °C to 800 °C. As temperature increases, the active cations undergo thermal reduction, leading to a decrease in their oxidation state and the concurrent release of oxygen. The optimized air electrode materials exhibit a lower initial desorption temperature (303.9 °C), suggesting enhanced surface oxygen exchange kinetics and migration rates within the perovskite lattice. Additionally, charge transfer within the oxide bulk, along with the formation of H^+ carriers, is often linked to modifications in electronic structure. X-ray photoelectron spectrum (XPS) is a valuable tool for analyzing surface chemical state while X-ray absorption spectroscopy (XAS) provides powerful, element-selective insights into the oxidation states of TMs.[173–175] For example, Zhou *et al.* conducted *operando* hard XAS to observe changes in both the geometric and electronic structures of the air electrodes.[167]

Oxygen vacancies are essential in influencing the catalytic activity of air electrodes, as they function both as active sites for electrochemical reactions and as pathways for ionic transport.[176] Considering the importance of oxygen vacancies, a series of advanced methods have been employed to detect the existence of oxygen vacancies, concentration, and homogeneity.[177] TG analysis and Iodometric titration[178] is carried out to determine the oxygen nonstoichiometry (δ), while XPS is conducted to analyze the chemical state of oxygen in air electrode materials. In the study of Liu *et al.*, O 1s XPS was fitted in four peaks: 529 eV, 530.6 eV, 531.5 eV, and 532.8 eV, corresponding to lattice oxygen (O_{latt}), superoxidative oxygen species (O_2^{2-}/O^-), adsorbed oxygen/

4564 | *Energy Environ. Sci.*, 2025, **18**, 4555–4595

This journal is © The Royal Society of Chemistry 2025

hydroxide (O_2/OH^-), and adsorbed water (H_2O), respectively (Fig. 6(g)).[179] The oxygen vacancy density is directly related to the amount of O_2^{2-}/O^-. Raman spectroscopy is used to investigate the vibrational modes which results in shifts in the Raman spectrum or appearance of new peak.[180,181] Additionally, positron annihilation lifetime spectroscopy (PALS) is carried out to detect oxygen vacancies concentrations based on the positron lifetime.[182] And electron paramagnetic resonance (EPR) test can detect peak intensity for oxygen vacancies by comparing the g-factor.[183] Soft X-ray adsorption spectroscopy (sXAS) can be used to investigate the electronic structures of the O K-edge, which are highly sensitive to oxygen vacancy concentration, electron concentration and hybridized states.[184] Resonant inelastic X-ray scattering (RIXS) can complement XAS measurements by providing detailed information about electron occupancy in d-orbitals and the extent of metal–oxygen hybridization.[185] Scanning transmission electron microscopy (STEM) is employed to analyze the structure of nanomaterials, offering direct atomic-level imaging. Mao *et al.* utilized STEM to examine the atomic scale structure of RuO_2 and identified defects on the materials surface.[186] The stability of air electrode material is assessed using TG methods, along with comparative analyses of morphology, structure, and composition before and after operation. The thermal expansion coefficient (TEC) of air electrode is confirmed by determining lattice parameters through temperature-dependent XRD testing. Advanced *in situ* characterization techniques, such as *in situ* XRD, are employed to monitor the dynamic changes occurring during the operation of the air electrode.[187,188]

3. BaMO$_{3-\delta}$-based perovskite air electrode

Among the diverse family of perovskite oxides, Ba-based simple perovskite BaMO$_{3-\delta}$ (M = Co, Fe) stands out as a particularly attractive option for air electrode in P-SOCs. The larger ionic radii of Ba (1.61 Å) compared to Sr (1.44 Å) and La (1.36 Å), along with its lower electronegativity (Ba: 0.89; Sr: 0.95; Ca: 1.0; La: 1.1; Pr: 1.13, according to Pauling electronegativity), significantly lowers the activation energy required for O^{2-} migration within the crystal lattice.[91,189] This characteristic simultaneously enhances the overall basicity of the oxide ions, promoting adequate conductivity for both oxygen ions and protons. Thus, placing Ba at the A site effectively ensures the transport of carriers. Additionally, its abundant reserves and significantly low cost of Ba ($\sim$1029 USD mt^{-1}) compared to La ($\sim$2621 USD mt^{-1}), Sr ($\sim$8830 USD mt^{-1}), Ca ($\sim$3353 USD mt^{-1}), and Pr ($\sim$73 779 USD mt^{-1}) place it among best candidate for A-site in sustainable industrialization P-SOCs (Prices as of March 2025).[91,190–192] Redox-active TMs like Co and Fe are commonly employed at its B-site for adequate electronic conductivity and enhanced catalytic activity. This chapter gives a comprehensive overview of typical BaMO$_{3-\delta}$-type perovskites used as high-performance air electrode materials (Fig. 7, performance summarized in Table 1).

3.1. BaCoO$_{3-\delta}$-based series

Co, as a B-site cation, is particularly effective for reactions involving electron exchange, such as OER and ORR. This is due to the strong hybridization between the metal 3d and O 2p orbitals,[32,243] as well as the close values of their intra-atomic exchange energy and crystal electric field splitting energy, which leads to small energy differences between their spin states and oxidation states.[244–247] The unique properties combined with the aforementioned of Ba collectively make BaCoO$_{3-\delta}$ (BCO) an exceptional choice for P-SOCs.[193,194,248]

However, BCO's hexagonal structure of BCO restricts charge carrier mobility within the lattice,[249–251] which limit its effectiveness as an independent air electrode.[132,252] It is, consequently, utilized as a reinforcement material, functioning as a
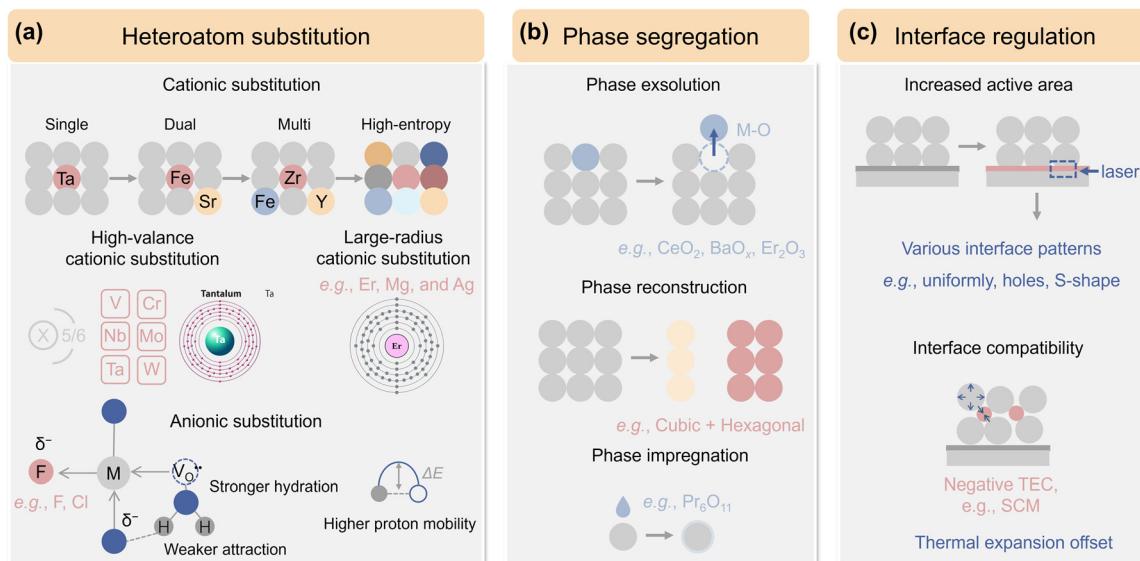

Fig. 7 Schematic of recent advances in BaMO$_{3-\delta}$-type air electrode materials, including (a) heteroatom substitution, (b) phase segregation, and (c) interface regulation.

This journal is © The Royal Society of Chemistry 2025

Energy Environ. Sci., 2025, **18**, 4555–4595 | **4565**

Table 1 Summary of advanced perovskite air electrode materials

Air electrode	ASR (Ω cm^2) at 3% H_2O in symmetrical cell						Single cell				Stability (h)	Ref.
	700 °C	650 °C	600 °C	550 °C	500 °C	450 °C	Electrolyte thickness (μm)	Temperature (°C)	PPD (mW cm^{-2})	Current density at 1.3 V (mA cm^{-2})		
$BaCoO_{3-\delta}$-based air electrode in P-SOCs												
BCO–PBC–LSCF	0.06	0.15	0.25	0.45	0.95		10	550	620	850	300 h (600 °C at -1 A cm^{-2})	193
PBCC–BCO							10	550	660	690	1500 h (600 °C at -1 A cm^{-2})	194
BCO–LSCF	0.04	0.07	0.16	0.35	0.84		10	500	410	500	1150 h (550 °C at -1 A cm^{-2})	195
BCO–BPCFY							70	700	750		85 h (700 °C at 0.7 V)	196
$Ba_{0.95}CoO_3$							15	700	1155			197
BCT		0.12	0.23	0.39	0.65	1.2	10	450	450	250	357 h (550 °C at -1 A cm^{-2})	132
BCFT							24	700	1272		120 h (700 °C at 0.84 V)	198
BSTC		0.08	0.15	0.27	0.5	1.3	6.5					199
BCFZnY450							11.8	450	320			200
PBCF							6	600	1120	1790	100 h (600 °C at 0.7 V)	201
HE-FMCNC	0.057		0.03				10	600	453		120 h (600 °C at 0.2 A cm^{-2})	202
HE-PLNBSCC							6.5	500	660	1100	200 h (500 °C at -0.5 A cm^{-2}, >10% H_2O)	203
HE-PBSLCC	0.06	0.12	0.26	0.75	2.13		10	500	400	280	500 h (600 °C at -0.5 A cm^{-2})	204
HE-BCFZSP			0.15				8	600	680	920	120 h (600 °C at -1.3 A cm^{-2})	205
HE-BCZGZrY							6.5	600	287		100 h (600 °C)	206
BCCY		0.051	0.11	0.20	0.50	1.49	16.1	450	187		800 h (550 °C)	207
BC1.5MN	0.07	0.13	0.24	0.4	1	3	10	550	540	680	1100 h (550 °C at 0.4 A cm^{-2})	208
HE-CBSLCC	0.039	0.088	0.23	0.6	1.65		6	550	1140	840	200 h (600 °C)	209
$BaCoO_{3-\delta}$ derivatives in P-SOCs												
BSCF–BZCY	0.16						15	700	418		100 h (600 °C at 0.2 A cm^{-2})	210
BSCFS600							20	600	566	870		211
LBSCF		0.04	0.42				20	600	350			211
BSCFP							16	500	425	401	240 h (550 °C)	212
BSCFF		0.06	0.12	0.25	0.54	1.41	16	500	302	190	70 h (550 °C at -0.295 A cm^{-2})	213
BSCFC		0.10	0.23	0.53	1.37	4.37	7	650	770	485		213
BSCFE–Er_2O_3		0.11	0.26	0.68	2.13		8	500	525	564	300 h (550 °C at 0.2 A cm^{-2})	179
C/H-BSCF							11	500	1000	1240	500 h (600 °C at -2 A cm^{-2})	214
N-BCFZYNF		0.076	0.165	0.407	1.338	4.783	20	500	374	345	80 h (550 °C at -0.5 A cm^{-2})	151
BCFZYN							10	550	540		400 h (550 °C at 0.2 A cm^{-2})	215
Ag-BCFZY		0.06	0.107	0.242			7	500	398		600 h (500 °C at 0.75 V)	216
KBCFZY			0.43	0.75	0.5			550	770		600 h (600 °C at -4 A cm^{-2} and 0.5 A cm^{-2})	217
BCFZY			0.71				20	500	131			218
S-BCFZY							90	600	350		60 h (600 °C at 0.45 A cm^{-2})	218
L-BCFZY		0.1	0.17	0.28			20	550	900		100 h (600 °C at 0.2 A cm^{-2})	219
SCM-BCFZY			0.35				14	600	655			220
$BaFeO_{3-\delta}$-based air electrode in P-SOCs												
BCF-30Pr	0.039		0.5				16	700	1406		100 h (700 °C at 0.3 A cm^{-2})	221
BCF36							20	600	550		100 h (600 °C at 0.6 V)	222
BCYF							15.8	450	151		450 h (550 °C at 0.2 A cm^{-2})	160
BFZ	0.06	0.25		1.2	3		6	500	670		230 h (600 °C at 1.2 A cm^{-2})	34
BLFZ0.95	0.04	0.07	0.1				10	600	620		250 h (600 °C at 0.9 V)	223
BFCS							8	550	330	610	120 h (600 °C at 0.8 V)	224
2Ru–BCF	0.033	0.2	0.48	1			7	700	1780		200 h (55 °C at 0.7 V)	225

Table 1 (*continued*)

Air electrode	ASR (Ω cm²) at 3% H_2O in symmetrical cell						Single cell					Ref.
	700 °C	650 °C	600 °C	550 °C	500 °C	450 °C	Electrolyte thickness (μm)	Temperature (°C)	PPD (mW cm⁻²)	Current density at 1.3 V (mA cm⁻²)	Stability (h)	
LnBaM₂O₅₊δ-based air electrode in P-SOCs												
PBSCF							15.7	500	420		200 h (600 °C at 0.6 V)	152
PBCsC		0.162	0.275	0.531	1.526		8	500	410	310	200 h (650 °C at 0.5 A cm⁻²)	226
16F-PBSCF		0.2	0.49	1.2			8	550	300			227
PBCIn	0.06	0.13	0.24	0.52	1.47		10	500	480	310	200 h (re P-SOC)	228
PBCCHf₀.₁	0.068	0.107	0.269	0.546			7	550	673	836	200 h (600 °C at ±0.5 A cm⁻²)	229
PBCFN	0.08	0.24	0.8				10	600	723	1036	200 h (650 °C at ±0.5 A cm⁻²)	230
BZC@PBCZ							12	600	551		140 h (600 °C at 0.55 A cm⁻²)	231
DP-BGCO	0.13	0.22	0.4	0.1			20	550	386.4		600 h (600 °C at 0.5 V)	232
BSCFW@PBSCF		0.24	0.24	0.80			10	550	570		240 h (650 °C at 0.7 V)	150
PCO@PBC	0.06	0.1	0.36				10	600	870	2090	100 h (650 °C at ±0.5 A cm⁻²)	233
PFC@PBSCF		0.25	0.3	1.88			10	550	640		100 h (650 °C at 0.5 A cm⁻²)	234
PCNCFO	0.04	0.09	0.81				10	600	910		100 h (650 °C at 0.5 A cm⁻²)	235
PLD-PBSCF			0.18				7	350	500	250	300 h (500 °C at 1 A cm⁻² and −1 A cm⁻²)	236
PBCHf10			0.187	0.374	0.933		7	450	600	400	500 h (600 °C at −0.5 A cm⁻²)	237
PNBFZ							16	550	401		24 h (600 °C at 0.7 V)	238
Others												
PNCu							26	650	280			239
NSTF							20	600	807			167
NSTF0.3@SC							22.5	600	960			167
SCN-PSCN							8	550	600	750	120 h (600 °C at 0.85 V)	240
SCFN			0.2	0.57	2.05		26	500	225	179	290 h (550 °C at 0.8 V)	171
PNC							16	450	640	1600	200 h (600 °C at 0.75 V)	241
PNC-LSCF							30	550	662		200 h (700 °C at 0.8 A cm⁻²)	242

BCO–PBC–LSCF: $BaCoO_{3-\delta}$–$Pr_{1-x}Ba_xCoO_{3-\delta}$–$(La_{0.6}Sr_{0.4})_{0.95}Co_{0.2}Fe_{0.8}O_{3-\delta}$; PBCC–BCO: $PrBa_{0.8}Ca_{0.2}Co_2O_{5+\delta}$–$BaCoO_{3-\delta}$; BCO–LSCF: $BaCoO_{3-\delta}$–$La_{0.6}Sr_{0.4}Co_{0.2}Fe_{0.8}O_{3-\delta}$; BCO–BPCFY: $BaCoO_{3-\delta}$–$Ba_{0.9}Pt_{0.1}Co_{0.7}Fe_{0.2}Y_{0.1}O_{3-\delta}$; BCT: $BaCo_{0.8}Ta_{0.2}O_{3-\delta}$; BCFT: $BaCo_{0.7}Fe_{0.2}Ta_{0.1}O_{3-\delta}$; BSTC: $BaSc_{0.1}Ta_{0.1}Co_{0.8}O_{3-\delta}$; BCFZnY: $BaCo_{0.4}Fe_{0.4}Zn_{0.1}Y_{0.1}O_{3-\delta}$; PBCF: $Pr_{0.5}Ba_{0.5}Co_{0.7}Fe_{0.3}O_{3-\delta}$; HE-FMCNC: $Fe_{0.6}Mn_{0.6}Co_{0.6}Ni_{0.6}Cr_{0.6}O_4$; HE-PLNBSCC: $Pr_{1/6}La_{1/6}Nd_{1/6}Ba_{1/6}Sr_{1/6}Ca_{1/6}CoO_{3-\delta}$; HE-PBSLCC: $Pr_{0.2}Ba_{0.2}Sr_{0.2}La_{0.2}Ca_{0.2}CoO_{3-\delta}$; HE-BCFZGZrY: $BaCo_{0.2}Zn_{0.2}Ga_{0.2}Zr_{0.2}Y_{0.2}O_{3-\delta}$; BCCY: $BaCo_{0.7}(Ce_{0.8}Y_{0.2})_{0.3}O_{3-\delta}$; BC1.5MN: $Ba_2Co_{1.5}Mo_{0.25}Nb_{0.25}O_{6-\delta}$; HE-CBSLCC: $Ce_{0.2}Ba_{0.2}Sr_{0.2}La_{0.2}Co_{0.2}CoO_{3-\delta}$; BSCF-BZCY: $Ba_{0.5}Sr_{0.5}Co_{0.8}Fe_{0.2}O_{3-\delta}$; BSCFP: $BaZr_{0.65}Ce_{0.2}Y_{0.15}O_3$; BCCY: $Ba_{0.5}Sr_{0.5}Co_{0.8}Fe_{0.2}O_{3-\delta}$–$BaZr_{0.1}Ce_{0.7}Y_{0.1}Yb_{0.1}O_{3-\delta}$; BSCFS: $Ba_{0.5}Sr_{0.5}Co_{0.8}Fe_{0.1}Sc_{0.1}O_{3-\delta}$; LBSCF: $La_{0.1}Ba_{0.4}Sr_{0.5}Co_{0.8}Fe_{0.2}O_{3-\delta}$; C/H-BSCF: $Ba_{0.5}Sr_{0.5}(Co_{0.8}Fe_{0.2})_{0.95}P_{0.05}O_{3-\delta}$; BSCFF: $Ba_{0.5}Sr_{0.5}Co_{0.8}Fe_{0.2}O_{3-\delta}$; BSCFF: $Ba_{0.5}Sr_{0.5}Co_{0.72}Fe_{0.18}Er_{0.09}O_{3-\delta}$–$Er_2O_3$; Ag-BCFZY: $Ba_{0.5}Sr_{0.5}Co_{0.8}Fe_{0.2}O_{3-\delta}$–$Ba_4Sr_4(Co_{0.8}Fe_{0.2})_4O_{16-\delta}$; N-BCFZYNF: $Ba(Co_{0.4}Fe_{0.4}Zr_{0.1}Y_{0.1})_{0.95}Ni_{0.05}F_{0.1}O_{2.9-\delta}$; BCFZYN: $Ba_{0.95}(Co_{0.4}Fe_{0.4}Zr_{0.1}Y_{0.1})_{0.95}Ni_{0.05}O_{3-\delta}$; L-BCFZY: laser-engineering $BaCo_{0.4}Fe_{0.4}Zr_{0.1}Y_{0.1}O_{3-\delta}$; BCFZY: $BaCo_{0.4}Fe_{0.4}Zr_{0.1}Y_{0.1}O_{3-\delta}$; S-BCFZY: self-recoverable $BaCo_{0.4}Fe_{0.4}Zr_{0.1}Y_{0.1}O_{3-\delta}$; BLFZ0.95: $Ba_{0.95}La_{0.05}(Fe_{0.8}Zn_{0.2})_{0.95}O_{3-\delta}$; BFCS: $BaFe_{0.6}Ce_{0.2}Co_{0.2}Hf_{0.1}O_{5+\delta}$; 2Ru-BCF: Ru-anchor $BaCo_{0.125}Fe_{0.875}O_{3-\delta}$; PBSCF: $PrBa_{0.5}Sr_{0.5}Co_{1.5}Fe_{0.5}O_{5+\delta}$; PBCsC: $PrBa_{0.9}Cs_{0.1}Co_2O_{5+\delta}$; 16F-PBSCF: $PrBa_{0.5}Sr_{0.5}Co_{1.5}Fe_{0.5}O_{5.84-\delta}Cl_{0.16}$; PBCCHf_{0.1}: $PrBa_{0.8}Ca_{0.2}Co_{1.9}Hf_{0.1}O_{5+\delta}$; PBCFN: $PrBaCo_{1.6}Fe_{0.2}Nb_{0.2}O_{5+\delta}$@$PrBaCo_{1.6}Fe_{0.2}Nb_{0.2-x}O_{5+\delta}$; BZC@PBCZ: $BaZrO_3$@$PrBaCo_{1.92}ZrO_{0.08}O_{5+\delta}$; DP-BGCO: $BaGdCo_2O_{6-\delta}$; BSCFW@PBSCF: $(Ba/Sr)[Co/Fe/W]O_{3-\delta}$@$PrBa_{0.5}Sr_{0.5}Co_{1.5}Fe_{0.5}O_{5+\delta}$; PCO@PBC: $Pr_{0.9}Fe_{0.7}Co_{0.3}O_3$@$PrBa_{0.5}Sr_{0.5}Co_{1.5}Fe_{0.5}O_{5+\delta}$; PFC@PBSCF: $Pr_{0.2}Ce_{0.2}Ni_{0.2}Co_{0.2}Fe_{0.2}O_x$; PLD-PBSCF: pulsed laser deposition $PrBa_{0.5}Sr_{0.5}Co_{1.5}Fe_{0.5}O_{5+\delta}$; PBCHf10: $PrBaCo_{1.9}Hf_{0.1}O_{5+\delta}$; PNBFZ: $Pr_{0.8}Nd_{0.2}BaFe_{1.9}Zn_{0.1}O_{5+\delta}$; LSN: $La_{1.2}Sr_{0.8}NiO_{4+\delta}$; PNCu: $Pr_2Ni_{0.8}Cu_{0.2}O_{4+\delta}$; NSTF: $Na_3Sr_2Ti_4Fe_{1-4}O_{3-\delta}$; NSTF0.3@SC: $Na_{0.3}Sr_{0.7}Ti_{0.1}Fe_{0.9}O_{3-\delta}$@$PrSrCo_{1.8}Nb_{0.2}O_{6-\delta}$; SCN-PSCN: $SrCo_{0.5}Nb_{0.5}O_{3-\delta}$@$PrSrCo_{1.8}Nb_{0.2}O_{6-\delta}$; SCFN: $Sr_{0.9}Ce_{0.1}Fe_{0.8}Ni_{0.2}O_{3-\delta}$; PNC: $PrNi_{0.5}Co_{0.5}O_{3-\delta}$; PNC–LSCF: $Pr_2Ni_{0.5}Co_{0.5}O_{4-\delta}$–$La_{0.6}Sr_{0.4}Co_{0.2}Fe_{0.8}O_{3-\delta}$.

This journal is © The Royal Society of Chemistry 2025

Energy Environ. Sci., 2025, **18**, 4555–4595 | **4567**

modified layer to enhance catalytic activities as well as air electrode durability as in reported *in situ* studies using $PrBa_{0.8}$-$Ca_{0.2}Co_2O_{5+\delta}$, $Ba_{0.9}Pr_{0.1}Co_{0.7}Fe_{0.2}Y_{0.1}O_{3-\delta}$, and $La_{0.6}Sr_{0.4}Co_{0.2}$-$Fe_{0.8}O_{3-\delta}$ (LSCF).[193–196] The BCO coatings additionally mitigate toxic effects of Cr from interconnectors owing to their ability to reduce Cr accumulation on the electrode surface.[253] Recent research efforts have increasingly focused on the bulk structural regulation of BCO for its ultimate autonomy. Atomic substitution techniques have been widely employed to modify their air electrodes phase structure, evolving from single-element substitutions (like Pr, La, Nb, Zn, Sc, *etc.*)[254–262] to double and then multi-element modifications (Fig. 7(a)).[197,259,263,264] Notably, heteroatomic doping with high-valence cations like Nb^{5+}, Ta^{5+},

or Mo^{6+} at the B-site has proven particularly effective. For instance, Kim *et al.* developed cubic $BaCo_{0.8}Ta_{0.2}O_{3-\delta}$ (BCT) by incorporating Ta^{5+}, which has highly corrosion-resistance, stable valence state, and a lower electronegativity (Ta: 1.5; Nb: 1.6; Mo: 2.16).[132] The inclusion of Ta^{5+} stabilized the high-symmetry cubic perovskite structure, significantly enhancing phase stability, conductivity, and catalytic activity for both OER and ORR (Fig. 8(a)). Thus, BCT air electrode achieved remarkable PPD of 2.26 W cm^{-2} at 650 °C and electrolysis current density of 1.1 A cm^{-2} at 1.3 V and 550 °C in P-SOC. Combining two dopants on BCO-type electrodes, like Fe–Ta,[198,264,265] Sm–Zr,[263] and Co–Zr,[266] creates synergistic effects that enhance electrical, ionic, and catalytic properties to levels superior to
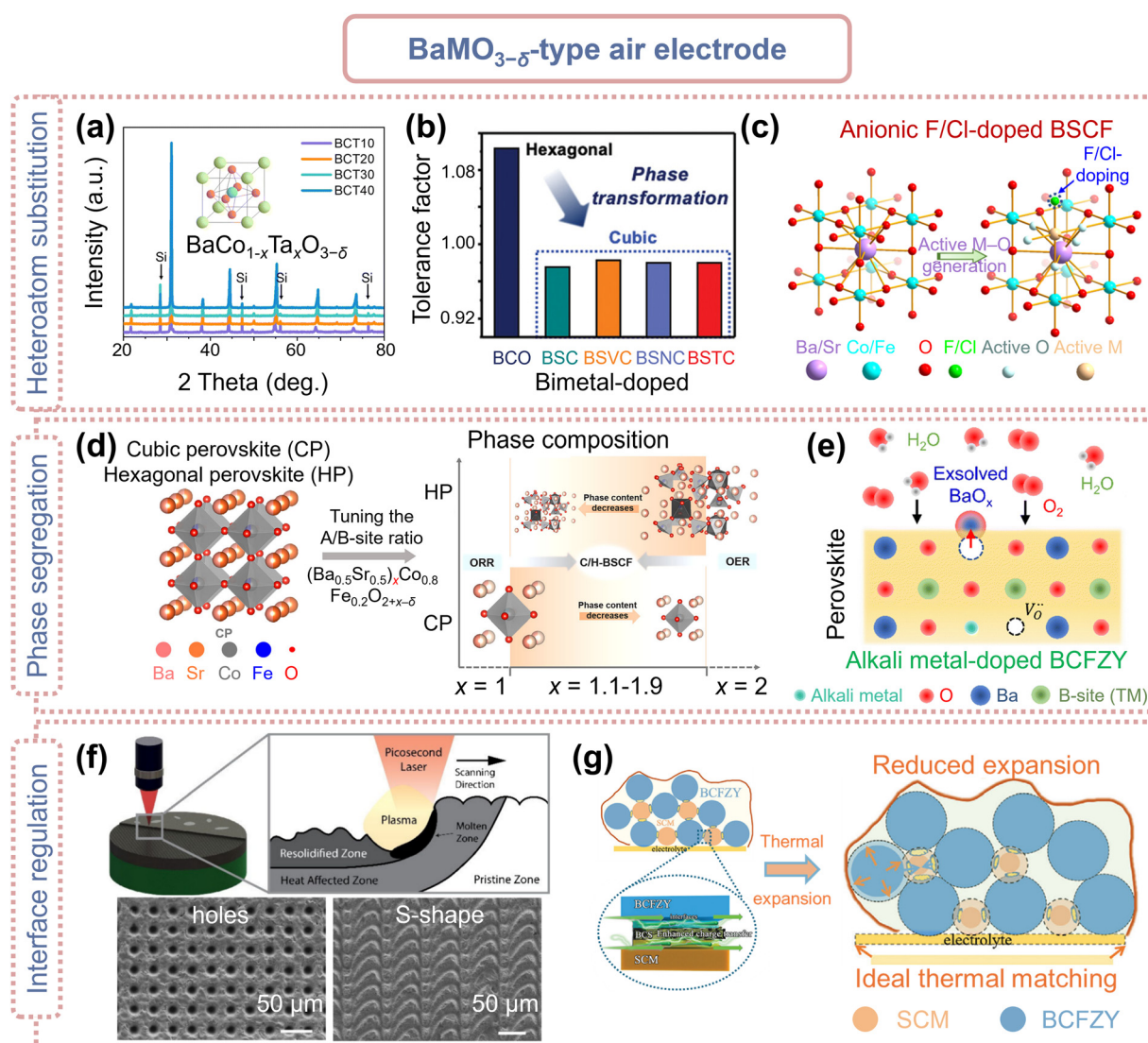
Fig. 8 Recent advances in $BaMO_{3-\delta}$-type air electrode materials. (a) XRD patterns of BCT. Reproduced with permission.[132] Copyright 2023, Royal Society of Chemistry. (b) Tolerance factors of bimetal-doped BMM'C. Reproduced with permission.[199] Copyright 2024, Wiley-VCH. (c) O-site substitution with F/Cl of BSCFF. Reproduced with permission.[213] Copyright 2023, Elsevier. (d) Schematic of phase content-controlled hybrid electrode. Reproduced with permission.[214] Copyright 2024, Springer Nature. (e) Reaction mechanism on the surface of ABCFZY electrode in humidified air. Reproduced with permission. Copyright 2024, Royal Society of Chemistry.[216] (f) Schematic of the laser ablating process and SEM micrographs of holes and S-shape. Reproduced with permission.[219] Copyright 2024, American Chemical Society. (g) Mechanism of the SCM limited reactive bonding "glue". Reproduced with permission.[220] Copyright 2024, Wiley-VCH.

4568 | *Energy Environ. Sci.*, 2025, **18**, 4555–4595

This journal is © The Royal Society of Chemistry 2025

single-element doping. Inspired by dual-doping strategy observed in $SrCoO_3$ for O-SOCs,[267] Kim *et al.* developed Sc–Ta co-doped $BaSc_{0.1}Ta_{0.1}Co_{0.8}O_{3-\delta}$ (BSTC), which stabilizes the cubic perovskite structure.[199] Dual-doping strategy can lead to reduced TEC, improved water uptake, hydration properties, proton transport capabilities, and higher resistance to CO_2 (Fig. 8(b)). The BSTC air electrodes in P-SOCs achieved PPD of 3.15 W cm^{-2} and 2.25 W cm^{-2} at 650 °C and 600 °C in FC mode, and a current density of 4.21 A cm^{-2} at 1.3 V and 650 °C in EC mode. Additionally, Sr–Fe co-doped $Ba_{0.5}Sr_{0.5}Co_{0.8}Fe_{0.2}O_{3-\delta}$ (BSCF) inspired from O-SOCs has seen widespread practical implementation in P-SOCs, which is discussed in detail in Section 3.2. Multi-element doped materials,[200,201] represented by $BaCo_{0.4}Fe_{0.4}Zr_{0.1}Y_{0.1}O_{3-\delta}$ (BCFZY) inspired by electrolyte materials, demonstrate exceptional electrochemical potential and serve as the foundation for numerous research studies. A detailed exploration of BCFZY is presented in Section 3.2. In the design of multi-element substitution strategy, high-entropy design has emerged as a significant topic.[202,268–270] High-entropy perovskite oxides (HEPOs) that contain five or more elements in nearly equimolar ratios exhibit unique properties due to complexity of their localized environments and expected broad adjustability afforded by the "cocktail" effect.[271] Unlike traditional enthalpy-driven phase separation during multi-doping processes,[272,273] HEPOs are stabilized by configurational entropy. In addition, they display a range of unique properties that differ from those of individual oxides including unique crystal structures, enhanced thermal and electronic characteristics, superior catalytic activity, improved electrochemical performance, efficient ionic transport, and distinct thermal expansion behaviors.[203,274–278] He *et al.* developed A-site HEPO $Pr_{0.2}Ba_{0.2}Sr_{0.2}La_{0.2}Ca_{0.2}CoO_{3-\delta}$ (HE-PBSLCC), that effectively combined high conductivity and low TEC of Pr, larger ionic radius of La^{3+}, and chemical stability of Ca^{2+}. This composition led to reduced TEC (23.8×10^{-6} K^{-1}) and effective phase segregation suppress.[187] HE-PBSLCC achieved a PPD of 1.51 W cm^{-2} and a current density of 2.68 A cm^{-2} at 1.3 V at 650 °C, while operational lifetimes exceeding 270-h FC and 500-h EC opeartion.[187] Sun *et al.* constructed B-site HEPO $BaCo_{0.2}Fe_{0.2}Zr_{0.2}Sn_{0.2}Pr_{0.2}O_{3-\delta}$, demonstrating integrated triple-phase conduction, along with exceptional structural stability in high concentration steam.[205,206] In addition to bulk structure modification, atomic substitution can also facilitate the formation of multiple phases within a single bulk grain which is called surface segregation or exsolution. Improper t of certain elements in perovskites can lead to phase separation, resulting in the formation of two or more distinct phases with varying elemental compositions. The self-assembly strategy for creating hybrid electrodes ensures a more homogeneous phases distribution and improved phase contact compared to straightforward physical mixing, thereby reducing energy barriers for charges conduction.[207] Song *et al.* introduced a novel self-assembled $BaCo_{0.7}(Ce_{0.8}Y_{0.2})_{0.3}O_{3-\delta}$ electrode for P-SOFC, incorporating Ce and Y cations into the B-site of the BCO base.[207] This material undergoes self-assembly into nanocomposite consisting of mixed H$^+$/e$^-$ phase, mixed O^{2-}/e$^-$ phase, and the BCO phase during calcination. Enhanced electrochemical activity and ionic transport were achieved due to the synergistic effects of the distinct phases. The composite electrode

$Ba_2Co_{1.5}Mo_{0.25}Nb_{0.25}O_{6-\delta}$ (BC1.5MN), as reported by He *et al.*, undergoes elegant decomposition into BCO and double-perovskite $Ba_{2-x}Co_{1.5-x}Mo_{0.5}Nb_{0.5}O_{6-\delta}$ (DP-BCMN).[208] This transformation enables the electrode to achieve a PPD of 1.17 W cm^{-2} and a current density of 2.04 A cm^{-2} at 1.3 V and 650 °C. A-Site HEPO $Ce_{0.2}Ba_{0.2}Sr_{0.2}La_{0.2}Ca_{0.2}CoO_{3-\delta}$ (HE-CBSLCC), developed by He *et al.*,[209] self-assembles into a three-phase heterostructure under specific processing conditions. This structure includes a deficient $Ce_{0.2-y}Ba_{0.2}Sr_{0.2-x}La_{0.2-x}Ca_{0.2}CoO_{3-\delta}$ (CD-CBSLCC), along with CeO_2, and $La_{0.5}Sr_{0.5}CoO_3$ (LSC) nano-catalysts. Oxygen reduction occurs across the entire air electrode surface, with water formation occurring predominantly at or near CD-CBSLCC. CeO_2 phase can either donate or accept H$^+$, thereby facilitating the ORR and OER kinetics in reversible P-SOCs. The electrode achieves a PPD of 1.66 W cm^{-2} and a current density of 1.76 A cm^{-2} at 1.3 V and 600 °C. They also exhibit excellent operational stability, with 200 h in FC mode, 200 h in EC mode, and 548 h in reversible cycling at 550 °C.

3.2. Eye-catching $BaCoO_{3-\delta}$ derivatives

$Ba_{0.5}Sr_{0.5}Co_{0.8}Fe_{0.2}O_{3-\delta}$ (BSCF) is the center of attention as air electrode material for intermediate temperature O-SOCs.[279,280] In 2004, BSCF made its debut as a cathode for O-SOFCs, achieving remarkable PPDs of 1.01 W cm^{-2} at 600 °C and 402 mW cm^{-2} at 500 °C.[281,282] With mixed conductivity of oxygen ions and a reported proton exchange k value of 3.85×10^{-6} cm s^{-1} at 500 °C in 0.21 atm pO_2, the cubic perovskite BSCF has been identified as air electrode candidate for P-SOCs, too.[158,281] To extend three-phase boundaries and minimize the TEC mismatch between the electrode and electrolyte, BSCF has been composited with various electrolyte materials including $BaCe_{0.7}Zr_{0.1}Y_{0.2}O_{3-\delta}$,[283] $BaCe_{0.9}Y_{0.1}O_3$,[284] $BaCe_{0.8}Zr_{0.1}Y_{0.1}O_{3-\delta}$,[285] $BaCe_{0.4}Zr_{0.4}Y_{0.2}O_{3-\delta}$,[286] $BaZr_{0.65}Ce_{0.20}Y_{0.15}O_3$,[210] and BZCYYb.[287] However, this kind of composite design may compromise the conductivity of air electrode.

Due to the differences in the working principles of P-SOCs and O-SOCs—specifically, that in O-SOCs, water vapor is generated and consumed on the fuel electrode side[288,289]—the electrode materials for the two types of cells are not fully interchangeable.[290] BSCF as P-SOCs air electrode, for example, degrades in high-concentration steam environments.[291] To tackle this problem, atomic substitution (like Sc, La, P) has been attempted to BSCF to stabilize its structure.[211,212,292] Besides cation regulation, anion (O-site) substitution has recently emerged as an effective method for tailoring perovskite air electrode (Fig. 7(a)).[293–295] Anion doping involves substituting lattice oxygen or occupying oxygen vacancies with anions, typically at a stoichiometric ratio of 0.1 to 0.2, thereby modifying the basicity, valence balance, electronegativity, and band structure. To date, halogens (F$^-$ and Cl$^-$) have been used as anionic dopants.[293,296–298] Halogen doping can reduce the basicity of perovskite oxides without compromising their proton conductivity, thus enhancing their chemical stability against acidic gases like CO_2.[293,294,299] Halogen doping can alleviate F$^-$ diffusion from the electrolyte.[300] By introducing halogen, the oxygen vacancy concentration is decreased to maintain electron neutrality, with halogen potentially occupying these vacancies, further lowering vacancy

concentration.[22,293,297] The fluorinated $Ba_{0.5}Sr_{0.5}Co_{0.8}Fe_{0.2}O_{3-\delta}$ (BSCFF) air electrode, for instance at 650 °C, achieved a PPD of 977 mW cm^{-2} and a current density of 950 mA cm^{-2} at 1.3 V.[213] Chen et al. further compared the effects of F$^-$ and Cl$^-$ (Fig. 8(c)), noting that although both have similar valence states, they differ significantly in electronegativity (χ_F: 3.98 > χ_O: 3.44 > χ_{Cl}: 3.16) and ionic radii (F$^-$: 1.33 Å < O^{2-}: 1.40 Å < Cl$^-$: 1.81 Å).[213] The higher electronegativity of F$^-$ enhances its electron-attracting ability, thereby increasing the polarity of the M–O bonds. In P-SOCs, the fluorinated BSCFF air electrode outperformed chlorine $Ba_{0.5}Sr_{0.5}Co_{0.8}Fe_{0.2}O_{2.9-\delta}Cl_{0.1}$ (BSCFC) air electrode in terms of both D_{chem} and k_{chem}. The fluorinated BSCFF also exhibited superior electrochemical performance in both FC (977 mW cm^{-2} vs. 770 mW cm^{-2} for chlorine BSCFC at 650 °C) and EC (950 mA cm^{-2} vs. 485 mA cm^{-2} for chlorine BSCFC at 1.3 V and 650 °C).

Recent research indicates that exceeding material tolerance limits through atomic substitution can form self-assembled multi-phase nanocomposites within a single grain. By carefully controlling concentration of high-valence cations (like Mo^{6+} and W^{6+}) or large-radius cations (like Er, Mg, and Ag), it is possible to customize electrical conductivity, catalytic activity, and structural stability within composite air electrode (Fig. 7(a)).[301,302] Liu et al., for instance, introduced Er into BSCF, which lead to the formation of a nanocomposite featuring predominant cubic perovskite phase ($Ba_{0.5}Sr_{0.5}Co_{0.72}Fe_{0.18}Er_{0.09}O_{3-\delta}$), along with a minor Er_2O_3 component.[179] The Er_2O_3 phase acts as a rapid H$^+$ transport channel, thereby facilitating kinetics of both ORR and OER. While the self-assembly strategy effectively creates strong interactions between hybrid phases, the dynamically changing composition and inconsistent elemental composition render concerns about durability. Liu et al. efficiently controlled the phase contents of hybrid material by adjusting the stoichiometric ratio of A-site and B-site elements, while ensuring the consistency of elemental composition (Fig. 8(d)). The resulting $Ba_{1.5}Sr_{1.5}Co_{1.6}Fe_{0.4}O_{7-\delta}$ consisted of 57.26 wt.% cubic $Ba_{0.5}Sr_{0.5}Co_{0.8}Fe_{0.2}O_{3-\delta}$ (BSCF) and 42.74 wt.% hexagonal $Ba_4Sr_4(Co_{0.8}Fe_{0.2})_4O_{16-\delta}$ (H-BSCF).[214] This hybrid perovskite integrated the superior oxygen activation and conductivity of cubic phase and strong hydration reaction and abundant $V_O^{\bullet\bullet}$ of hexagonal phase. The strengthened interaction between the two phases enhanced the structural and chemical stability.

Since 2013, $BaCo_{0.4}Fe_{0.4}Zr_{0.1}Y_{0.1}O_{3-\delta}$ (BCFZY) has garnered significant attention from researchers, particularly after O'Hayre's group proposed its application in P-SOFC.[103,266] Numerous studies have since been published exploring the chemistry and electrochemistry of BCFZY based on typical compositing (BCFZY–$BaZr_{0.5}Y_{0.5}O_3$ and BCFZY–NiO)[303,304] and substitution (Zn,[305] Mg,[200,306] Sc,[307] Y^{3+},[308] F,[166,213] and A-site-deficient) strategies. Recent investigations on BCFZY increasingly advocate for a dual-functional strategy that combines both bulk and interfacial modifications instead of focusing in one aspect.[195,215,309–311] Chen et al. involved Ni, F co-doped $Ba(Co_{0.4}Fe_{0.4}Zr_{0.1}Y_{0.1})_{0.95}Ni_{0.05}F_{0.1}O_{2.9-\delta}$ (N-BCFZYNE), resulting in precipitation of NiO as a surface catalyst.[151] The higher electronegativity of F$^-$ compared to O^{2-} enhances the polarity of M$-V_O^{\bullet\bullet}-$M bonds, facilitating H$_2$O adsorption on $V_O^{\bullet\bullet}$ and leading to the formation of additional protonic defects. The

F$^-$ introduction decreases the negative charge on lattice oxygen, which in turn weakens the O$\cdots$H interaction, thereby lowering the barrier for proton diffusion. The in situ generated metal oxide catalyst demonstrated enhanced surface reaction activity. This approach achieved improvement both internally (via highly reactive metal–oxygen bonds) and externally (via enabled nano-scale catalysis). Secondary phase nanoparticles (NPs) exsolution can occur under various conditions including water vapor, reducing/oxidizing atmospheres, high temperatures, and electric fields.[215,312] Kim et al. designed steam-induced Ag metal nanocatalysts that functions solely as an electronic conductor, without engaging in proton uptake and diffusion.[216] Building on this, through steam-introduced strategy, Park et al. introduced exsolved BaO_x species in alkali metal ions (Li$^+$, Na$^+$, K$^+$)-doped BCFZY, which served as active sites for ORR/OER (Fig. 8(e)).[217] The driving force for Ba dissolution arises from lattice strain caused by differences in ionic radius and defect interactions, while BaO_x is thermodynamically favored due to its negative Gibbs free energy. In addition to water-induced exsolution, treating $Ba_{0.95}Ag_{0.5}Co_{0.8}Nb_{0.1}Ta_{0.1}O_{3-\delta}$ in a reductive atmosphere[313] and employing voltage-driven exsolution in $Ln_{0.2}Ba_{0.8}Co_{0.7}Fe_{0.3}O_{3-\delta}$[314,315] were also effective in generating NPs catalyst on the surfaces.

Exsolved NPs like Co, Fe, and Ni may slowly dissolve back into the perovskite lattice at elevated temperatures and oxidizing environment.[316,317] Inspired by this, Wang et al. developed a self-recoverable BCFZY (S-BCFZY) electrode for P-SOFCs, featuring a reversible exsolution/dissolution mechanism based on the incorporation of NPs.[218] Under cathodic conditions, the weak Co–O and Fe–O bonds effectively lower the energy barrier for oxygen release, promoting the generation of $V_O^{\bullet\bullet}$ and H$^+$.[218] In anodic conditions, conversely, these weakened TM–O bonds facilitate the segregation of TM atoms (Co^0 and Fe^0) to the perovskite surface, leading to NPs formation and enhanced electrocatalytic activity.[318,319] This multifunctional modification, spanning from the bulk to the surface, positively influences the catalytic process. However, significant differences in the elemental composition of various phases can create thermal strains that are difficult to mitigate and can impair both catalytic activity and stability. Additionally, elemental migration may lead to confusion regarding the actual composition of the hybrid electrode, particularly under high-temperature operational conditions. The exsolution process may inadvertently induce structural modifications in the parent oxide, potentially resulting in the development of RP phases or unwanted cation precipitation.[320] Therefore, the long-term effectiveness of this approach must be thoroughly assessed.

Modifying air electrodes involves not only the electrode materials themselves but also the electrode/electrolyte interface (Fig. 7(c)).[321,322] The blunt surface of perovskite-type proton-conducting electrolytes contributes to interfacial resistances, leading to significant discrepancies in the ASR compared to theoretical values.[323,324] To alleviate interface problem, Zhou et al. developed a novel picosecond laser ablation technique that precisely modifies the electrolyte surface (Fig. 8(f)).[219] This method enables uniform removal of the electrolyte's top layer and creates various patterns, such as cross, S-shape, and hole designs, which increase the effective surface area and establish

4570 | Energy Environ. Sci., 2025, 18, 4555–4595

This journal is © The Royal Society of Chemistry 2025

strong bonding anchors between the BCFZY electrode and BZCYYb electrolyte (Fig. 8(f)). Another interface-controlled approach is to improve the compatibility between electrode materials and electrolytes, especially thermomechanical compatibility.[170,325] Yu *et al.* employed negative thermal expansion oxide $Sm_{0.85}Cu_{0.15}MnO_{3-\delta}$ (SCM with TEC of -5.93×10^{-6} K^{-1}) to offset the thermal expansion of BCFZY.[220] SCM can also strengthen electrode structure and adhesion, and provide acceptable oxygen–reduction–reaction activity (Fig. 8(g)). Thus, this strategy achieves a PPD of 1.455 W cm^{-2} at 700 °C.

3.3. BaFeO$_{3-\delta}$-based perovskite

Given the significant differences in TEC between cobalt-based electrodes and electrolytes (*e.g.*, BSCF: 24.7×10^{-6} K^{-1}; BCFZY: 22.9×10^{-6} K^{-1}; BZCYYb: 10.8×10^{-6} K^{-1}; BZCY: 9.3×10^{-6} K^{-1}),[199,207,326] along with the easy evaporation of Co at elevated temperatures and economic considerations (Co: 66.5 USD kg^{-1}; Fe: 6.7 USD kg^{-1}),[190] Fe emerges as a viable alternative.[160,309,327–329] Fe shares comparable reducibility with Co and, unlike Co-based perovskites, Fe-based perovskites are more easily hydrated and demonstrate improved chemical and thermal stability. The TEC of Fe-based air electrode materials shows enhanced compatibility with proton-conducting electrolytes.[330] Among all Fe-based perovskite, BaFeO$_3$ (BFO) exhibit superior H$^+$ conductivity compared to placing Sr or La at A-site.[32] However, undoped BFO crystallizes in a hexagonal system with low symmetry, poor oxygen ion conductivity, limited tolerance to CO$_2$ and H$_2$O, thereby hindering its effectiveness as a high-performance air electrode.[331–333] To mitigate these challenges, doping (*e.g.*, La, Zn, Sm, Cl, and F) and compositing (*e.g.*, $Sm_{0.2}Ce_{0.8}O_{2-\delta}$–$Ba_{0.5}Sr_{0.5}Fe_{0.8}Sb_{0.2}O_{3-\delta}$) strategies are frequently employed.[332,334–343] Recently, Lu *et al.* combined the two modifications to develop a $BaCe_{0.2}Fe_{0.8}O_{3-\delta}$–$Pr_6O_{11}$ (BCF–30Pr) composite cathode for P-SOFC through impregnation technique.[221] The incorporation of Pr_6O_{11} increased the specific surface area of electrode, reduced the Fe^{3+} content, and enhanced the concentration of $V_O^{\bullet\bullet}$ on the BCF surface. These changes improved both the ORR activity and H$^+$ conduction, leading to a PPD of 1406 mW cm^{-2} at 700 °C.

Inspired by the design of BCFZY, Ce, Zr and Y are also favored dopants in BFO phase.[223,344–346] The Ce-doped $BaCe_{0.36}Fe_{0.64}O_{3-\delta}$ (BCF36) developed by Tong *et al.* features a cubic BFO phase with high O^{2-}/e$^-$ conductivity and an orthorhombic BaCeO$_3$ phase with H$^+$ transfer, thus achieving a PPD of 1525 mW cm^{-2} at 700 °C.[222] By tailoring the Ce/Y ratio in bimetal-doped $Ba(Ce_{0.8}Y_{0.2})_xFe_{1-x}O_{3-\delta}$ (BCYF), a O^{2-}/e$^-$ conducting single-phase transforms into a triple-conducting multi-phase composite.[347] The optimized BCYF nano-composite displayed improved e$^-$ conductivity, ORR activity, thermo-mechanical compatibility, and CO$_2$ tolerance, owing to the strong interaction between O^{2-}/e$^-$ and H$^+$/e$^-$ conducting phases, as well as the optimized dual-phase composition. The $BaCe_{0.16}Y_{0.04}$-$Fe_{0.8}O_{3-\delta}$ cathode demonstrates 450 h durable operation at 550 °C for P-SOFC. Based on BFO, Wang *et al.* combined A- and B-site co-substitution to construct $Ba_{0.875}Fe_{0.875}Zr_{0.125}O_{3-\delta}$ (BFZ) with the formation of $V_O^{\bullet\bullet}$ and $OH_O^{\bullet}$ while retaining structural, which can catch up power outputs of state-of-the-art Co-based BCFZY with a

PPD of 0.67 W cm^{-2} at 500 °C and operational stability of 230 h at 600 °C.[22,34] In the context of BFO-based perovskites used in reversible P-SOCs, Wang *et al.* developed $BaFe_{0.6}Ce_{0.2}Sc_{0.2}O_{3-\delta}$ (BFCS) perovskite characterized by optimized Fe 3d-e$_g$ orbital occupancy, a higher concentration of $V_O^{\bullet\bullet}$, and enhanced Fe^{4+}–O^{2-} interactions which promotes the activation and mobility of lattice oxygen.[224] The BFCS air electrode for P-SOC achieves encouraging output performance in both EC (1.55 W cm^{-2}) and FC (-2.96 A cm^{-2} at 1.3 V) modes at 700 °C. Single-atom catalysis, an emerging technology, has recently been utilized in Fe-based air electrodes. Zhao *et al.* developed a novel air electrode (2Ru-BCF) by integrating single-atom Ru rivets onto $BaCe_{0.125}Fe_{0.875}O_{3-\delta}$ (BCF).[225] The Ru atoms in this structure adopt a distinctive 4-coordinate Ru–O–Fe configuration, which not only promotes reverse hydrogen spillover but also functions as an active site for P-ORR. This optimized 2Ru–BCF cathode (2 wt% Ru) delivers a remarkable PPD of 1.78 W cm^{-2} at 700 °C and demonstrates stable operation over 200 h.

4. LnBaM$_2$O$_{5+\delta}$-based perovskite

LnBaM$_2$O$_{5+\delta}$-based double perovskites feature A-sites occupied by 4f lanthanide and alkaline earth cation Ba. The B-sites host abundant TM cations, including Mn, Fe, Co, and Ni. These materials exhibit enhanced electrochemical performance due to their higher D_{chem} and k_{chem} (performance summarized in Table 1).[348,349] The atomic level of the separation of cations with an alternative layer structure happens due to the large difference in the A or B sites for the two different cations with equal amounts. This chapter offers an in-depth review of typical LnBaM$_2$O$_{5+\delta}$-type perovskites employed as high-performance materials for air electrodes (summarized as Fig. 9).

4.1. LnBaCo$_2$O$_{5+\delta}$-based perovskite

The presence of Co on the B-sites has proven advantageous for both OER and ORR processes. LnBaCo$_2$O$_{5+\delta}$-type double perovskite oxides including $NdBaFe_{2-x}Co_xO_{5+\delta}$,[350] $NdBa_{0.5}Sr_{0.5}Co_{1.5}Fe_{0.5}O_{5+\delta}$,[43,351] and $Ba_{1-x}Gd_{0.8}La_{0.2+x}Co_2O_{6-\delta}$[352,353] with triple-conducting capability, have been demonstrated as effective air electrodes for P-SOCs. Among cobalt-based double perovskites, incorporation of Pr^{2+}/Pr^{3+} in the A site lead to favorable TECs, high conductivity, and strong catalytic activity for OER and ORR reactions.[354,355] Thus, $PrBaCo_2O_{5+\delta}$ (PBC) system is widely studied as air electrode material,[84,231,335,356–366] *e.g.*, famous $PrBa_{0.5}Sr_{0.5}Co_{2-x}Fe_xO_{5+\delta}$ developed by Choi *et al.*, which can achieve PPD exceed 500 mW cm^{-2} at 500 °C and long-term durability under CO$_2$.[84,152] Doping with aliovalent cations including Zn, Ca, Sr, Fe, Ca, and Pd in PBC has been explored to enhance oxygen transport, match TECs with electrolyte, and improve stability.[335,367–371] Xu *et al.* introduced a low-Lewis-acid-strength Cs$^+$-doped $PrBa_{0.9}Cs_{0.1}Co_2O_{5+\delta}$ (PBCsC) electrode (Fig. 9(a)).[226] A-Site dopants with lower acidity facilitate easier H$^+$ uptake (Fig. 10(a)). The polarization of ionic Lewis acid strength at the A site shifts electrons pairs, leading to increased $V_O^{\bullet\bullet}$ and surface exchange kinetics (Fig. 10(b)).[372] PBCsC electrode demonstrates excellent performance in both FC mode (1.66 W cm^{-2}) and EC mode
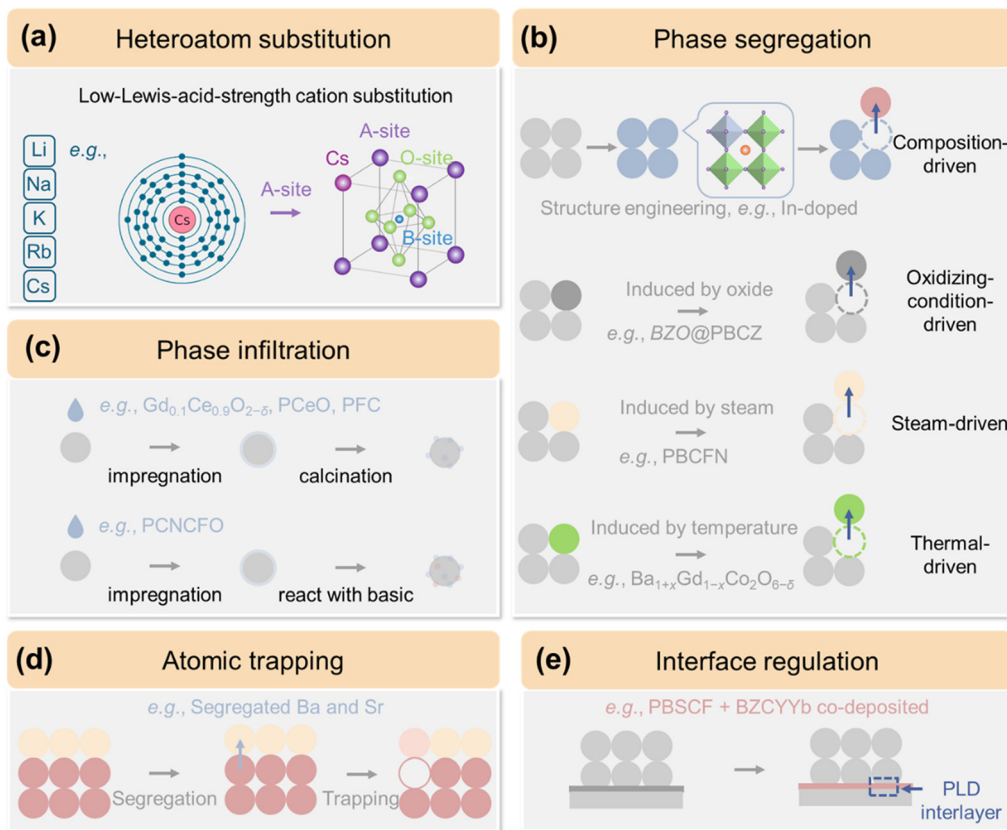
Fig. 9 Schematic of recent advances in LnBaM$_2$O$_{5+\delta}$-type air electrode materials, including (a) heteroatom substitution, (b) phase segregation, (c) phase infiltration, (d) atomic trapping, and (e) interface regulation.

(-2.85 A cm^{-2} at 1.3 V) at 650 °C. Regarding anion substitution, the high electronegativity of F weakens the bond strength between transition-metal 3d orbitals and O 2p states (metal–oxygen bonds) in perovskites, thereby enhancing oxygen surface exchange and diffusion processes.[227,343] The PrBa$_{0.5}$Sr$_{0.5}$Co$_{1.5}$Fe$_{0.5}$O$_{5.84-\delta}$F$_{0.16}$ electrode for P-SOFC exhibits an improved PPD of 510 mW cm^{-2} at 600 °C.[227] The long-term durability of perovskite electrodes is significantly influenced by the alkaline earth cations (e.g., Ba and Sr) surface segregation,[373] which stems from composition, temperature, acidity or alkalinity, oxygen/steam partial pressure, and polarization current (Fig. 9(c)).[374] The resultant insulating impurities impede the transfer of electrons and ions in proton-involved ORR and OER processes.[374–376] Researchers explored various strategies to mitigate the negative impacts of segregation, represented by phase structure engineering.[18,26,313] Du et al. utilized In^{3+}, which has a large ionic radius (In^{3+} = 0.8 Å, Co^{3+} = 0.545 Å, and Co^{4+} = 0.53 Å) and is recognized for enhancing sinterability and stability in proton-conducting electrolytes,[377–379] to develop a PrBaCo$_{1.9}$In$_{0.1}$O$_{5+\delta}$ (PBCIn) air electrode.[228] The composition-driven formation of composite phases in the PBCIn electrode consists of a primary phase of deficient PrBa$_{0.95}$Co$_{1.85}$In$_{0.09}$O$_{5+\delta}$ and a secondary cubic perovskite phase BaCo$_{0.85}$In$_{0.15}$O$_{3-\delta}$.[228] The synergistic effect of these two phases enables PBIn to show 2.25 W cm^{-2} in FC mode, -4.41 A cm^{-2} at 1.3 V in EC mode at 700 °C and 210 h durability under 600 °C. High-valence cation Hf^{4+}-doped PrBa$_{0.8}$Ca$_{0.2}$Co$_{1.9}$Hf$_{0.1}$O$_{5+\delta}$

(PBCCHf$_{0.1}$) naturally is regarded as double perovskite backbone, PrBa$_{0.8-x}$Ca$_{0.2}$Co$_{1.9}$Hf$_{0.1-x}$O$_{5+\delta}$ (PBCCHf$_{0.1-x}$), with nano-sized BaHfO$_3$ forming on the surface (Fig. 10(c)).[229,380,381] The in situ exsolution of BaHfO$_3$ NPs induces additional oxygen vacancies on the surface of Ba- and Hf-deficient PBCCHf$_{0.1-x}$. Xu et al. demonstrated that Fe and Nb co-doped PBC form a heterostructure under steam-driven conditions (Fig. 10(d)), featuring in situ exsolved Nb-deficient PrBaCo$_{1.6}$Fe$_{0.2}$Nb$_{0.2-x}$O$_{5+\delta}$ (Nb-deficient PBCFN) on a double perovskite backbone, PrBaCo$_{1.6}$Fe$_{0.2}$Nb$_{0.2}$O$_{5+\delta}$ (Nb-rich PBCFN).[230] The combination of in situ formed Nb-deficient NPs and the Nb-rich parent perovskite significantly faster surface exchange process, enhancing both catalytic activity (PPD of 1.059 W cm^{-2} and current density of 2.148 A cm^{-2} at 1.3 V at 650 °C) and durability (200 h). In situ exsolution of BaZrO$_3$ NPs from the host PrBaCo$_{1.92}$Zr$_{0.08}$O$_{5+\delta}$ (BZO@PBCZ) occurs under oxidizing conditions, facilitating the liberation Ba and Zr cations and forming proton transfer channels (Fig. 10(e)),[231] Thereby accelerating the oxygen reduction catalytic activity. Cation-nonstoichiometric Ba$_{1+x}$Gd$_{1-x}$Co$_2$O$_{6-\delta}$ spontaneously grows into the double perovskite BaGdCo$_2$O$_{6-\delta}$ (BGCO), anchored by BCO NPs under thermal-driven conditions (Fig. 10(f)).[232] The synergy between the two components leads to exceptional performance, with the mixed O^{2-}/e$^-$-conducting perovskite-derived oxide exhibiting superior catalytic activity for the ORR, while the double perovskite structure enhances bulk H$^+$ conductivity, thus increasing the number of available reaction sites.

4572 | Energy Environ. Sci., 2025, **18**, 4555–4595

This journal is © The Royal Society of Chemistry 2025

Surface decoration of nano-catalysts, typically on the order of tens of nanometers, on cathodes through a cost-effective infiltration process has garnered considerable attention (Fig. 9(c)).[383,384] The porous skeleton facilitates significant electronic and ionic conductivity and the infiltrated coating enhances both catalytic activity and durability, e.g., $Gd_{0.1}Ce_{0.9}O_{2-\delta}$-infiltrated PBC.[385] Pei et al. incorporated a fluorite-based $Pr_{0.1}Ce_{0.9}O_{2+\delta}$ (PCeO) catalyst coating on PBC skeleton, demonstrating a much-reduced polarization resistance (reduced 58%), improved performance (PPD of 1.21 W cm^{-2} at 650 °C), and Ba segregation inhibition.[233] The infiltration method promotes a well-mixed combination of raw materials at the atomic level, allowing for lower synthesis temperatures, and extends the length of the three-phase boundaries,[386–388] where the electron, ion, and gas phases converge. For instance, at 700 °C, the $Pr_{0.9}Fe_{0.7}Co_{0.3}O_3$ (PFC) coating formed on PBSCF base after infiltration resulted in substantial performance improvements and markedly poisoning (including Cr and steam) tolerance (Fig. 10(g)).[234,389,390] Besides creating a surface coating, the infiltrated solution may interact with the perovskite matrix. Gao et al. designed a multi-

cationic oxide nano-catalyst, $Pr_{0.2}Ce_{0.2}Ni_{0.2}Co_{0.2}Fe_{0.2}O_x$ (PCNCFO), anchored on the surface of the PBC electrode via infiltration (Fig. 10(h)).[235] The cerium oxide in the PCNCFO coating reacts dynamically with Ba segregated from the PBC, forming $BaCeO_3$, which stabilizes the PBC phase structure, enhances proton conduction and transfer, and accelerate oxygen surface exchange. Consequently, the PCNCFO-coated PBC cathode achieved a high PPD of 1.31 W cm^{-2} at 650 °C.

Recently, an innovative method involving atomic trapping at high temperatures has been effective in modifying the surface chemistry of perovskites to tackle segregation.[391–393] In the $(La_{0.6}Sr_{0.4})_{0.95}Co_{0.2}Fe_{0.8}O_{3-\delta}$ perovskite, strontium atoms can be selectively extracted using an acidic MoO_4 trap, forming inactive $SrMoO_4$, which enhances durability.[394] Building on this atomic capture approach, Zhao et al. introduced liquid-phase dispersible $(NH4)_{10}W_{12}O_{41}$ onto the PBSCF surface, allowing for the capture of segregated barium and strontium cations from the PBSCF matrix (Fig. 9(d)).[150] This process results in the formation of a heterostructure $(Ba/Sr)(Co/Fe/W)O_{3-\delta}$ (BSCFW)@PBSCF (Fig. 10(i)). The novel P-SOFC cathode achieved remarkable performance,
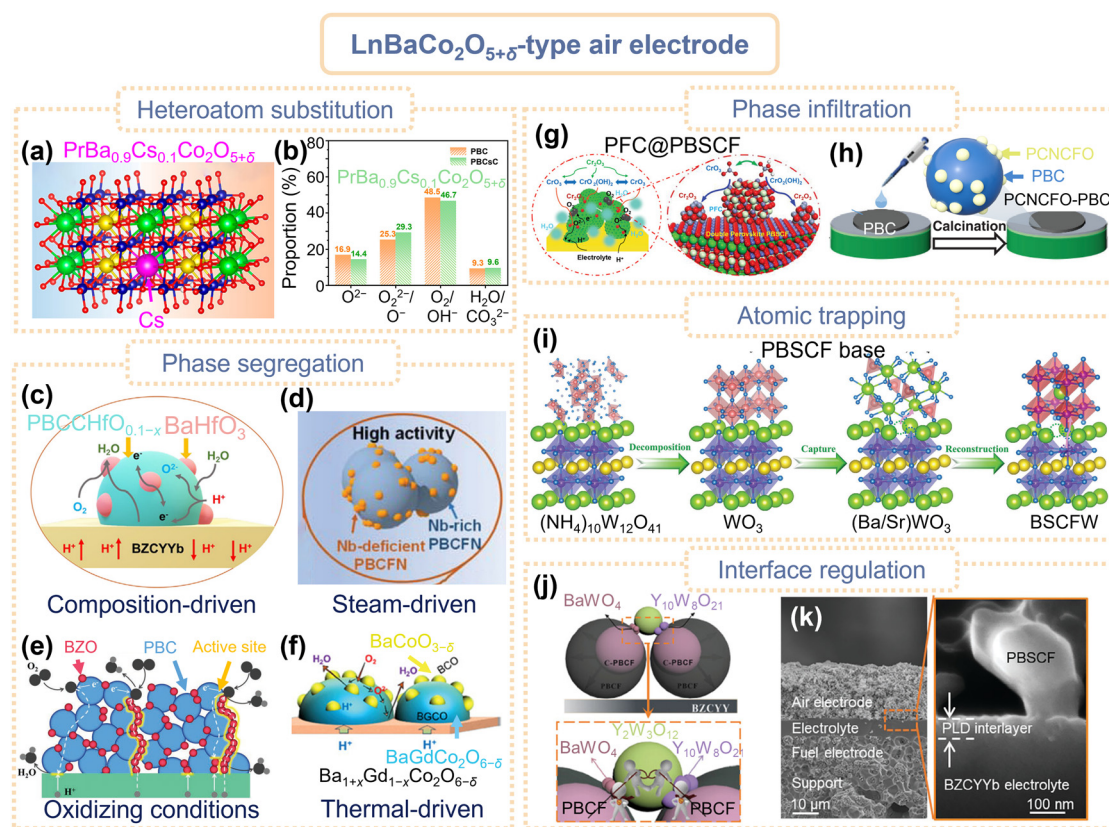
**Fig. 10** Recent advances in LnBaCo$_2$O$_{5+\delta}$-type air electrode materials. (a) Structure of PBCsC, (b) comparisons of different oxygen species contents of PBS and PBCsC. Reproduced with permission.[226] Copyright 2023, American Chemical Society. (c) Schematic of Hf-doped PBCCHf$_{0.1}$. Reproduced with permission.[229] Copyright 2024, Elsevier. (d) Schematic of PBCFN. Reproduced with permission.[230] Copyright 2022, Wiley-VCH. (e) Schematic of BZO@PBC. Reproduced with permission.[231] Copyright 2022, Wiley-VCH. (f) Schematic of BGCO−BCO hybrid catalyst. Reproduced with permission.[232] Copyright 2024, Wiley-VCH. (g) Schematic of PFC@PBSCF in the presence of contaminants (Cr and steam). Reproduced with permission.[234] Copyright 2022, Wiley-VCH. (h) Schematic for the fabrication procedures of PCNCFO−PBC. Reproduced with permission.[235] Copyright 2024, Wiley-VCH. (i) Structural evolution during reverse atom capture process. Reproduced with permission.[150] Copyright 2024, Wiley-VCH. (j) Mechanism underlying the thermo-mechanical enhancement of TEC gradient formation. Reproduced with permission.[382] Copyright 2024, Wiley-VCH. (k) Cross-sectional SEM image of PBSCF/BZCYYb composite interlayer. Reproduced with permission.[236] Copyright 2024, Wiley-VCH.

This journal is © The Royal Society of Chemistry 2025

Energy Environ. Sci., 2025, **18**, 4555–4595 | **4573**

attaining a PPD of 1.32 W cm^{-2} at 650 °C, alongside impressive long-term durability for 240 h.

Several methods exist for modifying the bulk structure of PBC-type air electrode materials including morphology engineering,[395] heterostructure construction,[234,396-398] compositing,[399-402] and microstructure design.[203,271,403] However, the large TECs of cobalt-based PBC materials (10.8 × 10^{-6} K^{-1} for BZCYYb, 23.7 × 10^{-6} K^{-1} for PBSCF) restrict their practical application by leading to mechanical incompatibility with electrolyte and poor electrolyte/electrode interface adhesion.[400,404] Negative thermal expansion materials represented by $Y_2W_3O_{12}$ and $Sm_{0.85}Cu_{0.15}MnO_{3-\delta}$ are added to the air electrode to offset the thermal expansion.[170,220,325] However, inadequate mechanical mixing and poor physical contact between powders can result in delamination due to the significant variation in the thermal expansion coefficient of the electrode material and added powders. Additionally, the use of negative thermal expansion materials is constrained by phase transitions triggered by temperature or pressure changes, as well as its low stiffness and hygroscopic nature. To address these challenges, Gao et al. proposed composite electrodes with a TEC gradient.[382] The transition phase, generated in situ due to topological atomic effects, helps bridge the thermal behavior gap and maintains thermo-mechanical stability. This approach also ensures chemical stability by preventing water vapor infiltration into the electrode. In this recently published study, the formation of the transitional phases, $BaWO_4$ and $Y_{10}W_8O_{21}$, at the interface between $PrBa(Co_{0.7}Fe_{0.3})_2O_{5-\delta}$ (PBCF) and $Y_2W_3O_{12}$ contributes to the development of TEC gradient electrode (Fig. 10(j)). And the transition phase captures the A-site element Ba in the electrolyte layer, thereby optimizing the electrolyte–electrode interface.

The abrupt transition from a dense electrolyte to a porous electrode creates discontinuous reaction pathways and oxygen vacancies, impeding charge transfer and the transport of gas and ionic phases, leading to a high polarization resistance at electrolyte/electrode interface. This weak adhesion, structural and chemical discontinuities, and limited contact points, exacerbates stagnation at the interface and restricts effectiveness of electrode at low operating temperatures.[84,132,405,406] Therefore, interface engineering is essential to address the challenges of efficient operation in P-SOCs at intermediate to low temperatures by ensuring a seamless transition between the electrolyte and electrode. Choi et al. introduced a mono-grain PBSCF/BZCYYb composite interlayer, which enabled an even lower operating temperature of 350 °C.[236,407] This composite interlayer was fabricated using pulsed laser deposition (PLD), with triple-conducting oxide PBSCF and proton-conducting oxide BZCYYb co-deposited onto a dense BZCYYb electrolyte (Fig. 10(i)). The resulting mono-grain composite interlayer features a quasi-2D thin layer with an alternately arranged, phase-separated structure, which extends the electrode/electrolyte interface by approximately 13.7 times compared to a reference sample with a conventional interface between a porous electrode and a dense electrolyte (Fig. 10(k)). The composite also exhibits a higher $V_O^{\bullet\bullet}$ concentration, about twice that of the PBSCF bulk powder electrode, due to charge modulation reactions at the heterointerface. This unique structure facilitates reaction pathways through vertically aligned oxygen

vacancies, significantly reducing both ohmic and polarization resistances. This mono-grain composite interlayer in a fuel electrode-supported configuration achieved a PPD of 0.50 W cm^{-2} and a current density of 0.25 A cm^{-2} at 1.3 V at 350 °C.

4.2. $LnBaFe_2O_{5+\delta}$-based perovskite

Despite their advantageous properties for electrochemical water splitting and power generation, cobalt-based perovskites exhibit drawbacks such as cobalt toxicity, high cost, and large TEC. Recent studies have highlighted several Fe-based double perovskites that show promising performance,[408-410] including $LaBaFe_2O_{5+\delta}$,[411] $PrBaFe_2O_{5+\delta}$,[412] $GdBaFe_2O_{5+\delta}$,[413] $NdBaFe_2O_{5+\delta}$,[414] and $SmBaFe_2O_{5+\delta}$.[411] Rational substitution strategies have been employed to enhance oxygen vacancy concentrations in $LnBaFe_2O_{5+\delta}$, for example, doping the A-site with Sr[415] and Ca,[416] and substituting the B-site with W,[417] Ta,[418] Nb,[419] and Mo.[420] $Pr_{0.8}Nd_{0.2}BaFe_{1.9}Zn_{0.1}O_{5+\delta}$ (PNBFZ)[238] developed by Teketel et al., demonstrates improved electrical conductivities, lower TEC (13.9 × 10^{-6} K^{-1}), and higher PPD of 401 mW cm^{-2} at 550 °C. BCO have been incorporated to construct composites.[421] However, compared to cobalt-based materials, layered iron-based perovskite air electrode materials exhibit slightly lower performance, and their potential requires further investigation.

5. Other representative perovskite

In addition to barium-containing perovskite materials, various other perovskite materials have seen significant advancements in recent years. This chapter focuses on lanthanide-rich perovskite structures and strontium-based perovskite materials, inspired by O-SOCs, to highlight their recent developments in intermediate-temperature P-SOCs air electrodes (summarized in Table 1).

5.1. $Ln_2NiO_{4+\delta}$ series

The nickel-based perovskite represented by RP-type oxide $Ln_2NiO_{4+\delta}$ (where Ln = La, Pr, and Nd) possesses a unique K_2NiF_4 structure, characterized by the alternating arrangement of perovskite and Ln–O rock salt layers along the c-axis. The presence of excess interstitial oxygen in the Ln–O layer serves as an ionic carrier, resulting additional electron holes,[422] which contribute to enhanced electrocatalytic capacity and enhanced surface oxygen-exchange kinetics.[423-425] Grimaud et al. were pioneers in investigating the hydration and electrochemical behaviors of $La_2NiO_{4+\delta}$ (LNO), $Pr_{2-x}Sr_xNiO_{4+\delta}$, and other related compounds.[63] Their work established a direct connection between the layered perovskite structure and triple-conducting behavior, making the RP phase $Ln_2NiO_{4+\delta}$ promising candidates for P-SOCs.[426-428]

La^{3+} in the A site with the larger ionic radius (La^{3+}: 1.36 Å; Ca^{2+}: 1.00 Å; Pr^{3+}: 0.99 Å) can effectively lower B–O bond strength for easier O^{2-} migration in the crystal lattice, which is beneficial for ensuring sufficient O^{2-} conductivity at reduced temperatures.[429-432] Unlike typical perovskite structures, where protons reside and migrate on regular O^{2-}, layered perovskite (RP), exampled by LNO, may contain oxygen interstitials that allow protons to locate and migrate. However, the performance

4574 | Energy Environ. Sci., 2025, **18**, 4555–4595

This journal is © The Royal Society of Chemistry 2025

of LNO-based electrodes is limited by their low electronic conductivity and excessive alkaline earth metals. To improve this, various doping and compositing strategies have been employed.[433,434] Sr-substituted $La_{1.2}Sr_{0.8}NiO_{4+\delta}$ (LSN), for instance, achieved resistance of 0.15 Ω cm^2 in symmetric cell and a PPD of 460 mW cm^{-2} at 700 °C.[435] Zhong et al. reported that the water content in both pristine LNO and $La_{2-x}A_xNiO_{4+\delta}$ (where A = Ca, Sr, Ba) rises with the level and basicity of the dopant increase (Fig. 11(a) and (b)).[427,436] Wang et al. improved electronic conductivity by partially substituted Ni with Cu in $La_{1.5}Sr_{0.5}NiO_{4+\delta}$, increasing it from 74 S cm^{-1} to 171 S cm^{-1} at 800 °C. This enhancement was primarily attributed to the contraction of Ni–O bonds and the oxidation of Ni^{2+} to Ni^{3+}. Cu, Zn co-doped LSN demonstrates a high electrolysis current density of 1.5 A cm^{-2} (1.3 V) at 600 °C under high humidity (60%) in air. A self-assembled composite of $La_{0.6}Sr_{0.4}FeO_{3-\delta}$–LSN, developed by Yang et al., exhibited low polarization resistances of 0.055 Ω cm^2 at 700 °C in O_2.[437]

The $Pr_2NiO_{4+\delta}$ (PrN)-based phases have been attempted in P-SOCs systems. Grimaud et al. found that PrN can function as a triple-conducting conducting oxide with low R_p when combined with a proton conductor like $BaCe_{0.9}Y_{0.1}O_{3-\delta}$ (BCY10).[63] In their subsequent work, they developed the BCY10-PrN composite to reduce TEC and optimize electrochemical properties through microstructure tuning.[438] To improve insufficient adhesion of mixed systems, Tarutin et al. developed Cu-doped $Pr_2Ni_{0.8}Cu_{0.2}O_{4+\delta}$, which demonstrates a PPD of ~340 mW cm^{-2} at 750 °C.[239] Nevertheless, the phase stability of PrN requires further improvement due to the decomposition of PrN into $PrNiO_3$ and PrO_2, leading to mixed ionic oxides formation at the electrode/electrolyte interface.[439]

The electrocatalytic,[424] oxygen transport,[440] and electrochemical properties[441,442] of $Nd_2NiO_{4+\delta}$ (NNO) have been extensively documented in the literature.[443] Luebber et al. utilized NNO to fabricate micro-tubular SOFC. Ba-doped $Nd_{1.9}Ba_{0.1}NiO_{4+\delta}$ demonstrates lower polarization resistances, reaching as low as 1.7 Ω cm^2 at 700 °C.[444] Additionally, the incorporation of Sr in $Nd_{2-x}Sr_xNiO_{4+\delta}$ alters the oxidation state of Ni from Ni^{2+} to Ni^{3+}, thereby influencing its magnetic properties.[445] However, NNO undergoes a tetragonal to orthorhombic phase transition at 610 °C, which necessitates careful consideration of its application in intermedium-temperature catalysis.[446]

5.2. $SrMO_{3-\delta}$-based perovskite

$SrMO_{3-\delta}$ with alkaline earth element Sr at A site is used as catalytic activity enhancement materials. $SrCoO_{3-\delta}$ (SCO), for example, was infiltrated on $Na_{0.3}Sr_{0.7}Ti_{0.1}Fe_{0.9}O_{3-\delta}$ (NSCF0.3@SC) thus achieving an improved PPD of 966 mW cm^{-2} at 600 °C.[167] Zhu et al. decorated $SrCo_{0.5}Nb_{0.5}O_{3-\delta}$ (SCN) NPs on the surface of $PrSrCo_{1.8}Nb_{0.2}O_{6-\delta}$ (PSCN).[240] This SCN NPs decoration significantly reduces the energy barriers associated with surface oxygen and vapor dissociation. Thus, SCN-PSCN composite electrode manifests a PPD of 1.30 W cm^{-2} and a current density of 1.91 A cm^{-2} at 1.3 V at 650 °C. However, Sr-containing electrodes often degrade due to Sr segregation, which results from the reactivity of Sr with steam. This segregation problem is particularly pronounced in EC mode, where higher steam concentrations exacerbate the issue.[194,447] To mitigate it, various methods have been proposed, including doping with Ca,[448] however, these have shown limited effectiveness. A more promising approach is transforming unstable Sr-containing single phases into stable hybrid materials
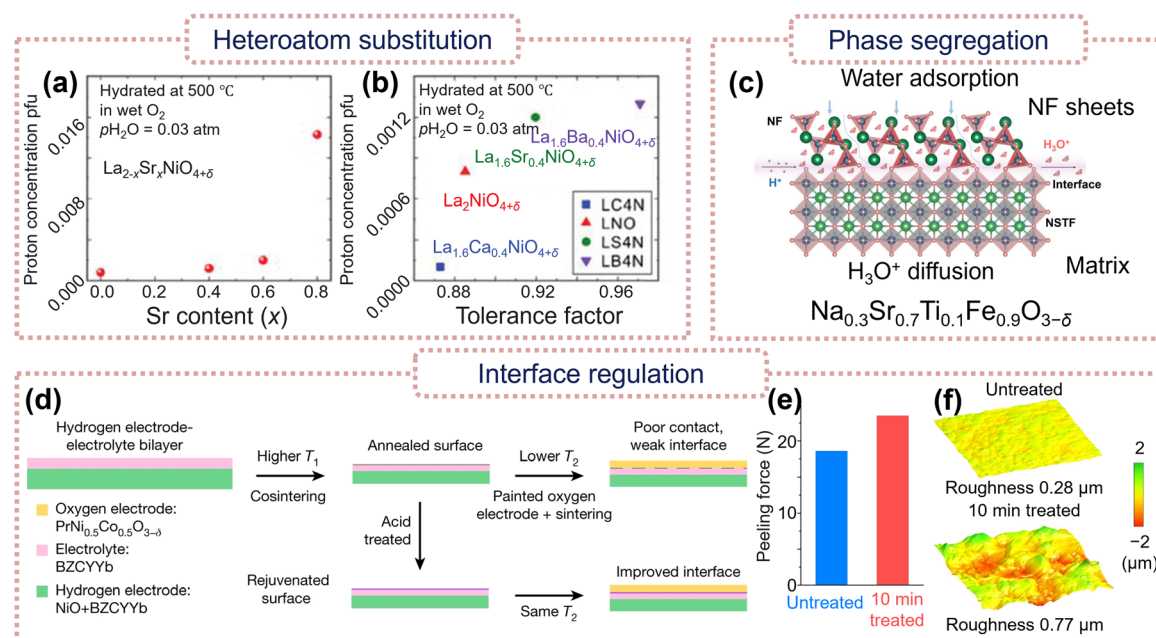

Fig. 11 Recent advances in $Ln_2NiO_{4+\delta}$, $SrMO_{3-\delta}$, and $PrMO_{3-\delta}$-type air electrode materials. Proton concentrations per formula unit (pfu) of (a) $Ln_2NiO_{4+\delta}$, and (b) $La_2NiO_{4+\delta}$ and $La_{1.6}A_{0.4}Ni_{4+\delta}$ (A = Ca, Sr, Ba). Reproduced with permission.[427] Copyright 2022, Wiley-VCH. (c) Schematic of H_3O^+ diffusion in NSTF. Reproduced with permission.[167] Copyright 2024, Wiley-VCH. (d) Schematic fabrication process. (e) Peeling strength of cathode-electrolyte interface. (f) AFM for electrolyte surfaces. Reproduced with permission.[241] Copyright 2022, Springer Nature.

This journal is © The Royal Society of Chemistry 2025

Energy Environ. Sci., 2025, **18**, 4555–4595 | **4575**

by leveraging the segregation phenomenon through careful structure regulation.[449–451] Song *et al.* synthesized a $Sr_{0.9}Ce_{0.1}Fe_{0.8}$-$Ni_{0.2}O_{3-\delta}$ (SCFN)-based nanocomposite electrode, featuring tetragonal and RP phases with surface-enriched CeO_2 and NiO NPs.[171] The RP phase in SCFN enhances hydration and H^+ conduction, while the nanoscale NiO and CeO_2 phases facilitate oxygen surface exchange and transfer of O^{2-} ions from the RP or NiO surfaces to the primary phase. Zhou *et al.* developed a self-assembling two-phase Na-doped $SrTi_{0.1}Fe_{0.9}O_{3-\delta}$ cathode for P-SOFCs, featuring a $Na_ySr_zTi_uFe_{1-u}O_{3-\delta}$ (NSTF) perovskite main phase and nanosized β-$NaFeO_2$ (NF) through thermal-induced phase exsolution (Fig. 11(c)).[167] Unlike most air electrode materials that exhibit a negative dependence on pH_2O, the NSTF/NF nanocomposite cathode demonstrates a positive pH_2O dependence in SOFC applications. This is attributed to enhanced H^+ uptake and the potential development of a H_3O^+ transport pathway at the NSTF and NF phases interface, resulting in a new quadruple-conducting (H_3O^+/H^+/O^{2-}/e^-) cathode that yields a PPD of 0.807 W cm^{-2} at 600 °C.

Extrinsic Cr and S impurities at the surface represent another source of degradation in strontium-based perovskites.[452] The accumulation of electronically and ionically insulating contaminants—such as Cr_2O_3, SO_2, and secondary compounds like $SrCrO_4$ and $SrSO_4$—on the perovskite surface during SOFCs operation, primarily from vaporized Cr originated from metal interconnects and S-based species in the gas flow, ultimately degrades catalytic performance.[453–458] Several strategies have been explored to mitigate the detrimental effects of Cr, including: (i) the use of Cr getters,[459] (ii) coating of the interconnects,[460] and (iii) surface modifications that demonstrate high resistance to Cr poisoning.[383,461,462] However, the issue of Cr and S poisoning of Sr-based materials in P-SOCs requires further investigation.

5.3. PrMO$_{3-\delta}$-based perovskite

$PrNi_{0.5}Co_{0.5}O_{3-\delta}$ (PNC), belonging to the $PrMO_3$ family, is recognized as an effective triple-conducting air electrode material for P-SOCs due to its high proton conductivity. PNC is inspired by $PrCoO_3$ (PCO) and lanthanide nickelates, combined the advantages of segregation mitigation and excellent tolerance to high steam vapor and varying oxygen partial pressures.[463–466] Ding *et al.* demonstrated that appropriate nickel substitution at the B-sites of the PNC perovskite can lower the migration barrier for proton conduction, and easily introduce proton defects through hydration reactions.[172] This enhancement in proton conduction, combined with the triple-conducting capabilities of PNC, facilitates both WOR and ORR, thereby improving the electrochemical performance during self-sustained and reversible operations at reduced temperatures. To broaden the application of PNC in low-temperature P-SOCs, addressing the issue of poor contact at the electrode/electrolyte interface is crucial. A straightforward acid treatment developed by Bian *et al.* can effectively rejuvenate the surface of high-temperature annealed electrolytes (Fig. 11(d)).[241] This process fosters reactive bonding between the air electrode PNC and the electrolyte BZCYYb, leading to enhanced electrochemical performance and stability (Fig. 11(e) and (f)). Exceptional performance in P-SOFC is achieved at temperatures as low as 350 °C, with PPDs reaching 1.6 W cm^{-2} at 600 °C, 650 mW cm^{-2} at

450 °C, and 300 mW cm^{-2} at 350 °C. However, Pr is classified as a critical material by the European Commission and its large-scale use both unsustainable and costly.[467] Additionally, When PNC is combined with the proton-conducting electrolyte BZCY, it demonstrates low tolerance to H_2O and CO_2.[468] Therefore, more research is needed to improve their compatibility. Yao *et al.*, for example, impregnated $Pr_2Ni_{0.5}Co_{0.5}O_{4-\delta}$, which consists of a PNC perovskite phase and a PrO_2 phase, onto LSCF base.[242] The PNC perovskite phase facilitates rapid proton transport, while the PrO_2 nanoparticles, characterized by a high concentration of oxygen vacancies, enhance both oxygen adsorption and transfer. The modified electrode achieving a PPD of 1857 mW cm^{-2} at 700 °C, and exhibit durability for 200 h.

In addition to alkaline earth and rare earth element-based air electrodes, alkali metal-based materials are also being investigated for solid oxide cell development. For example, $LiCoO_2$, a widely used cathode material in lithium-ion batteries, has achieved a PPD of 0.86 W cm^{-2} at 800 °C in O-SOFCs, benefiting from coordinated lithium volatilization and anion doping.[469] Given the extensive adoption of lithium-ion technology, integrating recycled lithium-ion battery materials into solid oxide cell research presents a cost-effective approach. Moreover, the high-temperature operating environment efficiently removes volatile impurities, enhancing the feasibility of repurposing recycled materials for solid oxide cell applications.

6. Theoretical insights and computational design

Theoretical calculations are a powerful research tool in the field of SOCs including synthesis of perovskite and their application as air electrode materials. The complex compositions of perovskites render the exploration and development of efficient air electrode materials both time-consuming and challenging, which inevitably drove a search for more efficient tools. Theoretical calculations—especially high-throughput screening and machine learning—inherently became leading tools for the role thanks to their reliability and adaptability. The operational temperature of approximately 600 °C complicates direct observation of the air electrode's functioning SOCs which reduce their reliability there and beyond. Theoretical calculations effectively simulate operating conditions of the electrode and elucidate the underlying microscopic principles at play (summarized in Fig. 12).

6.1. Computational approaches for high-performance design

Traditional approaches of discovering and developing new materials typically depend on empirical experiments and trial-and-error techniques, which can be time-consuming, costly, and often constrained in their scope. In contrast, simulations can integrate computational chemistry, molecular orbital theory, and experimental methods to effectively guide the discovery and optimization of air electrodes.[117,470]

By leveraging theoretical calculations, researchers can systematically explore material properties and behaviors, thereby
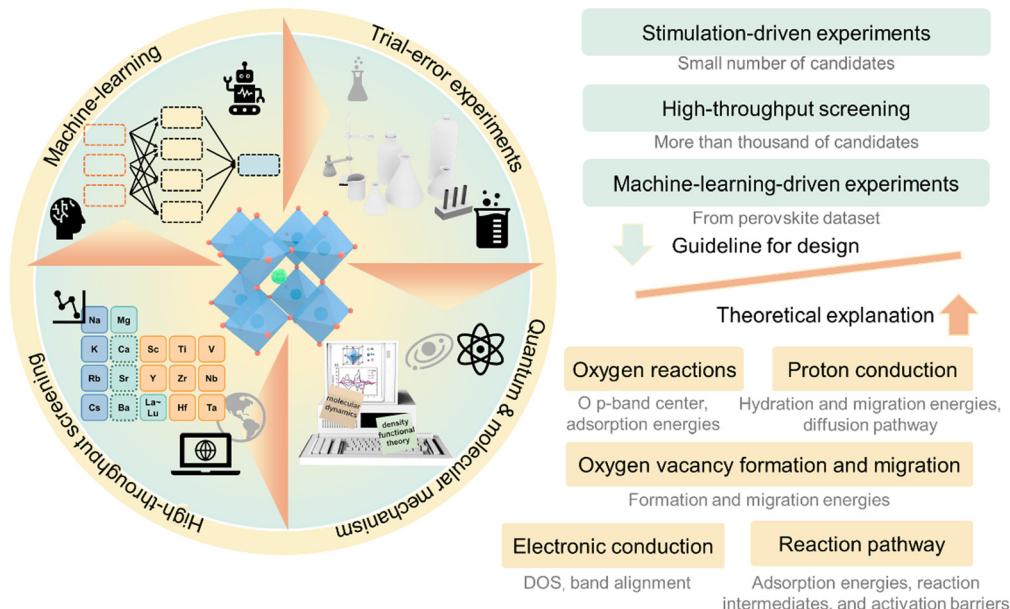
Fig. 12 Application of theoretical calculations in the development of perovskite air electrodes.

streamlining the design process and identifying optimal candidates more efficiently. In the study conducted by Mao *et al.*, the optimization of bimetal-doped SCO was guided by DFT calculations focusing on two key parameters: the formation energy and the migration barrier of oxygen vacancies.[267] A lot of 13 different TMs was evaluated as potential dopants with working resulting in 91 possible combinations for bimetal-doped SCO to identify the most promising electrode candidate. Ciucci and colleagues have utilized *ab initio* simulations, molecular orbital insights to design A- and B-site co-substituted BFO materials.[34] By combining calculated lattice constants, substitutional defect formation energy E_{form}, oxygen vacancy formation energy $E_{\text{vac}}(V_O^{\bullet\bullet})$ and hydration energy E_{hydr}, they concluded a potential $Ba_{0.875}Fe_{0.875}Zr_{0.125}O_{3-\delta}$ candidate (Fig. 13(a)).[34] And as validated in experiments, the designed cathode can achieve impressive PPDs of 0.67 W cm^{-2}, 1.28 W cm^{-2}, and 2.04 W cm^{-2} at 500 °C, 600 °C, and 700 °C, respectively, and outstanding stability exceeding 200 h even in high-steam environments. Simulation-driven strategies enhance the potential for innovative material development while reducing time, manpower, and economic expenditures. Researchers can streamline the experimental process, focus resources on the most promising candidates of high effective catalyst, and avoid redundant or less effective experiments. The high-throughput computational methods employed by Luo *et al.* facilitated the screening of 932 materials based on key parameters such as $V_O^{\bullet\bullet}$ formation energy, hydration energy, and adsorption energy, thereby expediting the discovery and optimization of proton conductors.[471] Very recently, Hu *et al.* used high-throughput calculations combined with data-driven decomposition analysis to forecast essential properties for 4455 unique perovskite oxides, focusing on their thermodynamic stability and decomposition tendencies crucial for various applications (Fig. 13(b)).[237]

Since the advent of artificial intelligence (AI) and the increasing amount of experimental data in material synthesis, machine learning (ML) techniques have become the cornerstone of new material discoveries, accelerating the design, prediction of property, and optimization.[372] ML involves the use of computational algorithms and statistical models to analyze extensive datasets, enabling the extraction of meaningful patterns and facilitating predictions or optimizations based on these insights.[472–474] Consequently, it is able to speed up the discoveries and guides experimental work towards the most promising candidates materials at relatively short time and low budge.[475–479] ML models to date have been used to identify the critical factors affecting $H^+/O^{2-}/e^-$ conductivities through feature selection and engineering techniques. In 2021, an XGBoost model was constructed to efficiently and accurately predict the conductivities of 97 625 perovskite oxides under wet (3% H_2O) hydrogen and wet air environments.[480] In hydration abilities analysis, Wang *et al.* employed a random forest (RF) model to identify efficient mixed proton–electron conductive oxides by predicting the hydrated proton concentration (HPC) of 3200 $A_{1-x}A1_xB_{1-y}B1_yO_3$ perovskite oxides.[481] Through this RF approach, they successfully predicted the HPC of these perovskite oxides, enabling the selection of highly efficient mixed proton–electron conductive materials. Recent studies also indicate that ML models can effectively predict the catalytic activity of air electrode materials in solid oxide cells, particularly regarding resistance to oxygen reduction (R_p), power density, energy barriers, oxygen p-band centers, and vacancy formation energies, often calculated *via* DFT.[482–485] Integrating ML with DFT has been found enhancing efficiency and accuracy of these calculations, facilitating faster material innovation.[486] Ni *et al.* introduced ionic Lewis acid strength (ISA) as an effective physical descriptor to accelerate the research of ORR activity.[372] Their model successfully predicted the R_p of 6871 oxides, demonstrating the best fit among eight different regression models.

This journal is © The Royal Society of Chemistry 2025

Energy Environ. Sci., 2025, **18**, 4555–4595 | **4577**
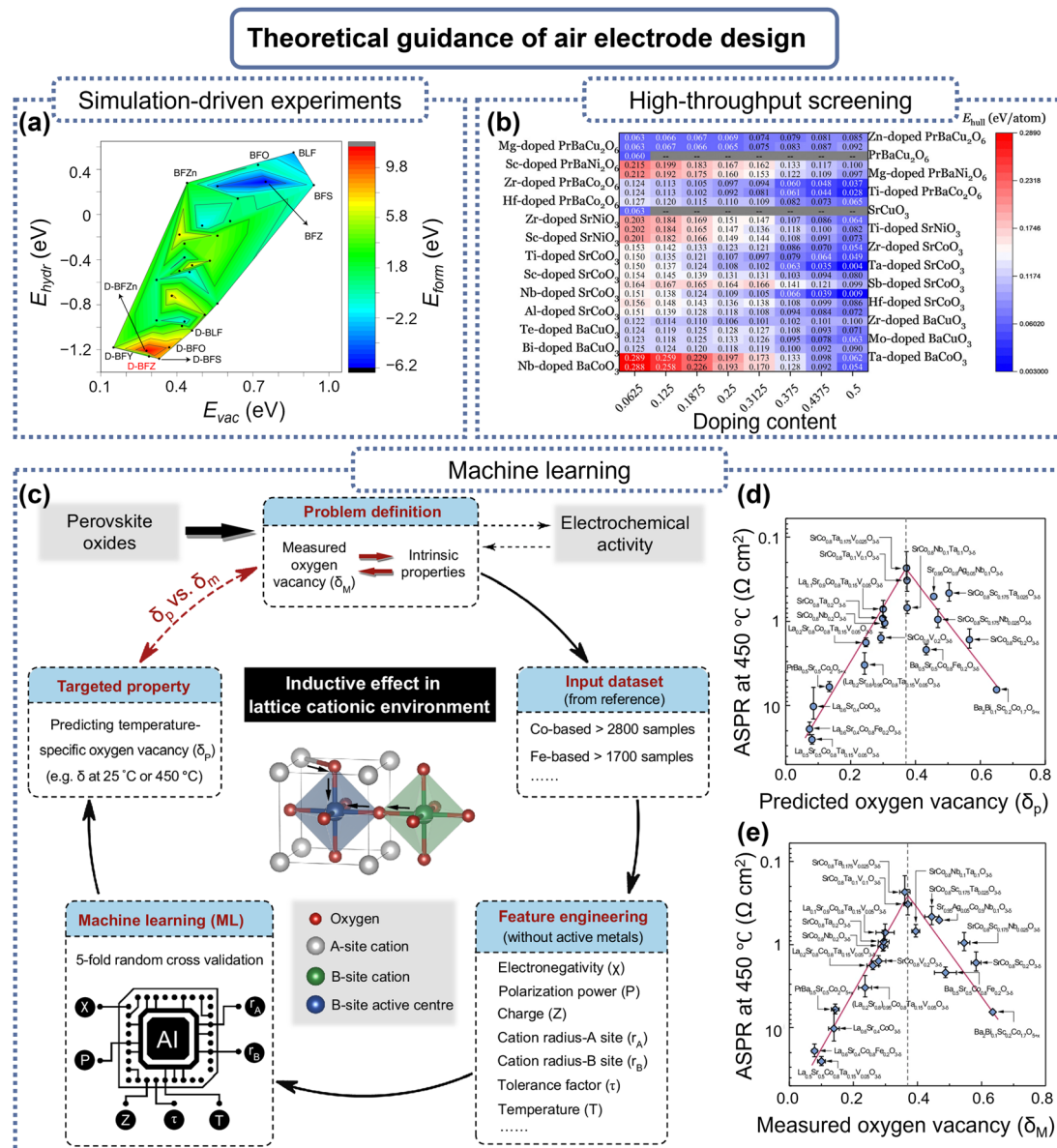
Fig. 13 (a) Plot of computed E_{form} against E_{vac} and E_{hydr} for BFO and its derivative materials (dots). Reproduced with permission.[34] Copyright 2022, Springer Nature. (b) Promising perovskite candidates with exceptional thermodynamic stability. Reproduced with permission.[237] Copyright 2024, Royal Society of Chemistry. (c) Workflow of oxygen vacancies prediction, and (d) and (e) the measured and predicted ASR. Reproduced with permission.[81] Copyright 2024, Springer Nature.

The important score assigned to each descriptor revealed that A/B-site ionic Lewis acid (AISA/BISA) significantly influences model predictions, suggesting a strong correlation with intrinsic ORR activity. An active learning strategy can be used to predict H_2 production in high-entropy oxides, enabling a more rational design of high-entropy materials rather than relying solely on experience and intuition.[487] A very recent study by Li *et al.* shows ML techniques have been used by to quantify the relationship between oxygen vacancy concentrations and catalytic activity, based on 235 cobalt-based and 200 iron-based perovskite catalysts (Fig. 13(c)).[81] The temperature-dependent variation in oxygen vacancy concentrations in both Co-based and Fe-based perovskites can be accurately predicted from

well-established elemental properties. The oxygen electrocatalytic activity of perovskite oxides exhibit a "volcano" dependence on oxygen vacancies concentrations, where the optimal oxygen vacancy concentration for electrocatalysis changes with the operating temperatures (Fig. 13(d) and (e)). This study offers an efficient approach with oxygen vacancy-activity relations to efficiently predict perovskite for electrocatalysis operated across a broad temperature range.

Additionally, ML models have been developed to predict the thermodynamic phase stability of perovskite oxides by estimating their energy above the convex hull (E_{hull}) under realistic conditions.[488] The reliability of these models was confirmed through comparisons with DFT results and validation against

newly generated compounds.[489] Furthermore, EIS data has been used to train neural networks, which successfully forecast long-term performance degradation. The challenges, however remain as shown by Hagen *et al.*, who found weak correlations in degradation assessments based on a comprehensive dataset of SOC tests, highlighting the need for more extensive data to enhance statistical significance in ML applications for durability predictions.[490] ML holds great promise for developing high-efficiency perovskite air electrode materials for P-SOCs. However, challenges such as data availability, complexity of materials data, and the need for effective feature engineering hinder its application. Balancing multiple target properties like catalytic activity and stability is also difficult due to trade-offs between performance and degradation. Despite these obstacles, leveraging big data and advanced computing can enhance efficiency and accuracy of ML in materials research. Overcoming these challenges requires collaboration, better data standards, and improved model interpretability.

6.2. Mechanistic understanding from simulations

Due to the challenges of direct observation, theoretical calculations have emerged as a powerful tool for elucidating the microscopic mechanisms of efficient air electrodes. These mechanisms primarily involve reactions related to protons and oxygen ions. By analyzing the adsorption, transfer, and reaction processes of charge carriers, researchers can establish a connection between structure and performance, thereby guiding the optimization of air electrode materials. Hydration reactions involve proton incorporation and interactions with lattice oxygen, which is regarded as water adsorption and proton transport. Li *et al.* evaluated the impact of doped boron (B) on surface chemical properties by calculating water adsorption energies.[491] They found that the B-modified $Pr_4Ni_3O_{10+\delta}$ (0.5B-PN) surface had a water adsorption energy of -1.4 eV, compared to -0.9 eV for the PN surface, reflecting a 55.6% improvement in hydration ability due to the surface modification with dispersed B. Lu *et al.* calculated hydration energies for different cells by inserting H_2O into oxygen vacancies of extracted cells in parent perovskite structures (Fig. 14(a)).[183] $BaCo_{0.4}Fe_{0.4}Nb_{0.2}O_{3-\delta}$ (BCFN) showed the highest hydration energy which is indicative of strong affinity for H_2O molecules, the performance partly attributed to Nb^{5+} doping. For F-doped BCFZY examined by Ren *et al.*, the reduction in lattice size was confirmed through cell structure analysis, and hydration properties were illustrated by the adsorption energies of H_2O on $Fe-V_O-Co$ sites and integrated crystal-orbital Hamilton populations (iCOHPs, Fig. 14(b)).[166] By simulating the electronic structure and potential energy surfaces of perovskites, proton conduction mechanisms can be provided. Liu *et al.* used climbing image nudged elastic band (CINEB) calculations to show higher energy barrier (E_b) for proton migration for hopping pathway than rotation pathway in perovskites, identifying hopping as the rate-limiting step (Fig. 14(c)).[179] They found Er-doping in BSCF lowering E_b for the hopping pathway by 0.13 eV. Er_2O_3, with its simpler proton hopping process, achieves an even lower E_b of 0.35 eV and a greater hopping distance compared to $Ba_{0.5}Sr_{0.5}Co_{0.8}Fe_{0.2}O_{3-\delta}$

(BSCF) and $Ba_{0.5}Sr_{0.5}(Co_{0.8}Fe_{0.2})_{0.9}Er_{0.1}O_{3-\delta}$ (BSCFE), indicating that Er_2O_3 markedly improves proton migration in composite electrodes. Beyond E_b, factors such as the $O{\cdots}H$ bonds formation energy and distance are also crucial for predicting proton conduction. Chen *et al.* reported higher positive formation energy for $O{\cdots}H$ bonds in $Ba_{0.5}Sr_{0.5}Co_{0.8}Fe_{0.2}O_{2.9-\delta}F_{0.1}$ (BSCFF) than $Ba_{0.5}Sr_{0.5}Co_{0.8}Fe_{0.2}O_{3-\delta}$ (BSCF), suggesting more robust bonds formation with oxygen by the proton in BSCF (Fig. 14(d)).[213] This stronger bonding results in a more challenging hopping process for protons, following the Grotthus mechanism. Moreover, fluorinated oxides like BSCFF exhibit longer $O{\cdots}H$ distances, which implies easier disruption of these bonds and a reduced energy barrier for proton displacement. To analyze proton diffusion pathways and conductivity,[492] first-principles molecular dynamics (FPMD) simulations at 1000 K were employed by Kim *et al.*[199] These simulations showed more rapidly protons diffusion in $BaSc_{0.1}Ta_{0.1}Co_{0.8}O_{3-\delta}$ (BSTC) compared to $BaCoO_{3-\delta}$ (BCO) as evidenced by a higher mean squared displacement (MSD) for BSTC (Fig. 14(e)). This enhanced diffusion is linked to hydroxide rotation, proton transfer, and trapping phenomena. In terms of diffusion pathways, BSTC establishes a continuous 3D proton transport network within 100 ps, whereas BCO develops a more limited 2D network (Fig. 14(f)). The proton conductivity of BSTC measured at 4.94×10^{-4} S cm^{-1} using the Nernst–Einstein relation, indicating its suitability for P-SOCs air electrodes. Furthermore, negative crystal orbital Hamiltonian populations (–COHPs) reveal that $O{\cdots}H$ bonds in BSTC are weaker than those in BCO with integrated –COHP values of 3.87 eV bond^{-1} for BSTC and 3.95 eV bond^{-1} for BCO. This suggests that BSTC facilitates more efficient proton transfer due to its weaker $O{\cdots}H$ bonds and decomposition in the O 2p and H 1s orbitals.

Proton-involved oxygen reactions dominate the kinetics of air electrode. He *et al.* utilized DFT calculations to investigate how A-site entropy tuning affects the performance of perovskite materials for OER and ORR.[212,493] The study compared high-entropy $Pr_{0.2}Ba_{0.2}Sr_{0.2}La_{0.2}Ca_{0.2}CoO_{3-\delta}$ (PBSLCC) with binary $PrBaCo_2O_{5+\delta}$ (PBC) and ternary $Pr_{0.8}Ba_{0.8}Ca_{0.4}Co_2O_{5+\delta}$ (PBCC), focusing on key descriptors such as the O p-band center,[36,107,495] $V_O^{\bullet\bullet}$ formation energies, and oxygen adsorption. The projected density of states (PDOS) of PBCC and PBSLCC was displayed to verify the strong hybridization of cations in the B-site Co ion with oxygen (Fig. 14(g)).[493] The O p-band center PBSLCC shifted closer to the Fermi level (-3.29 eV) compared to PBC and PBCC. The oxygen vacancy formation energies (E_{vac}) in PBSLCC (0.97 eV) is lower compared to PBC (1.35 eV) and PBCC (1.31 eV).[496] Oxygen adsorption energies (ΔE_{ads}) studies revealed that PBSLCC exhibits weaker oxygen bonds and better kinetics, in line with Sabatier's principle.[497,498] Overall, the research confirms that A-site entropy tuning significantly enhances OER and ORR performance by optimizing the activity of oxygen reactions.

Oxygen vacancies play a crucial role in affecting ion transfer and hydration properties of perovskite oxides. To assess the hydration and oxygen ion transfer capabilities of air electrode materials, researchers examine the formation energy of oxygen vacancies in different materials and lattice sites. Liu *et al.*

This journal is © The Royal Society of Chemistry 2025

Energy Environ. Sci., 2025, **18**, 4555–4595 | **4579**
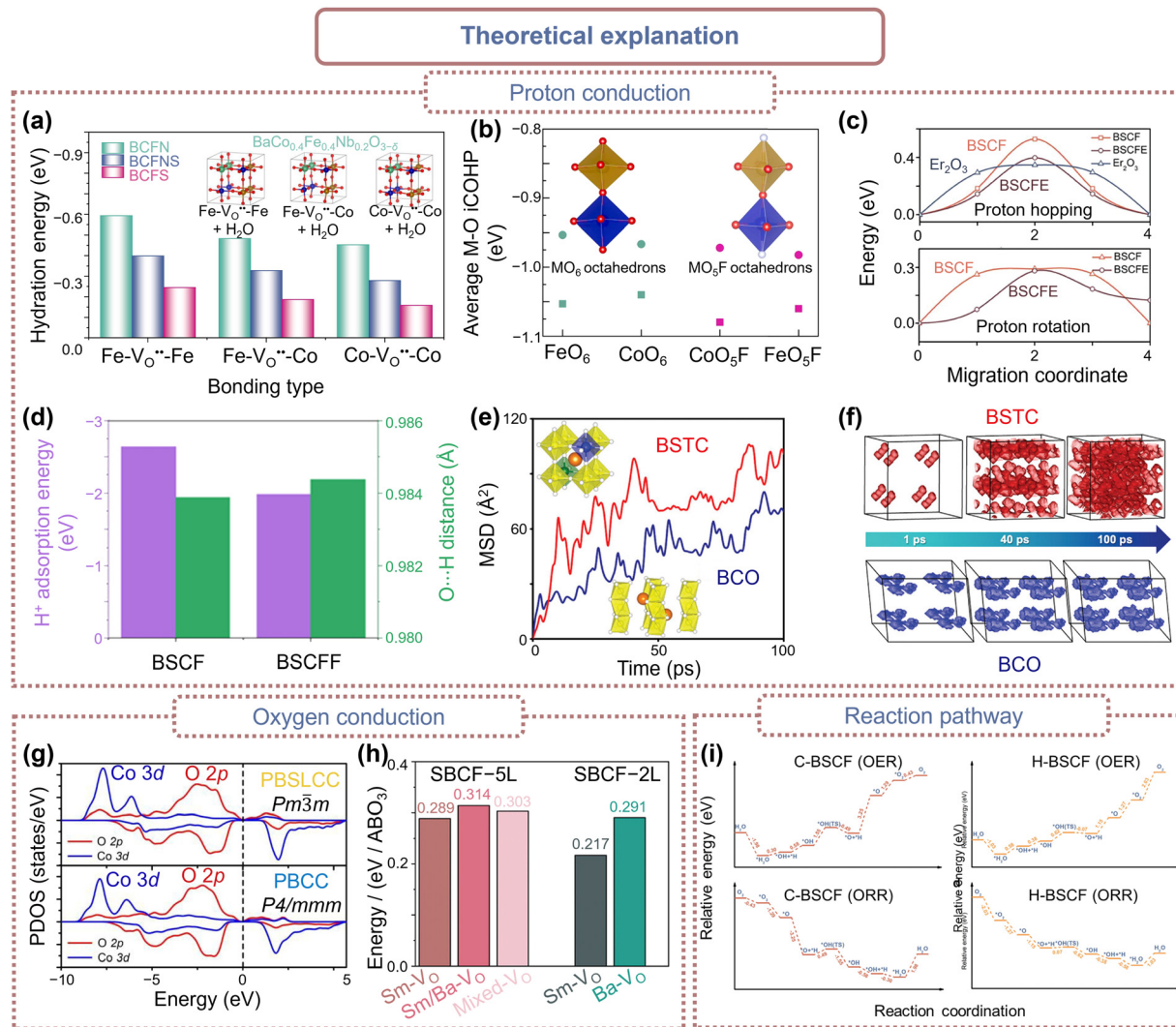
Fig. 14 Recent advances in theoretical explanation for efficient air electrode materials. (a) Hydration energies of the BCFN, BCFNS, and BCFS (inset: optimized structural models for the hydrated samples of BCFN). Reproduced with permission.[166] Copyright 2023, Elsevier. (b) M−O iCOHP value comparison for BCFZY(F). Reproduced with permission.[164] Copyright 2022, Elsevier. (c) Energy profile for proton hopping and rotation in BSCF, BSCFE, and Er_2O_3. Reproduced with permission.[179] Copyright 2023, Wiley-VCH. (d) O···H formation energy and distance for BSCF(F). Reproduced with permission.[213] Copyright 2023, Elsevier. (e) MSD of a hydrogen atom and (f) time-dependent evolution of H^+ diffusion pathways in BSTC and BCO. Reproduced with permission.[199] Copyright 2024, Wiley-VCH. (g) PDOS of the O 2p and Co 3d orbitals of PBCC and PBSLCC. Reproduced with permission.[493] Copyright 2023, Elsevier. (h) Oxygen vacancy formation energy in electrodes SBCF-2L and SBCF-5L. Reproduced with permission.[494] Copyright 2024, Wiley-VCH. (i) Energy barrier of cubic C-BSCF (100) and hexagonal H-BSCF (0001) surfaces. Reproduced with permission.[214] Copyright 2024, Springer Nature.

showed that the Er-doping notably reduces E_{vac} and hydration energy (E_{hdr}) by 0.12 eV and 0.22 eV, respectively.[179] This doping strategy thus enhances hydration ability of $Ba_{0.5}$-$Sr_{0.5}Co_{0.72}Fe_{0.18}Er_{0.09}O_{3-\delta}$–$Er_2O_3$ composite air electrode. In a separate study, Sun et al. used DFT calculations to evaluate the oxygen vacancies formation energy in $Sm_{0.8}Ba_{1.2}Co_{0.8}Fe_{1.2}O_{5+\delta}$ (SBCF-5L) and $SmBaCo_{0.8}Fe_{1.2}O_{5+\delta}$ (SBCF-2L).[494] he vacancies for SBCF-5L are more easily formed in the –[SmO_{1-x}]– layer, with formation energies of 0.289 eV and 0.314 eV for the –[SmO_{1-x}]– and perovskite layers, respectively. In contrast, SBCF-2L shows values of 0.217 eV and 0.291 eV (Fig. 14(h)). When vacancies are present in the –[SmO_{1-x}]– layer of SBCF-5L, the formation energy in the perovskite layer drops, facilitating

enhanced three-dimensional oxygen ion conduction. This results in a higher initial concentration of oxygen vacancies in SBCF-5L compared to SBCF-2L, making SBCF-5L more efficient for oxygen ion transport. In Chen et al.'s work, the oxygen vacancy formation and PDOS of Fe-substituted $Nd_{0.8}Sr_{1.2}Ni_{1-x}Fe_xO_{4\pm\delta}$ was predicted by DFT.[499] The oxygen vacancy formation energy was calculated as 4.34 eV for $Nd_{0.8}Sr_{1.2}NiO_{4\pm\delta}$ (NSN) and 4.19 eV for $Nd_{0.8}Sr_{1.2}Ni_{0.7}Fe_{0.3}O_{4\pm\delta}$ (NSNF), showing that Fe doping reduces this energy compared to other perovskite oxides. Fe 3d electrons are closer to the Fermi level compared to Ni 3d, indicating improved catalytic activity with Fe doping. Lower oxygen vacancy formation energy, coupled with accelerated charge transfer through

4580 | *Energy Environ. Sci.*, 2025, **18**, 4555–4595

This journal is © The Royal Society of Chemistry 2025

Fe–O–Ni bridges, suggests enhanced catalytic activity for ORR and OER in Fe-doped NSN.[500,501]

In perovskite oxides, electronic conduction often occurs *via* polaron hopping. To understand factors influencing overall electronic conductivity, density-of-states (DOS) and band alignment simulations are employed. Yu *et al.* analyzed DOS plots for $Sr_3Fe_{1.8}Nb_{0.2}O_{7-\delta}$ (SFN) and $Sr_{2.8}Fe_{1.8}Nb_{0.2}O_{7-\delta}$ (D-SFN) to understand the effects of Nb doping and A-site cation defects.[502] These plots show that the conduction band near the Fermi level is mainly influenced by Fe 3d orbitals while the valence band comes from O 2p orbitals. In D-SFN, there are more unoccupied states near the valence band which suggests better charge transfer. The addition of Sr defects increases Fe valence states, enhancing the overlap between Fe 3d and O 2p orbitals. This stronger Fe–O interaction improves electron conduction in D-SFN. Additionally, DOS analysis was performed by Zhou *et al.* to analyze different active sites of $PrBa_{0.8}Ca_{0.2}Co_2O_{5+\delta}$–$BaCoO_{3-\delta}$ (PBCC–BCO) composite air electrode.[194] Their findings showed that Co majority spin states at PBCC (010) lose more electrons compared to $BaCoO_3$ (110), which is linked to differences in coordination. Specifically, $BaCoO_3$ (110) benefits from electron-donating Ba, which creates an electron-rich region at the Co sites, enhancing interactions with oxygen-containing intermediates. This increased interaction facilitates water deprotonation but limits oxygen desorption on $BaCoO_3$ (110).

The OER process on the air electrode surface involves several steps: H_2O adsorption ($^*H_2O$, * indicates the adsorbed state), oxygen evolution ($^*H_2O \rightarrow {}^*OH + {}^*H \rightarrow {}^*O + {}^*H \rightarrow {}^*O \rightarrow {}^*O_2$), and $^*O_2$ desorption, whereas the ORR process is essentially the reverse of OER process.[30,194,503] Combining calculating adsorption energies, reaction intermediates, and activation barriers, OER and ORR pathways can be simulated at the atomic level. This approach helps identify the rate-determining steps and optimize the catalytic activity of air electrodes. Liu *et al.* investigated the energy barriers for OER and ORR on cubic $Ba_{0.5}Sr_{0.5}Co_{0.8}Fe_{0.2}O_{3-\delta}$ (C-BSCF) and hexagonal $Ba_4Sr_4(Co_{0.8}Fe_{0.2})_4O_{16-\delta}$ (H-BSCF) surfaces to understand their mechanisms in P-SOCs air electrodes.[214] They determined the most stable surface configurations by evaluating various A- and B-site arrangements and surface terminations. The results revealed that C-BSCF has a higher energy barrier of 3.25 eV for OER mainly due to limited proton conduction whereas H-BSCF requires a lower barrier of 1.15 eV, highlighting its superior proton migration capability. Conversely, H-BSCF faces a 2.03 eV barrier for oxygen desorption while C-BSCF performs better in this regard. The hybrid $Ba_{1.5}Sr_{1.5}Co_{1.6}Fe_{0.4}O_{7-\delta}$ (C/H-BSCF) electrode combines the advantages of both phases, with initial water decomposition occurring on the cubic phase and further decomposition and oxygen desorption on the hexagonal phase. For ORR, C-BSCF shows a more favorable oxygen reduction process with a significant advantage over H-BSCF which has lower energy barriers for oxygen adsorption and desorption (Fig. 14(i)). Overall, the C/H-BSCF hybrid electrode benefits from enhanced ORR and OER activities due to the synergistic effects of combining cubic and hexagonal phases. When examining complex hybrid air electrodes, it is often highly effective to investigate the microscopic mechanisms of oxygen reactions with theoretical calculations.

In composite air electrode PBCC–BCO constructed by Zhou *et al.*, the H_2O adsorption and oxygen evolution are favored on BCO with ΔG values of 0.099 eV (H_2O adsorption) and 0.62 eV (oxygen evolution) for BCO, compared to 1.794 eV (H_2O adsorption) and 1.055 eV (oxygen evolution) for PBCC at 600 °C.[194] The PBCC surface, on the other hand, is more favorable for O_2 formation and desorption (1.307 eV for BCO *vs.* −0.823 eV for PBCC at 600 °C). Combined with DOS, the proposed OER sequence for the PBCC–BCO air electrode involves initial H_2O absorption on the BCO (110) surface, where it dissociated into $^*OH$ and $^*H$. The $^*OH$ intermediate is then further dissociated into $^*O$ and $^*H$ on BCO (110), and finally, O_2 is formed and desorbed on PBCC (010). This sequence highlights the combined effects of rapid H_2O dissociation on BCO NPs and fast oxygen desorption on PBCC in enhancing OER activity.

7. Pre-commercialization considerations

Renewable energy sources now contribute more than 29% of global electricity generation, with countries like Australia reaching levels as high as 35%.[504] Several large-scale hydrogen plants have recently been launched worldwide by corporations including European Energy in Denmark,[505] TotalEnergies in French,[506] and German Aerospace Center in Germany.[507] By integrating electrolysis with renewable energy sources, fuels and chemicals production can move away from fossil fuels dependence, achieving the development of a fully renewable energy system. P-SOCs offer a reliable and affordable solution to incorporate green energy into the current energy infrastructure. This chapter outlines key factors to address before P-SOCs technology can be fully commercialized.

7.1. Scaling up from lab to industry

Lab-scale P-SOCs are generally designed with compact sizes, for instance, O'Hayre, Shao, and Duan *et al.* report active areas of just around 1 cm^2 for their P-SOCs.[9,81] This small scale is suitable for laboratory research, where studies focus on optimizing electrode materials, cell structure, and performance parameters under controlled conditions. However, for practical applications, P-SOCs must be significantly larger to meet the energy demands of real-world systems (10^2 W for electronic devices and 10^4 W for electronic vehicles). Application-oriented P-SOCs typically adopt a planar or tubular design to increase surface area and enhance efficiency. Currently, numerous studies have explored larger-scale P-SOCs (as shown in Fig. 15(a) and Table 2) including 12 × 12 cm^2 planar designs and 8 cm^2 tubular configurations.[161,162] However, despite these increased sizes, the total output power remains insufficient to operate electronic devices. The production capacity of a P-SOC plant is directly proportional to the total active area. Expanding the active area at the individual cell level and assembling multiple cells into stacks are the two most straightforward methods to increase output.[508,509] Scaling up requires addressing challenges such as maintaining mechanical integrity,

This journal is © The Royal Society of Chemistry 2025

*Energy Environ. Sci.*, 2025, **18**, 4555–4595 | **4581**
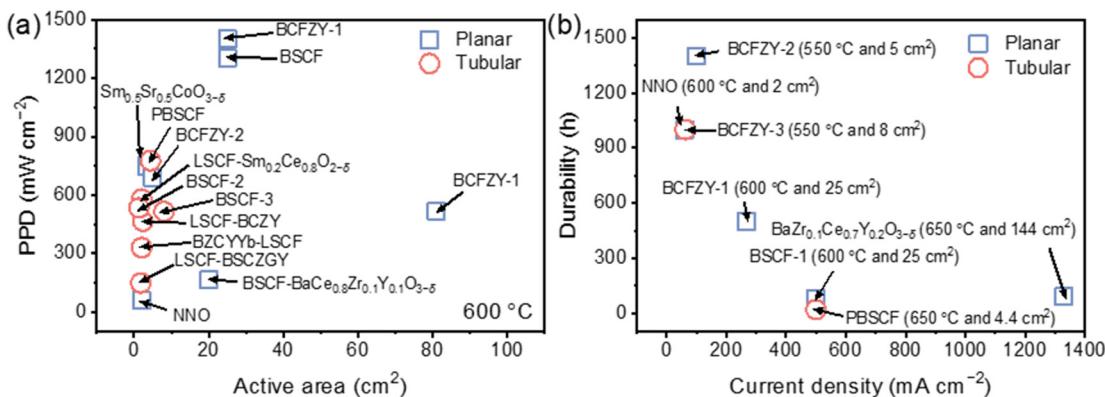
Fig. 15   Large-area P-SOCs: (a) PPDs at 600 °C and (b) durability (data detailed in Table 2).

Table 2   Application-oriented P-SOC air electrodes design

Air electrode	Area (cm^2)	PPD at 600 °C (mW cm^{-2})	Current density at 1.3 V (mA cm^{-2})	Stability (h)	Ref.
Planar					
$BaCe_{0.2}Zr_{0.7}Y_{0.1}O_{3-\delta}$	135			400 h (ASR)	512
$BaZr_{0.1}Ce_{0.7}Y_{0.2}O_{3-\delta}$	144			90 h (650 °C and 1330 mA cm^{-2})	162
$Ba_{0.5}Sr_{0.5}Co_{0.8}Fe_{0.2}O_{3-\delta}$–$BaCe_{0.8}Zr_{0.1}Y_{0.1}O_{3-\delta}$ (BSCF–BCZY)	20	165		3000 h (600 °C, 170 mA cm^{-2} and −100 mA cm^{-2})	285
$Ba_{0.5}Sr_{0.5}Co_{0.8}Fe_{0.2}O_{3-\delta}$ (BSCF-1)	25	1302		80 h (550 °C and 500 mA cm^{-2})	513
$BaCo_{0.4}Fe_{0.4}Zr_{0.1}Y_{0.1}O_{3-\delta}$ (BCFZY-1)	81	518			514
BCFZY-1	25	1400		500 h (550 °C and 267 mA cm^{-2})	514
$BaCo_{0.4}Fe_{0.4}Zr_{0.1}Y_{0.1}O_{3-\delta}$ (BCFZY-2)	5	690		1400 h (550 °C and 100 mA cm^{-2})	515
$Nd_2NiO_{4+\delta}$ (NNO)	2.01	60		1000 h (600 °C at 60 mA cm^{-2})	516
$Sm_{0.5}Sr_{0.5}CoO_{3-\delta}$ (SSC)	3.33	747			517
Tubular					
$BaZr_{0.1}Ce_{0.7}Y_{0.1}Yb_{0.1}O_{3-\delta}$–$La_{0.6}Sr_{0.4}Co_{0.2}Fe_{0.8}O_{3-\delta}$ (BZCYYb–LSCF)	2	331			518
$La_{0.6}Sr_{0.4}Co_{0.2}Fe_{0.8}O_{3-\delta}$–$Ba_{0.5}Sr_{0.5}Ce_{0.6}Zr_{0.2}Gd_{0.1}Y_{0.1}O_{3-\delta}$ (LSCF–BSCZGY)	1.79	150		96 h (700 °C and 0.7 V)	519
BCFZY-3	8	517	915	1000 h (550 °C and 0.062 A cm^{-2})	161
$La_{0.6}Sr_{0.4}Co_{0.2}Fe_{0.8}O_{3-\delta}$–$Sm_{0.2}Ce_{0.8}O_{2-\delta}$ (LSCF–$Sm_{0.2}Ce_{0.8}O_{2-\delta}$)	2	580			520
$La_{0.6}Sr_{0.4}Co_{0.2}Fe_{0.8}O_{3-\delta}$–$BaCe_{0.7}Zr_{0.1}Y_{0.2}O_{3-\delta}$ (LSCF–BCZY)	2.3	465		70 h (600 °C and 0.7 V)	521
$Ba_{0.5}Sr_{0.5}Co_{0.8}Fe_{0.2}O_{3-\delta}$ (BSCF-2)	1.29	534			359
$PrBa_{0.5}Sr_{0.5}Co_{1.5}Fe_{0.5}O_{5+\delta}$ (PBSCF)	4.4	776		20 h (650 °C and 0.5 A cm^{-2})	522

achieving uniform gas distribution, and managing thermal stresses across a larger area. In particular, the design must ensure durability and stable performance under operating conditions that differ from the controlled lab environment (Fig. 15(b)), making factors like material selection, sealing methods, and thermal management crucial to the development of commercial-scale P-SOCs systems.[510,511]

7.2.   Key challenges for commercialization

As an air electrode material progresses toward practical applications, the criteria for evaluating its performance shift accordingly. Several practical considerations must be addressed, spanning technical, economic, and market-related factors. A primary concern is production scalability, which requires the development of cost-effective synthesis methods and dependable supply chains for essential raw materials such as Ba and Co. The traditional approaches for fabricating perovskite electrode

materials include molten salt synthesis, hydrothermal reaction, sol–gel synthesis, and solid-state method. Each method plays a crucial role in determining phase purity, microstructure, defect concentration, and ionic/electronic transport properties, which directly impact electrode performance in P-SOCs. The hydrothermal method, performed under low-temperature ($\sim$150–300 °C) and high-pressure conditions, enables fine morphology control and low-defect-density perovskites, which enhance proton and oxygen ion transport, but scalability remains a challenge due to high-pressure requirements.[523,524] Molten salt synthesis is an emerging technique that allows for the formation of highly crystalline, defect-engineered perovskites at around 800 °C by utilizing molten salts as a reaction medium to promote controlled grain growth and enhanced ionic diffusion, which improves oxygen vacancy mobility and catalytic activity.[525] The sol–gel method, operating at a relatively low calcination temperature ($\sim$600–900 °C), facilitates the synthesis of nanostructured perovskites

with a high surface area and uniform dopant distribution while preserving porosity and enhancing gas diffusion. These characteristics contribute to improved catalytic activity and ionic conductivity. However, potential issues such as organic solvent impurities, phase separation require careful management, unavailability and high price of the corresponding salts.[526] Conversely, the solid-state reaction method, the most cost-effective and scalable approach for large-scale perovskite production, involves high-temperature calcination ($\sim$1000–1400 $^{\circ}$C) of mixed solid precursors, producing highly crystalline and thermodynamically stable perovskites with superior bulk electronic conductivity. However, this approach often results in large grain sizes with a low surface area, leading to non-uniform dopant distribution that may necessitate additional grinding or doping strategies for optimization.[527] Additionally, advanced electrode structuring techniques such as freeze-casting, sacrificial templating, and 3D printing can help create highly porous, hierarchical structures that enhance both electronic and ionic transport without compromising mechanical integrity. Moreover, roll-to-roll processing and screen-printing techniques offer promising routes for integrating perovskite electrodes into commercial-scale P-SOCs with high reproducibility and cost efficiency.[528,529] By implementing these strategies, the transition from research to commercialization can be accelerated. Achieving competitive costs is crucial, necessitating reductions in manufacturing expenses through process optimization, material efficiency, and economies of scale.

Performance improvement also remains essential, particularly in enhancing outputs, efficiency, and lifespan, to ensure that P-SOCs can meet the rigorous demands of high-performance applications like electric vehicles and energy storage systems. In addition to technical and economic considerations, practical deployment of P-SOCs requires attention to delivery logistics, safety, and recycling strategies.[530–532] Efficient delivery systems ensure that both raw materials and finished products reach their destinations securely and cost-effectively, with protective packaging, optimized shipping routes, and local distribution centers to minimize damage and costs. Safety is also critical, especially given the high operating temperatures and reactivity of materials in P-SOCs; ensuring thermal stability, reliable sealing, and resistance to environmental stress are essential for operational integrity. Finally, recycling strategies are needed to recover valuable materials like Co from spent cells, reducing reliance on raw material extraction and supporting sustainable production. Together, these considerations enable P-SOC technology to be deployed safely, sustainably, and at scale.

8. Challenges and prospects

In the intermediate-to-low temperature range, state-of-the-art P-SOCs continue to exhibit suboptimal performance compared to conventional O-SOCs.[533] Air electrodes for P-SOCs have garnered significant interest due to their high polarization resistance, yet no truly successful air electrode material has emerged, unlike the established LSM and LSCF for O-SOCs. A review of the latest advancements in P-SOC air electrodes shows that the BCO series achieves the lowest ASR (Fig. 16(a) and (b)), with $LnBaM_2O_{6+\delta}$ double perovskite materials following closely (Fig. 16(c)). In contrast, Fe-based materials typically demonstrate less remarkable performance (Fig. 16(d)). To minimize the resistance of P-SOCs device and enhance both power output and hydrogen production efficiency, the BCO series may emerge as a key focus in future research efforts (Fig. 16).

Lowering operational temperatures is crucial for sustainability, as it reduces costs, enhances market feasibility, and opens the door for portable and transportable applications. Although P-SOCs operate at lower temperatures than O-SOCs—down to 350 $^{\circ}$C—their performance remains insufficient for practical applications (Fig. 16(e)–(g)).[236] At low temperatures, the primary challenge is typically the slow kinetics of ORR and OER. Current research often focuses on modifying existing air electrodes to enhance proton conduction, resulting in numerous variations and studies but limited genuine innovation. As operating temperatures continue to decrease, combining insights from low-temperature catalytic systems, such as PEM and anion exchange membranes, could offer valuable inspiration. For instance, low-temperature catalysis often achieves performance optimization through controlled crystal orientation and complex surface interface design. Furthermore, the reduced operating temperature enables direct observation of microevolution within the P-SOCs system. Advanced characterization techniques, including in situ TEM, can provide insights into the underlying mechanisms, thereby aiding and expediting the development of advanced air electrode materials.

Ensuring stable operation is a key aspect of optimizing both power generation and hydrogen production in P-SOCs, directly impacting efficiency, reliability, and system lifespan. Current treatment methods for air electrode materials like segregation, can raise concerns about durability. The failure of P-SOCs during operation may also arise from interface issues stemming from the thermal expansion differences between the electrode and the electrolyte. Improving the electrolyte/electrode interface is essential for enhancing air electrode. Given the complexity of the composition and elements in perovskite air electrode materials, employing AI-driven design can significantly speed up the material development process. Moreover, the P-SOC system is strongly influenced by physical factors like temperature and pressure. Finite element analysis can be applied to assess and forecast the performance of P-SOC devices in real-world operating environments.[534]

Lab-scale experiments are crucial for developing new technologies as they provide essential data for subsequent pilot and industrial-scale investigations. The reliability of this experimental data is vital as it guides future research directions, especially in the development of SOC technology for electrochemical energy storage and conversion which is key for achieving a net-zero carbon society. However, the complexity of lab-scale testing involving multiple parameters such as cell configuration, performance measurement strategies, and temperature distribution, can obscure true cell performance and affect power output. Discrepancies in results often arise from the omission of important parameter information in reports,

This journal is © The Royal Society of Chemistry 2025

Energy Environ. Sci., 2025, **18**, 4555–4595 | **4583**
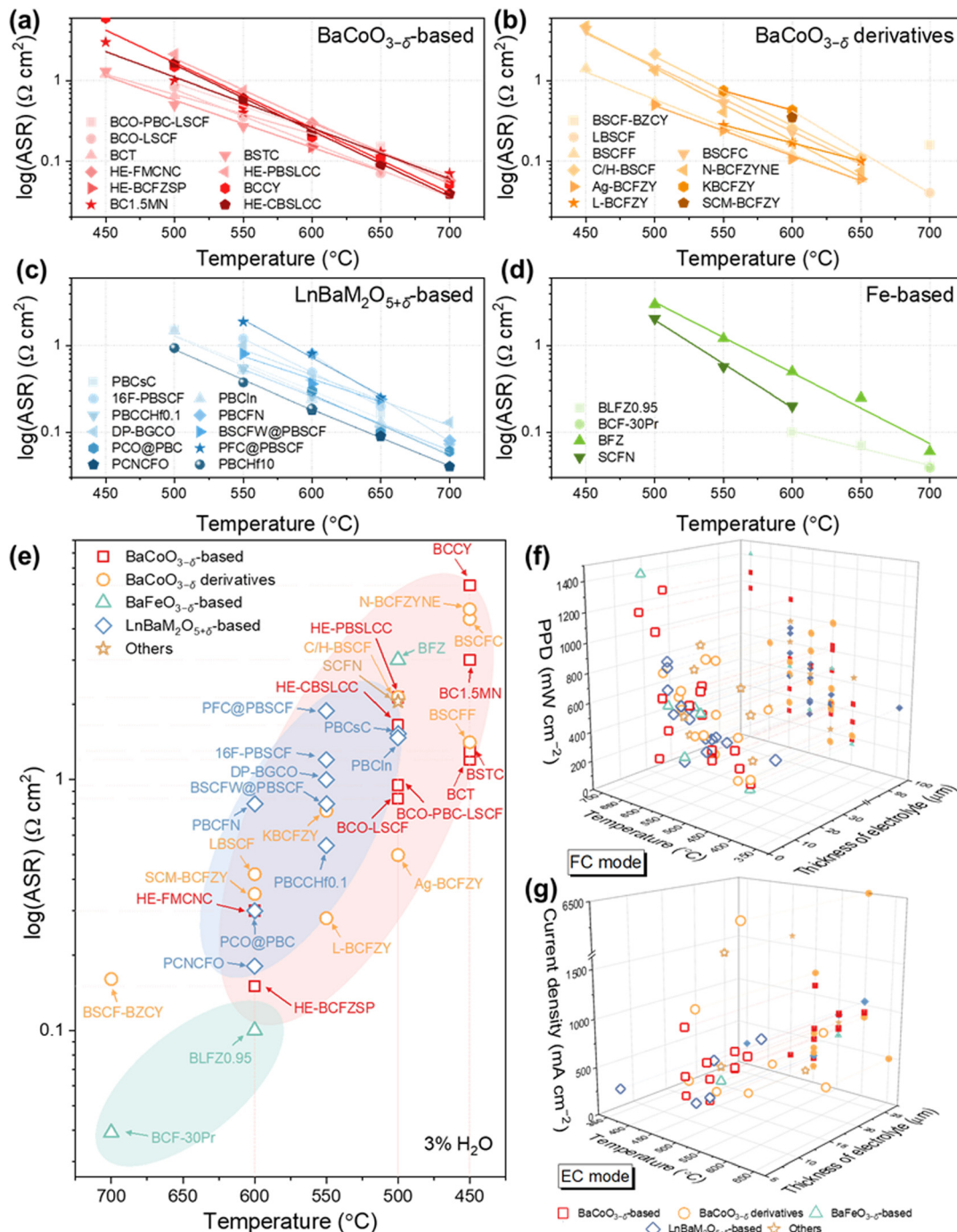
Fig. 16 Comparison of ASR in symmetrical cell configuration of advanced air electrodes for P-SOCs at 3% H_2O: (a) $BaCoO_{3-\delta}$-based perovskites, (b) $BaCoO_{3-\delta}$-derivated perovskites, (c) $LnBaM_2O_{6+\delta}$-based perovskites, and (d) Fe-based perovskites. Summary of electrochemical properties of advanced perovskite air electrode materials (detailed data summarized in Table 1): (e) ASR of lowest working temperature in symmetrical cells configuration, (f) PPDs in fuel cell (FC) mode, and (g) current densities in electrolysis cell (EC) mode.

leading to significant variances in literature. To facilitate reliable comparisons in future research, it is recommended that detailed information on various parameters including cell size, surface area ratios, sealing methods, and flow rates, be consistently provided.[163] Additionally, the extra heat produced due to irreducible internal resistance during testing may lead to actual operating temperatures significantly exceeding the

recorded values. This discrepancy underscores the need for more precisely defined experimental conditions.

Despite extensive research, commercial implementation of P-SOCs systems still has not materialized because of insufficient power outputs and high cost.[34] Various considerations must be addressed during the laboratory stage to effectively align with commercial goals including the costs and availability

4584 | Energy Environ. Sci., 2025, 18, 4555–4595

This journal is © The Royal Society of Chemistry 2025

of raw materials, expanded cells area and electrolyte sealing, safety and lifespan during storage and transportation, as well as the recyclability and environmental impact of waste P-SOCs.[535,536] Consequently, it is advisable, in the early phases of research and development, to choose air electrode materials that are low-cost, safe, and environmentally friendly. This approach ensures that the materials are not only functional but also viable for future commercial applications.

Author contributions

C. P. and X. X. contributed to the central idea and conducted the draft. S. M. collected resources. P. K., Y. Z., and X. X. contributed to the writing and editing of the document.

Data availability

No primary research results, software or code have been included and no new data were generated or analysed as part of this review.

Conflicts of interest

There are no conflicts to declare.

Acknowledgements

References

1 X. Yang, C. P. Nielsen, S. Song and M. B. McElroy, *Nat. Energy*, 2022, **7**, 955–965.
2 I. Cho, J. Yun, B. Seong, J. Kim, S. H. Choi, H.-I. Ji and S. Choi, *J. Energy Chem.*, 2024, **88**, 1–9.
3 X. Xu, X. Han, Y. Zheng, W. Zhou, K. Davey and S.-Z. Qiao, *Chem Catal.*, 2023, **3**, 100794.
4 S. Tao and J. T. Irvine, *Chem. Rev.*, 2004, **4**, 83–95.
5 I. Jang, S. A. C. Juliana, J. O. Crawford, Y. J. Cho, S. Parvin, D. A. Gonzalez-Casamachin, J. Baltrusaitis, R. P. Lively and E. Nikolla, *Chem. Rev.*, 2024, **124**, 8233–8306.
6 C. Korte, A. Peters, J. Janek, D. Hesse and N. Zakharov, *Phys. Chem. Chem. Phys.*, 2008, **10**, 4623–4635.
7 A. Peters, C. Korte, D. Hesse, N. Zakharov and J. Janek, *Solid State Ionics*, 2007, **178**, 67–76.
8 L. Bi, S. Boulfrad and E. Traversa, *Chem. Soc. Rev.*, 2014, **43**, 8255–8270.
9 C. Duan, R. Kee, H. Zhu, N. Sullivan, L. Zhu, L. Bian, D. Jennings and R. O'Hayre, *Nat. Energy*, 2019, **4**, 230–240.
10 S. D. Ebbesen, S. H. Jensen, A. Hauch and M. B. Mogensen, *Chem. Rev.*, 2014, **114**, 10697–10734.
11 C. Tien, *Trans. Phenom. Plasma*, 1969, **5**, 253–324.
12 E. Tezel, A. Whitten, G. Yarema, R. Denecke, J.-S. McEwen and E. Nikolla, *ACS Catal.*, 2022, **12**, 11456–11471.
13 Y. Zheng, J. Wang, B. Yu, W. Zhang, J. Chen, J. Qiao and J. Zhang, *Chem. Soc. Rev.*, 2017, **46**, 1427–1463.
14 C. Gunathilake, I. Soliman, D. Panthi, P. Tandler, O. Fatani, N. A. Ghulamullah, D. Marasinghe, M. Farhath, T. Madhujith and K. Conrad, *Chem. Soc. Rev.*, 2024, **53**, 10900–10969.
15 J. Cao, Y. Ji and Z. Shao, *Energy Environ. Sci.*, 2022, **15**, 2200–2232.
16 Z. Luo, Z. Wang, T. Zhu, Y. Song, Z. Lin, S. Jiang, Z. Zhu and Z. Shao, *Energy Environ. Sci.*, 2024, **17**, 6873–6896.
17 Z. Shao and M. O. Tadé, *Chem. Soc. Rev.*, 2016, **37**, 1568.
18 J. Cao, Y. Ji and Z. Shao, *Chem. Soc. Rev.*, 2024, **53**, 450–501.
19 F. Liu, D. Ding and C. Duan, *Adv. Sci.*, 2023, **10**, 2206478.
20 N. Wang, C. Tang, L. Du, R. Zhu, L. Xing, Z. Song, B. Yuan, L. Zhao, Y. Aoki and S. Ye, *Adv. Energy Mater.*, 2022, **12**, 2201882.
21 M. Wang, C. Su, Z. Zhu, H. Wang and L. Ge, *Composites, Part B*, 2022, **238**, 109881.
22 C. Duan, J. Tong, M. Shang, S. Nikodemski, M. Sanders, S. Ricote, A. Almansoori and R. O'Hayre, *Science*, 2015, **349**, 1321–1326.
23 Z. Wang, Z. Luo, H. Xu, T. Zhu, D. Guan, Z. Lin, T.-S. Chan, Y.-C. Huang, Z. Hu, S. P. Jiang and Z. Shao, *Adv. Funct. Mater.*, 2024, 2402716, DOI: **10.1002/adfm.202402716**.
24 C. Tang, Y. Yao, N. Wang, X. Zhang, F. Zheng, L. Du, D. Luo, Y. Aoki and S. Ye, *InfoMat*, 2024, **6**, e12515.
25 L. Wang, R. Merkle and J. Maier, *J. Electrochem. Soc.*, 2010, **157**, B1802.
26 Y. Wang, Y. Ling, B. Wang, G. Zhai, G. Yang, Z. Shao, R. Xiao and T. Li, *Energy Environ. Sci.*, 2023, **16**, 5721–5770.
27 P. Kazempoor and R. J. Braun, *Int. J. Hydrogen Energy*, 2014, **39**, 2669–2684.
28 F. Gallucci, F. Chiaravalloti, S. Tosti, E. Drioli and A. Basile, *Int. J. Hydrogen Energy*, 2007, **32**, 1837–1845.
29 Z. Wang, X. Zhou, L. Liu, H. Chen, X. Qian, F. He, Y. Sheng and X. Jiang, *J. Chin. Ceram. Soc.*, 2023, **51**, 2689–2699.
30 C. Duan, J. Huang, N. Sullivan and R. O'Hayre, *Appl. Phys. Rev.*, 2020, **7**, 011314.
31 B. Yuan, N. Wang, C. Tang, L. Meng, L. Du, Q. Su, Y. Aoki and S. Ye, *Nano Energy*, 2024, **122**, 109306.
32 M. Papac, V. Stevanovic, A. Zakutayev and R. O'Hayre, *Nat. Mater.*, 2021, **20**, 301–313.
33 W. Zhang, M. Liu, X. Gu, Y. Shi, Z. Deng and N. Cai, *Chem. Rev.*, 2023, **123**, 7119–7192.
34 Z. Wang, Y. Wang, J. Wang, Y. Song, M. J. Robson, A. Seong, M. Yang, Z. Zhang, A. Belotti, J. Liu, G. Kim, J. Lim, Z. Shao and F. Ciucci, *Nat. Catal.*, 2022, **5**, 777–787.
35 T. Cooper, J. R. Scheffe, M. E. Galvez, R. Jacot, G. Patzke and A. Steinfeld, *Energy Technol.*, 2015, **3**, 1130–1142.
36 R. Jacobs, T. Mayeshiba, J. Booske and D. Morgan, *Adv. Energy Mater.*, 2018, **8**, 1702708.
37 N. Ramadass, *Mater. Sci. Eng., B*, 1978, **36**, 231–239.

This journal is © The Royal Society of Chemistry 2025

Energy Environ. Sci., 2025, **18**, 4555–4595 | **4585**

38 Y. Song, X. Zhang, K. Xie, G. Wang and X. Bao, *Adv. Mater.*, 2019, **31**, 1902033.

39 J. Jing, J. Pang, L. Chen, H. Zhang, Z. Lei and Z. Yang, *Chem. Eng. J.*, 2022, **429**, 132314.

40 K. Zhu, H. Liu, X. Li, Q. Li, J. Wang, X. Zhu and W. Yang, *Electrochim. Acta*, 2017, **241**, 433–439.

41 Q. Zhang, J. Ding and M. He, *J. Phys. Chem. Solids*, 2017, **108**, 76–81.

42 C. S. Choi and E. Prince, *Acta Crystallogr.*, 1972, **28**, 2857–2862.

43 J. Kim, S. Sengodan, G. Kwon, D. Ding, J. Shin, M. Liu and G. Kim, *ChemSusChem*, 2014, **7**, 2811–2815.

44 P. Ding, W. Li, H. Zhao, C. Wu, L. Zhao, B. Dong and S. Wang, *JPhys Mater.*, 2021, **4**, 022002.

45 A. Kushima, D. Parfitt, A. Chroneos, B. Yildiz, J. A. Kilner and R. W. Grimes, *Phys. Chem. Chem. Phys.*, 2011, **13**, 2242–2249.

46 Y. Huan, S. Chen, R. Zeng, T. Wei, D. Dong, X. Hu and Y. Huang, *Adv. Energy Mater.*, 2019, **9**, 1901573.

47 O. F. Schirmer, *J. Phys.: Condens. Matter*, 2006, **18**, R667–R704.

48 A. J. Rettie, W. D. Chemelewski, D. Emin and C. B. Mullins, *J. Phys. Chem. Lett.*, 2016, **7**, 471–479.

49 D. Neagu and J. T. S. Irvine, *Chem. Mater.*, 2011, **23**, 1607–1617.

50 L. Tai, M. Nasrallah, H. Anderson, D. Sparlin and S. Sehlin, *Solid State Ionics*, 1995, **76**, 259–271.

51 R. Raffaelle, H. U. Anderson, D. M. Sparlin and P. E. Parris, *Phys. Rev. Lett.*, 1990, **65**, 1383–1386.

52 X. Liu, H. Zhao, J. Yang, Y. Li, T. Chen, X. Lu, W. Ding and F. Li, *J. Membr. Sci.*, 2011, **383**, 235–240.

53 S. Kirkpatrick, *Rev. Mod. Phys.*, 1973, **45**, 574–588.

54 D. Kim, S. Miyoshi, T. Tsuchiya and S. Yamaguchi, *Solid State Ionics*, 2014, **262**, 875–878.

55 A. S. Foster, A. L. Shluger and R. M. Nieminen, *Phys. Rev. Lett.*, 2002, **89**, 225901.

56 L. J. Duckers, *Phys. Lett.*, 1978, **67A**, 93–94.

57 Y. Ji and Y. Luo, *J. Am. Chem. Soc.*, 2016, **138**, 15896–15902.

58 C. L. Fu, M. Krčmar, G. S. Painter and X.-Q. Chen, *Phys. Rev. Mater.*, 2007, **99**, 225502.

59 J. Cao, C. Su, Y. Ji, G. Yang and Z. Shao, *J. Energy Chem.*, 2021, **57**, 406–427.

60 S. J. Skinner and J. A. Kilner, *Solid State Ionics*, 2000, **135**, 709–712.

61 C. Munnings, S. Skinner, G. Amow, P. Whitfield and I. Davidson, *Solid State Ionics*, 2005, **176**, 1895–1901.

62 A. Chroneos, D. Parfitt, J. A. Kilner and R. W. Grimes, *J. Mater. Chem.*, 2010, **20**, 266–270.

63 A. Grimaud, F. Mauvy, J. M. Bassat, S. Fourcade, L. Rocheron, M. Marrony and J. C. Grenier, *J. Electrochem. Soc.*, 2012, **159**, B683–B694.

64 Y. Yamazaki, P. Babilo and S. M. Haile, *Chem. Mater.*, 2008, **20**, 6352–6357.

65 I. Zvonareva, X.-Z. Fu, D. Medvedev and Z. Shao, *Energy Environ. Sci.*, 2022, **15**, 439–465.

66 K. D. Kreuer, *Annu. Rev. Mater. Res.*, 2003, **33**, 333–359.

67 K. D. Kreuer, *Chem. Mater.*, 1996, **8**, 610–641.

68 K. D. Kreuer, *Solid State Ionics*, 1999, **125**, 285–302.

69 H. Uchida, N. Maeda and H. Iwahara, *Solid State Ionics*, 1983, **11**, 117–124.

70 D. Poetzsch, R. Merkle and J. Maier, *Faraday Discuss.*, 2015, **182**, 129–143.

71 D. Poetzsch, R. Merkle and J. Maier, *Adv. Funct. Mater.*, 2015, **25**, 1542–1557.

72 N. Wang, S. Hinokuma, T. Ina, H. Toriumi, M. Katayama, Y. Inada, C. Zhu, H. Habazaki and Y. Aoki, *Chem. Mater.*, 2019, **31**, 8383–8393.

73 E. Fabbri, D. Pergolesi and E. Traversa, *Chem. Soc. Rev.*, 2010, **39**, 4355–4369.

74 T. Scherban, R. Villeneuve, L. Abello and G. Lucazeau, *Solid State Ionics*, 1993, **61**, 93–98.

75 T. Ueki and M. Watanabe, *Macromolecules*, 2008, **41**, 3739.

76 K. D. Kreuer, A. Rabenau and W. Weppner, *Angew. Chem., Int. Ed. Engl.*, 1982, **21**, 208–209.

77 J. Kim, S. Sengodan, S. Kim, O. Kwon, Y. Bu and G. Kim, *Renewable Sustainable Energy Rev.*, 2019, **109**, 606–618.

78 P. Ramaswamy, N. E. Wong and G. K. Shimizu, *Chem. Soc. Rev.*, 2014, **43**, 5913–5932.

79 G. Geneste, *Solid State Ionics*, 2018, **323**, 172–202.

80 M. Li, M. Zhao, F. Li, W. Zhou, V. K. Peterson, X. Xu, Z. Shao, I. Gentle and Z. Zhu, *Nat. Commun.*, 2017, **8**, 13990.

81 Z. Li, X. Mao, D. Feng, M. Li, X. Xu, Y. Luo, L. Zhuang, R. Lin, T. Zhu, F. Liang, Z. Huang, D. Liu, Z. Yan, A. Du, Z. Shao and Z. Zhu, *Nat. Commun.*, 2024, **15**, 9318.

82 H. Dai, Y. Yin, X. Li, C. Ma, Z. Chen, M. Hua and L. Bi, *Sustainable Mater. Technol.*, 2022, **32**, e00409.

83 R. Ren, Z. Wang, X. Meng, X. Wang, C. Xu, J. Qiao, W. Sun and K. Sun, *ACS Appl. Energy Mater.*, 2020, **3**, 4914–4922.

84 S. Choi, C. J. Kucharczyk, Y. Liang, X. Zhang, I. Takeuchi, H.-I. Ji and S. M. Haile, *Nat. Energy*, 2018, **3**, 202–210.

85 Y. Yin, D. Xiao, S. Wu, E. H. Da'as, Y. Gu and L. Bi, *Susmat*, 2023, **3**, 697–708.

86 Y. Yin, Y. Zhou, Y. Gu and L. Bi, *J. Adv. Ceram.*, 2023, **12**, 587–597.

87 Y. Lin, R. Ran, Y. Zheng, Z. Shao, W. Jin, N. Xu and J. Ahn, *J. Power Sources*, 2008, **180**, 15–22.

88 E. Fabbri, D. Pergolesi, S. Licoccia and E. Traversa, *Solid State Ionics*, 2010, **181**, 1043–1051.

89 Y. Yamazaki, F. Blanc, Y. Okuyama, L. Buannic, J. C. Lucio-Vega, C. P. Grey and S. M. Haile, *Nat. Mater.*, 2013, **12**, 647–651.

90 M. Yu, Q. Feng, Z. Liu, P. Zhang, X. Zhu and S. Mu, *Crystals*, 2024, **14**, 225.

91 R. Zohourian, R. Merkle, G. Raimondi and J. Maier, *Adv. Funct. Mater.*, 2018, **28**, 1801241.

92 K. Bae, D. Y. Jang, H. J. Choi, D. Kim, J. Hong, B. K. Kim, J. H. Lee, J. W. Son and J. H. Shim, *Nat. Commun.*, 2017, **8**, 14553.

93 Z. Wang, W. Yang, S. P. Shafi, L. Bi, Z. Wang, R. Peng, C. Xia, W. Liu and Y. Lu, *J. Mater. Chem. A*, 2015, **3**, 8405–8412.

94 E. Fabbri, I. Markus, L. Bi, D. Pergolesi and E. Traversa, *Solid State Ionics*, 2011, **202**, 30–35.

4586 | *Energy Environ. Sci.*, 2025, **18**, 4555–4595

This journal is © The Royal Society of Chemistry 2025

95 Z. Tao, L. Bi, Z. Zhu and W. Liu, *J. Power Sources*, 2009, **194**, 801–804.

96 E. Fabbri, L. Bi, D. Pergolesi and E. Traversa, *Energy Environ. Sci.*, 2011, **4**, 4984.

97 J. Choi, B. Kim, S.-H. Song and J.-S. Park, *Int. J. Hydrogen Energy*, 2016, **41**, 9619–9626.

98 J. Dailly, G. Taillades, M. Ancelin, P. Pers and M. Marrony, *J. Power Sources*, 2017, **361**, 221–226.

99 D. Kim, T. K. Lee, S. Han, Y. Jung, D. G. Lee, M. Choi and W. Lee, Mater, *Today Energy*, 2023, **36**, 101365.

100 H. Zhu, S. Ricote, C. Duan, R. P. O'Hayre, D. S. Tsvetkov and R. J. Kee, *J. Electrochem. Soc.*, 2018, **165**, F581–F588.

101 D. K. Lim, C. J. Park, M. B. Choi, C. N. Park and S. J. Song, *Int. J. Hydrogen Energy*, 2010, **35**, 10624–10629.

102 H. Zhu and R. J. Kee, *Int. J. Hydrogen Energy*, 2016, **41**, 2931–2943.

103 C. Duan, D. Hook, Y. Chen, J. Tong and R. O'Hayre, *Energy Environ. Sci.*, 2017, **10**, 176–182.

104 E. Fabbri, L. Bi, D. Pergolesi and E. Traversa, *Adv. Mater.*, 2012, **24**, 195–208.

105 D. Chen, C. Chen, Z. M. Baiyee, Z. Shao and F. Ciucci, *Chem. Rev.*, 2015, **115**, 9869–9921.

106 W. T. Hong, M. Risch, K. A. Stoerzinger, A. Grimaud, J. Suntivich and Y. Shao-Horn, *Energy Environ. Sci.*, 2015, **8**, 1404–1427.

107 Y.-L. Lee, J. Kleis, J. Rossmeisl, Y. Shao-Horn and D. Morgan, *Energy Environ. Sci.*, 2011, **4**, 3966.

108 E. D. Wachsman and K. T. Lee, *Science*, 2011, **334**, 935–939.

109 D. N. Mueller, M. L. Machala, H. Bluhm and W. C. Chueh, *Nat. Commun.*, 2015, **6**, 6097.

110 J. Suntivich, W. T. Hong, Y.-L. Lee, J. M. Rondinelli, W. Yang, J. B. Goodenough, B. Dabrowski, J. W. Freeland and Y. Shao-Horn, *J. Phys. Chem. C*, 2014, **118**, 1856–1863.

111 J. Suntivich, H. A. Gasteiger, N. Yabuuchi, H. Nakanishi, J. B. Goodenough and Y. Shao-Horn, *Nat. Chem.*, 2011, **3**, 546–550.

112 W. T. Hong, K. A. Stoerzinger, B. Moritz, T. P. Devereaux, W. Yang and Y. Shao-Horn, *J. Phys. Chem. C*, 2015, **119**, 2063–2072.

113 K. Li, Y. Liang, J. Zhang, B. Yu and L. Jia, *Int. J. Hydrogen Energy*, 2024, **91**, 858–866.

114 R. Peng, T. Wu, W. Liu, X. Liu and G. Meng, *J. Mater. Chem.*, 2010, **20**, 6218.

115 E. Fabbri, D. Pergolesi and E. Traversa, *Sci. Technol. Adv. Mater.*, 2010, **11**, 044301.

116 R. Majee, Q. A. Islam, S. Mondal and S. Bhattacharyya, *Chem. Sci.*, 2020, **11**, 10180–10189.

117 Y. Yuan, R. K. Patel, S. Banik, T. B. Reta, R. S. Bisht, D. D. Fong, S. Sankaranarayanan and S. Ramanathan, *Chem. Rev.*, 2024, **124**, 9733–9784.

118 H. Tellez Lozano, J. Druce, S. J. Cooper and J. A. Kilner, *Sci. Technol. Adv. Mater.*, 2017, **18**, 977–986.

119 H. Hayashi, H. Inaba, M. Matsuyama, N. G. Lan, M. Dokiya and H. Tagawa, *Solid State Ionics*, 1999, **122**, 1–15.

120 J. A. Kilner and R. J. Brook, *Solid State Ionics*, 1982, **6**, 237–252.

121 M. S. Islam, *Solid State Ionics*, 2002, **154–155**, 75–85.

122 A. F. Sammells, R. L. Cook, J. H. White, J. J. Osborne and R. C. MacDuff, *Solid State Ionics*, 1992, **52**, 111–123.

123 M. A. Peña and L. G. Fierro, *Chem. Rev.*, 2001, **101**, 1981–2017.

124 L. Liang, L. Wencong and C. Nianyi, *J. Phys. Chem. Solids*, 2004, **65**, 855–860.

125 H. Yokokawa, N. Sakai, T. Kawada and M. Dokiya, *J. Solid State Chem.*, 1991, **94**, 106–120.

126 A. A. Taskin, A. N. Lavrov and Y. Ando, *Appl. Phys. Lett.*, 2005, **86**, 091910.

127 C. Bernuy-Lopez, L. Rioja-Monllor, T. Nakamura, S. Ricote, R. O'Hayre, K. Amezawa, M. A. Einarsrud and T. Grande, *Materials*, 2018, **11**, 196.

128 D. Parfitt, A. Chroneos, A. Tarancón and J. A. Kilner, *J. Mater. Chem.*, 2011, **21**, 2183–2186.

129 A. Arulraj, F. Goutenoire, M. Tabellout, O. Bohnke and P. Lacorre, *Chem. Mater.*, 2002, **14**, 2492–2498.

130 I. Animitsa, N. Tarasova and Y. Filinkova, *Solid State Ionics*, 2012, **207**, 29–37.

131 J. C. Ruiz-Morales, J. Canales-Vázquez, C. Savaniu, D. Marrero-López, W. Zhou and J. T. Irvine, *Nature*, 2006, **439**, 568–571.

132 J. H. Kim, D. Kim, S. Ahn, K. J. Kim, S. Jeon, D.-K. Lim, J. K. Kim, U. Kim, H.-N. Im, B. Koo, K. T. Lee and W. Jung, *Energy Environ. Sci.*, 2023, **16**, 3803–3814.

133 R. Ren, Z. Wang, C. Xu, W. Sun, J. Qiao, D. W. Rooney and K. Sun, *J. Mater. Chem. A*, 2019, **7**, 18365–18372.

134 J. Wang, B. Wang, G. Huangfu, H. Zhang and Y. Guo, *Acta Mater.*, 2024, 120520.

135 N. Ran, W. Qiu, E. Song, Y. Wang, X. Zhao, Z. Liu and J. Liu, *Chem. Mater.*, 2020, **32**, 1224–1234.

136 J. Bielecki, S. F. Parker, L. Mazzei, L. Börjesson and M. Karlsson, *J. Mater. Chem. A*, 2016, **4**, 1224–1232.

137 K. Saito, K. Umeda, K. Fujii, K. Mori and M. Yashima, *J. Mater. Chem. A*, 2024, **12**, 13310–13319.

138 M. T. Greiner, L. Chai, M. G. Helander, W. M. Tang and Z. H. Lu, *Adv. Funct. Mater.*, 2012, **22**, 4557–4568.

139 Z. Sherafat, M. H. Paydar, I. Antunes, N. Nasani, A. D. Brandão and D. P. Fagg, *Electrochim. Acta*, 2015, **165**, 443–449.

140 N. Sakai, *Solid State Ionics*, 2004, **175**, 387–391.

141 N. Sakai, K. Yamaji, T. Horita, Y. P. Xiong, H. Kishimoto and H. Yokokawa, *J. Electrochem. Soc.*, 2003, **150**, A689–A694.

142 R. R. Liu, S. H. Kim, S. Taniguchi, T. Oshima, Y. Shiratori, K. Ito and K. Sasaki, *J. Power Sources*, 2011, **196**, 7090–7096.

143 S. Ricote, G. Caboche, C. Estournès and N. Bonanos, *J. Nanomater.*, 2008, **2008**, 354258–354262.

144 D. Hashimoto, D. Han and T. Uda, *Solid State Ionics*, 2014, **262**, 687–690.

145 A. Grimaud, J. M. Bassat, F. Mauvy, M. Pollet, A. Wattiaux, M. Marrony and J. C. Grenier, *J. Mater. Chem. A*, 2014, **2**, 3594.

146 X. Xu, J. Zhao, M. Li, L. Zhuang, J. Zhang, S. Aruliah, F. Liang, H. Wang and Z. Zhu, *Composites, Part B*, 2019, **178**, 107491.

This journal is © The Royal Society of Chemistry 2025

Energy Environ. Sci., 2025, **18**, 4555–4595 | **4587**

147 W. Zhou, B. An, R. Ran and Z. Shao, *J. Electrochem. Soc.*, 2009, **156**, B884–B890.

148 J. Tallgren, O. Himanen, M. Bianco, J. Mikkola, O. Thomann, M. Rautanen, J. Kiviaho and J. Van herle, *Fuel Cells*, 2019, **19**, 570–577.

149 W. Preis, E. Bucher and W. Sitte, *Fuel Cells*, 2012, **12**, 543–549.

150 S. Zhao, W. Ma, W. Wang, Y. Huang, J. Wang, S. Wang, Z. Shu, B. He and L. Zhao, *Adv. Mater.*, 2024, **36**, 2405052.

151 X. Chen, N. Yu, Y. Song, T. Liu, H. Xu, D. Guan, Z. Li, W. H. Huang, Z. Shao, F. Ciucci and M. Ni, *Adv. Mater.*, 2024, **36**, 2403998.

152 A. Seong, J. Kim, D. Jeong, S. Sengodan, M. Liu, S. Choi and G. Kim, *Adv. Sci.*, 2021, **8**, 2004099.

153 T. H. Wan, M. Saccoccio, C. Chen and F. Ciucci, *Electrochim. Acta*, 2015, **184**, 483–499.

154 C. Mänken, D. Schäfer and R.-A. Eichel, *J. Electrochem. Soc.*, 2024, **171**, 114501.

155 J.-I. Jung, S. T. Misture and D. D. Edwards, *Solid State Ionics*, 2010, **181**, 1287–1293.

156 S. Wang, *Solid State Ionics*, 2003, **159**, 71–78.

157 J. Song, S. Zhu, D. Ning and H. J. Bouwmeester, *J. Mater. Chem. A*, 2021, **9**, 974–989.

158 Y. Chen, T. Hong, P. Wang, K. Brinkman, J. Tong and J. Cheng, *J. Power Sources*, 2019, **440**, 227122.

159 J. Gu, L. Jiang, S. A. Ismail, H. Guo and D. Han, *Adv. Mater. Interfaces*, 2023, **10**, 2201764.

160 D. Zou, Y. Yi, Y. Song, D. Guan, M. Xu, R. Ran, W. Wang, W. Zhou and Z. Shao, *J. Mater. Chem. A*, 2022, **10**, 5381–5390.

161 Y.-D. Kim, C. Meisel, I.-H. Kim, C. Herradón, P. Rand, J. Yang, N. P. Sullivan and R. O'Hayre, *J. Power Sources*, 2025, **625**, 235700.

162 Q. Wang, T. Luo, Y. Tong, M. Dai, X.-Y. Miao, S. Ricote, Z. Zhan and M. Chen, *Sep. Purif. Technol.*, 2022, **295**, 121301.

163 S. Guo, L. Jiang, Y. Li, P. Zhong, S. A. Ismail, T. Norby and D. Han, *Adv. Funct. Mater.*, 2024, **34**, 2304729.

164 U. Tariq, M. Z. Khan, O. Gohar, Z. U. Din Babar, F. Ali, R. A. Malik, I. A. Starostina, Samia, J. Rehman, I. Hussain, M. Saleem, A. Ghaffar, M. A. Marwat, K. Zheng, M. Motola and M. B. Hanif, *J. Power Sources*, 2024, **613**, 234910.

165 C. Zhou, J. Sunarso, Y. Song, J. Dai, J. Zhang, B. Gu, W. Zhou and Z. Shao, *J. Mater. Chem. A*, 2019, **7**, 13265–13274.

166 R. Ren, X. Yu, Z. Wang, C. Xu, T. Song, W. Sun, J. Qiao and K. Sun, *Appl. Catal., B*, 2022, **317**, 121759.

167 C. Zhou, X. Wang, D. Liu, M. Fei, J. Dai, D. Guan, Z. Hu, L. Zhang, Y. Wang, W. Wang, R. O'Hayre, S. P. Jiang, W. Zhou, M. Liu and Z. Shao, *Energy Environ. Mater.*, 2024, **7**, e12660.

168 S. Paul, S.-J. Choi and H. J. Kim, *Energy Fuels*, 2020, **34**, 10067–10077.

169 N. N. Krishnan, N. M. H. Duong, A. Konovalova, J. H. Jang, H. S. Park, H. J. Kim, A. Roznowska, A. Michalak and D. Henkensmeier, *J. Membr. Sci.*, 2020, **614**, 118494.

170 Y. Zhang, B. Chen, D. Guan, M. Xu, R. Ran, M. Ni, W. Zhou, R. O'Hayre and Z. Shao, *Nature*, 2021, **591**, 246–251.

171 Y. Song, J. Liu, Y. Wang, D. Guan, A. Seong, M. Liang, M. J. Robson, X. Xiong, Z. Zhang, G. Kim, Z. Shao and F. Ciucci, *Adv. Energy Mater.*, 2021, **11**, 2101899.

172 H. Ding, W. Wu, C. Jiang, Y. Ding, W. Bian, B. Hu, P. Singh, C. J. Orme, L. Wang and Y. Zhang, *Nat. Commun.*, 2020, **11**, 1907.

173 X. Wu, Y. Guo, Z. Sun, F. Xie, D. Guan, J. Dai, F. Yu, Z. Hu, Y.-C. Huang and C.-W. Pao, *Nat. Commun.*, 2021, **12**, 660.

174 D. Guan, G. Ryu, Z. Hu, J. Zhou, C.-L. Dong, Y.-C. Huang, K. Zhang, Y. Zhong, A. C. Komarek and M. Zhu, *Nat. Commun.*, 2020, **11**, 3376.

175 S. Agrestini, K. Chen, C.-Y. Kuo, L. Zhao, H.-J. Lin, C.-T. Chen, A. Rogalev, P. Ohresser, T.-S. Chan and S.-C. Weng, *Phys. Rev. B*, 2019, **100**, 014443.

176 K. Ye, K. Li, Y. Lu, Z. Guo, N. Ni, H. Liu, Y. Huang, H. Ji and P. Wang, *TrAC, Trends Anal. Chem.*, 2019, **116**, 102–108.

177 Y.-M. Kim, J. He, M. D. Biegalski, H. Ambaye, V. Lauter, H. M. Christen, S. T. Pantelides, S. J. Pennycook, S. V. Kalinin and A. Y. Borisevich, *Nat. Mater.*, 2012, **11**, 888–894.

178 Z. F. Zhao, Z. X. Xue, Q. Q. Xiong, Y. Q. Zhang, X. S. Hu, H. Z. Chi, H. Y. Qin, Y. J. Yuan and H. L. Ni, *Sustainable Mater. Technol.*, 2021, **30**, e00357.

179 Z. Liu, Y. Lin, H. Nie, D. Liu, Y. Li, X. Zhao, T. Li, G. Yang, Y. Sun, Y. Zhu, W. Wang, R. Ran, W. Zhou and Z. Shao, *Adv. Funct. Mater.*, 2024, **34**, 2311140.

180 L. A. Lyon, C. D. Keating, A. P. Fox, B. E. Baker, L. He, S. R. Nicewarner, S. P. Mulvaney and M. J. Natan, *Anal. Chem.*, 1998, **70**, 341–362.

181 X. Li, K. Blinn, D. Chen and M. Liu, *Electrochem. Energy Rep.*, 2018, **1**, 433–459.

182 Y. Song, J. Min, Y. Guo, R. Li, G. Zou, M. Li, Y. Zang, W. Feng, X. Yao, T. Liu, X. Zhang, J. Yu, Q. Liu, P. Zhang, R. Yu, X. Cao, J. Zhu, K. Dong, G. Wang and X. Bao, *Angew. Chem., Int. Ed.*, 2024, **63**, e202313361.

183 C. Lu, R. Ren, Z. Zhu, G. Pan, G. Wang, C. Xu, J. Qiao, W. Sun, Q. Huang, H. Liang, Z. Wang and K. Sun, *Chem. Eng. J.*, 2023, **472**, 144878.

184 J. W. Smith and R. J. Saykally, *Chem. Rev.*, 2017, **117**, 13909–13934.

185 F. M. de Groot, M. W. Haverkort, H. Elnaggar, A. Juhin, K.-J. Zhou and P. Glatzel, *Nat. Rev. Methods Primers*, 2024, **4**, 45.

186 H. Over, Y. D. Kim, A. Seitsonen, S. Wendt, E. Lundgren, M. Schmid, P. Varga, A. Morgante and G. Ertl, *Science*, 2000, **287**, 1474–1476.

187 F. He, Y. Zhou, T. Hu, Y. Xu, M. Hou, F. Zhu, D. Liu, H. Zhang, K. Xu, M. Liu and Y. Chen, *Adv. Mater.*, 2023, **35**, 2209469.

188 Z. Cheng, J.-H. Wang, Y. Choi, L. Yang, M.-C. Lin and M. Liu, *Energy Environ. Sci.*, 2011, **4**, 4380–4409.

189 L. Pauling, *J. Chem. Educ.*, 1992, **69**, 519–521.

190 https://www.metal.com/price.

191 https://en.institut-seltene-erden.de/current-prices-of-strategic-metals/.

4588 | *Energy Environ. Sci.*, 2025, **18**, 4555–4595

This journal is © The Royal Society of Chemistry 2025

192 R. Shannon, *Acta Crystallogr.*, 1976, **32**, 751–767.

193 Y. Niu, Y. Zhou, W. Zhang, Y. Zhang, C. Evans, Z. Luo, N. Kane, Y. Ding, Y. Chen, X. Guo, W. Lv and M. Liu, *Adv. Energy Mater.*, 2022, **12**, 2103783.

194 Y. Zhou, E. Liu, Y. Chen, Y. Liu, L. Zhang, W. Zhang, Z. Luo, N. Kane, B. Zhao, L. Soule, Y. Niu, Y. Ding, H. Ding, D. Ding and M. Liu, *ACS Energy Lett.*, 2021, **6**, 1511–1520.

195 Y. Zhou, W. Zhang, N. Kane, Z. Luo, K. Pei, K. Sasaki, Y. Choi, Y. Chen, D. Ding and M. Liu, *Adv. Funct. Mater.*, 2021, **31**, 2105386.

196 H. Zheng, X. Zhou, X. Wang, Z. Zhao, Y. Wang, C. Xie, Y. Wang, H. Li and X. Ding, *J. Power Sources*, 2024, **597**, 234164.

197 K. Shi, Y. Yin, Z. Tang, S. Yu and Q. Zhang, *Ceram. Int.*, 2022, **48**, 13024–13031.

198 S. Peng, S. Lei, S. Wen, G. Weng, K. Ouyang, Z. Yin, J. Xue and H. Wang, *Int. J. Hydrogen Energy*, 2023, **48**, 22209–22219.

199 D. Kim, I. Jeong, S. Ahn, S. Oh, H. N. Im, H. Bae, S. J. Song, C. W. Lee, W. Jung and K. T. Lee, *Adv. Energy Mater.*, 2024, **14**, 2304059.

200 X. Wang, W. Li, C. Zhou, M. Xu, Z. Hu, C.-W. Pao, W. Zhou and Z. Shao, *ACS Appl. Mater. Interfaces*, 2023, **15**, 1339–1347.

201 M. Fu, W. Hu, H. Tong, X. Ling, L. Tan, F. Chen and Z. Tao, *J. Adv. Ceram.*, 2024, **13**, 63–72.

202 Y. Xu, X. Xu and L. Bi, *J. Adv. Ceram.*, 2022, **11**, 794–804.

203 Z. Liu, Z. Tang, Y. Song, G. Yang, W. Qian, M. Yang, Y. Zhu, R. Ran, W. Wang, W. Zhou and Z. Shao, *Nano-Micro Lett.*, 2022, **14**, 217.

204 F. He, Y. Zhou, T. Hu, Y. Xu, M. Hou, F. Zhu, D. Liu, H. Zhang, K. Xu, M. Liu and Y. Chen, *Adv. Mater.*, 2023, **35**, 2209469.

205 J. Sun, R. Ren, H. Yue, W. Cui, G. Wang, C. Xu, J. Qiao, W. Sun, K. Sun and Z. Wang, *Chin. Chem. Lett.*, 2023, **34**, 107776.

206 C. Yang, J. Li, S. Hu, J. Pu and B. Chi, *Ceram. Int.*, 2023, **49**, 38331–38338.

207 Y. Song, Y. Chen, W. Wang, C. Zhou, Y. Zhong, G. Yang, W. Zhou, M. Liu and Z. Shao, *Joule*, 2019, **3**, 2842–2853.

208 F. He, S. Liu, T. Wu, M. Yang, W. Li, G. Yang, F. Zhu, H. Zhang, K. Pei, Y. Chen, W. Zhou and Z. Shao, *Adv. Funct. Mater.*, 2022, **32**, 2206756.

209 F. He, M. Hou, D. Liu, Y. Ding, K. Sasaki, Y. Choi, S. Guo, D. Han, Y. Liu, M. Liu and Y. Chen, *Energy Environ. Sci.*, 2024, **17**, 3898–3907.

210 J. Seo, H.-W. Kim, J. H. Yu and H. J. Park, *J. Korean Ceram. Soc.*, 2022, **59**, 217–223.

211 X. Yang, Z. Wang, G. Li, Y. Zhou, C. Sun and L. Bi, *Ceram. Int.*, 2024, **50**, 40375–40383.

212 Z. Liu, D. Cheng, Y. Zhu, M. Liang, M. Yang, G. Yang, R. Ran, W. Wang, W. Zhou and Z. Shao, *Chem. Eng. J.*, 2022, **450**, 137787.

213 X. Chen, N. Yu, I. T. Bello, D. Guan, Z. Li, T. Liu, T. Liu, Z. Shao and M. Ni, *Energy Storage Mater.*, 2023, **63**, 103056.

214 Z. Liu, Y. Bai, H. Sun, D. Guan, W. Li, W.-H. Huang, C.-W. Pao, Z. Hu, G. Yang, Y. Zhu, R. Ran, W. Zhou and Z. Shao, *Nat. Commun.*, 2024, **15**, 472.

215 M. Liang, Y. Zhu, Y. Song, D. Guan, Z. Luo, G. Yang, S. P. Jiang, W. Zhou, R. Ran and Z. Shao, *Adv. Mater.*, 2022, **34**, 2106379.

216 J. H. Kim, J. Hong, D.-K. Lim, S. Ahn, J. Kim, J. K. Kim, D. Oh, S. Jeon, S.-J. Song and W. Jung, *Energy Environ. Sci.*, 2022, **15**, 1097–1105.

217 K. Park, M. Saqib, H. Lee, D. Shin, M. Jo, K. M. Park, M. Hamayun, S. H. Kim, S. Kim, K.-S. Lee, R. O'Hayre, M. Choi, S.-J. Song and J.-Y. Park, *Energy Environ. Sci.*, 2024, **17**, 1175–1188.

218 Y. Wang, Z. Wang, K. Yang, J. Liu, Y. Song, J. Li, Z. Hu, M. J. Robson, Z. Zhang, Y. Tian, S. Xu, Y. Lu, H. M. Law, F. Liu, Q. Chen, Z. Yang and F. Ciucci, *Adv. Funct. Mater.*, 2024, **34**, 2404846.

219 T. Zhou, H. Huang, Y. Meng, J. Conrad, M. Zou, Z. Zhao, K. S. Brinkman and J. Tong, *ACS Energy Lett.*, 2024, **9**, 4557–4563.

220 Z. Yu, L. Ge, Q. Ni, Y. Zheng, H. Chen, X. Zhou, Y. Mi, B. Shi, X. Yu, B. Wu, L. Bi and Y. Zhu, *Adv. Funct. Mater.*, 2024, **34**, 2309698.

221 X. Lu, Z. Yang, J. Zhang, X. Zhao, J. Chen, W. Liu, Y. Zhao and Y. Li, *J. Power Sources*, 2024, **599**, 234233.

222 H. Tong, M. Fu, Y. Yang, F. Chen and Z. Tao, *Adv. Funct. Mater.*, 2022, **32**, 2209695.

223 Q. Ye, H. Ye, Z. Ma, H. Lin, B. Zhao, G. Yang, F. Dong, M. Ni, Z. Lin and S. Zhang, *Small*, 2024, **20**, 2307900.

224 Z. Wang, Y. Wang, Y. Xiao, Y. Zhang, X. Wang, F. Wang and T. He, *Small*, 2024, **20**, 2312148.

225 S. Zhao, W. Ma, B. He, Y. Ling, Y. Huang, F. Hu, Z. Shu and L. Zhao, *Adv. Mater.*, 2025, e2501387, DOI: **10.1002/adma.202501387**.

226 Y. Xu, K. Xu, F. Zhu, F. He, H. Zhang, C. Fang, Y. Liu, Y. Zhou, Y. Choi and Y. Chen, *ACS Energy Lett.*, 2023, **8**, 4145–4155.

227 Y. Xu, Y. Huang, Y. Guo, F. Hu, J. Xu, W. Zhou, Z. Yang, J. Sun, B. He and L. Zhao, *Sep. Purif. Technol.*, 2022, **290**, 120844.

228 Z. Du, K. Xu, F. Zhu, Y. Xu, F. He, H. Gao, W. Gong, Y. Choi and Y. Chen, *Adv. Funct. Mater.*, 2024, **34**, 2409188.

229 K. Xu, H. Zhang, Y. Xu, D. Liu, F. Zhu, F. He, Y. Liu, H. Wang and Y. Chen, *Adv. Powder Mater.*, 2024, **3**, 100187.

230 K. Xu, H. Zhang, Y. Xu, F. He, Y. Zhou, Y. Pan, J. Ma, B. Zhao, W. Yuan, Y. Chen and M. Liu, *Adv. Funct. Mater.*, 2022, **32**, 2110998.

231 X. Zhang, R. Song, D. Huan, K. Zhu, X. Li, H. Han, C. Xia, R. Peng and Y. Lu, *Small*, 2022, **18**, 2205190.

232 X. Li, Z. Jin, C. Wang, R. Peng, Y. Zha, J. Cao, Y. Ji and Z. Shao, *Adv. Energy Mater.*, 2024, **14**, 2400319.

233 K. Pei, S. Luo, F. He, J. Arbiol, Y. Xu, F. Zhu, Y. Wang and Y. Chen, *Appl. Catal., B*, 2023, **330**, 122601.

234 H. Zhang, K. Xu, F. He, Y. Zhou, K. Sasaki, B. Zhao, Y. Choi, M. Liu and Y. Chen, *Adv. Energy Mater.*, 2022, **12**, 2200761.

235 H. Gao, F. He, F. Zhu, J. Xia, Z. Du, Y. Huang, L. Zhu and Y. Chen, *Adv. Funct. Mater.*, 2024, **34**, 2401747.

236 M. Choi, D. Kim, T. K. Lee, J. Lee, H. S. Yoo and W. Lee, *Adv. Energy Mater.*, 2025, **15**, 2400124.

237 X. Hu, Y. Zhou, Z. Luo, H. Li, N. Shi, Z. Liu, W. Zhang, W. Wang, Y. Ding and M. Liu, *Energy Environ. Sci.*, 2024, **17**, 9335.

This journal is © The Royal Society of Chemistry 2025

Energy Environ. Sci., 2025, **18**, 4555–4595 | **4589**

238 B. S. Teketel, B. A. Beshiwork, X. Luo, D. Tian, S. Zhu, H. G. Desta, Q. Yang, Y. Chen and B. Lin, *Ceram. Int.*, 2022, **48**, 37232–37241.

239 A. P. Tarutin, Y. G. Lyagaeva, A. I. Vylkov, M. Y. Gorshkov, G. K. Vdovin and D. A. Medvedev, *J. Mater. Sci. Technol.*, 2021, **93**, 157–168.

240 K. Zhu, L. Zhang, N. Shi, B. Qiu, X. Hu, D. Huan, C. Xia, R. Peng and Y. Lu, *ACS Nano*, 2024, **18**, 5141–5151.

241 W. Bian, W. Wu, B. Wang, W. Tang, M. Zhou, C. Jin, H. Ding, W. Fan, Y. Dong, J. Li and D. Ding, *Nature*, 2022, **604**, 479–485.

242 P. Yao, J. Zhang, Q. Qiu, Y. Zhao, F. Yu and Y. Li, *Adv. Energy Mater.*, 2024, 2403335, DOI: 10.1002/aenm.202403335.

243 J. Hwang, R. R. Rao, L. Giordano, Y. Katayama, Y. Yu and Y. Shao-Horn, *Science*, 2017, **358**, 751–756.

244 M. Medarde, C. Dallera, M. Grioni, J. Voigt, A. Podlesnyak, E. Pomjakushina, K. Conder, T. Neisius, O. Tjernberg and S. N. Barilo, *Phys. Rev. B: Condens. Matter Mater. Phys.*, 2006, **73**, 054424.

245 C. Frontera, J. L. García-Muñoz, A. E. Carrillo, C. Ritter, D. Martín y Marero and A. Caneiro, *Phys. Rev. B: Condens. Matter Mater. Phys.*, 2004, **70**, 184428.

246 E. Marelli, J. Lyu, M. Morin, M. Lemenager, T. Shang, N. S. Yuzbasi, D. Aegerter, J. Huang, N. D. Daffe, A. H. Clark, D. Sheptyakov, T. Graule, M. Nachtegaal, E. Pomjakushina, T. J. Schmidt, M. Krack, E. Fabbri and M. Medarde, *EES Catal.*, 2024, **2**, 335–350.

247 A. J. Barón-González, C. Frontera, J. L. García-Muñoz, J. Blasco and C. Ritter, *Phys. Rev. B: Condens. Matter Mater. Phys.*, 2010, **81**, 054427.

248 Y. Song, Y. Yi, R. Ran, W. Zhou and W. Wang, *Small*, 2024, e2406627, DOI: 10.1002/smll.202406627.

249 V. Cascos, R. Martínez-Coronado and J. A. Alonso, *Int. J. Hydrogen Energy*, 2014, **39**, 14349–14354.

250 I. Jeong, S. J. Jeong, B.-H. Yun, J.-W. Lee, C.-W. Lee, W. Jung and K. T. Lee, *NPG Asia Mater.*, 2022, **14**, 53.

251 M. Li, W. Zhou and Z. Zhu, *ChemElectroChem*, 2015, **2**, 1331–1338.

252 Z. Xu, J. Yu and W. Wang, *Membranes*, 2022, **12**, 831.

253 K. Pei, Y. Zhou, K. Xu, Z. He, Y. Chen, W. Zhang, S. Yoo, B. Zhao, W. Yuan, M. Liu and Y. Chen, *Nano Energy*, 2020, **72**, 104704.

254 T. Hibino, A. Hashimoto, M. Suzuki and M. Sano, *J. Electrochem. Soc.*, 2002, **149**, A1503.

255 S. Svarcova, *Solid State Ionics*, 2008, **178**, 1787–1791.

256 W. Zhou, J. Sunarso, J. Motuzas, F. Liang, Z. Chen, L. Ge, S. Liu, A. Julbe and Z. Zhu, *Chem. Mater.*, 2011, **23**, 1618–1624.

257 T. Ishihara, S. Fukui, H. Nishiguchi and Y. Takita, *J. Electrochem. Soc.*, 2002, **149**, A823.

258 T. Ishihara, *Proc. Vol.*, 2001, **2001-16**, 439–448.

259 T. Ishihara, S. Fukui, H. Nishiguchi and Y. Takita, *Solid State Ionics*, 2002, **152–153**, 609–613.

260 Y. Niu, Y. Kong, C. Sun, X. Song, N. Zhang and K. Sun, *ChemistrySelect*, 2019, **4**, 10851–10855.

261 Z. Zhao, H. Qi, S. Tang, C. Zhang, X. Wang, M. Cheng and Z. Shao, *Int. J. Hydrogen Energy*, 2021, **46**, 36012–36022.

262 B. Liu, J. Sunarso, Y. Zhang, G. Yang, W. Zhou and Z. Shao, *ChemElectroChem*, 2018, **5**, 785–792.

263 X. Wang, T. Zhang, H. Qi and B. Tu, *Mater. Lett.*, 2024, **355**, 135513.

264 X. Yang, X. Han, T. He and Y. Du, *ECS Trans.*, 2017, **78**, 543.

265 K. Xie, J. Zhou and G. Meng, *J. Alloys Compd.*, 2010, **506**, L8–L11.

266 M. Shang, J. Tong and R. O'Hayre, *RSC Adv.*, 2013, **3**, 15769.

267 X. Mao, Z. Li, M. Li, X. Xu, C. Yan, Z. Zhu and A. Du, *J. Am. Chem. Soc.*, 2021, **143**, 9507–9514.

268 R. Guo and T. He, *ACS Mater. Lett.*, 2022, **4**, 1646–1652.

269 E. Y. Y. Pikalova, E. G. G. Kalinina, N. S. S. Pikalova and E. A. A. Filonova, *Materials*, 2022, **15**, 8783.

270 S. Oh, D. Kim, H. J. Ryu and K. T. Lee, *Adv. Funct. Mater.*, 2023, **34**, 2311426.

271 Q. Wang, X. Liu, D. He and D. Wang, *Mater. Today*, 2023, **70**, 218–236.

272 J. Cheng, A. Navrotsky, X.-D. Zhou and H. U. Anderson, *Chem. Mater.*, 2005, **17**, 2197.

273 R. Witte, A. Sarkar, R. Kruk, B. Eggert, R. A. Brand, H. Wende and H. Hahn, *Phys. Rev. Mater.*, 2019, **3**, 034406.

274 S.-W. Cheong and M. Mostovoy, *Nat. Mater.*, 2007, **6**, 13–20.

275 J. R. Mawdsley and T. R. Krause, *Appl. Catal., A*, 2008, **334**, 311–320.

276 J. Dąbrowa, A. Olszewska, A. Falkenstein, C. Schwab, M. Szymczak, M. Zajusz, M. Moździerz, A. Mikuła, K. Zielińska, K. Berent, T. Czeppe, M. Martin and K. Świerczek, *J. Mater. Chem. A*, 2020, **8**, 24455–24468.

277 Y. Yang, H. Bao, H. Ni, X. Ou, S. Wang, B. Lin, P. Feng and Y. Ling, *J. Power Sources*, 2021, **482**, 228959.

278 Y. Shi, N. Ni, Q. Ding and X. Zhao, *J. Mater. Chem. A*, 2022, **10**, 2256–2270.

279 W. Zhou, R. Ran and Z. Shao, *J. Power Sources*, 2009, **192**, 231–246.

280 M. Marrony, M. Ancelin, G. Lefevre and J. Dailly, *Solid State Ionics*, 2015, **275**, 97–100.

281 Z. Shao and S. M. Haile, *Nature*, 2004, **431**, 170–173.

282 Z. Shao, S. M. Haile, J. Ahn, P. D. Ronney, Z. Zhan and S. A. Barnett, *Nature*, 2005, **435**, 795–798.

283 B. Lin, H. Ding, Y. Dong, S. Wang, X. Zhang, D. Fang and G. Meng, *J. Power Sources*, 2009, **186**, 58–61.

284 G. Taillades, P. Pers, P. Batocchi and M. Taillades, *ECS Trans.*, 2013, **57**, 1289.

285 J. Dailly, M. Ancelin and M. Marrony, *Solid State Ionics*, 2017, **306**, 69–75.

286 T. Yang, A. Shaula, D. Pukazhselvan, D. Ramasamy, J. Deng, E. L. da Silva, R. Duarte and J. A. Saraiva, *Appl. Surf. Sci.*, 2017, **424**, 82–86.

287 G. Taillades, P. Pers, V. Mao and M. Taillades, *Int. J. Hydrogen Energy*, 2016, **41**, 12330–12336.

288 J. Kim, A. Jun, O. Gwon, S. Yoo, M. Liu, J. Shin, T.-H. Lim and G. Kim, *Nano Energy*, 2018, **44**, 121–126.

289 L. Lei, J. Zhang, Z. Yuan, J. Liu, M. Ni and F. Chen, *Adv. Funct. Mater.*, 2019, **29**, 1903805.

290 M. Choi, S. J. Kim and W. Lee, *Ceram. Int.*, 2021, **47**, 7790–7797.

291 N. Bausá, C. Solís, R. Strandbakke and J. M. Serra, *Solid State Ionics*, 2017, **306**, 62–68.

292 Y. Xie, N. Shi, X. Hu, K. Zhu, R. Peng, C. Xia and M. Chen, *J. Electrochem. Soc.*, 2023, **170**, 024513.

293 Z. Zhang, Y. Zhu, Y. Zhong, W. Zhou and Z. Shao, *Adv. Energy Mater.*, 2017, **7**, 1700242.

294 J. Zhu, G. Liu, Z. Liu, Z. Chu, W. Jin and N. Xu, *Adv. Mater.*, 2016, **28**, 3511–3515.

295 Y. Li, Y. Li, Y. Wan, Y. Xie, J. Zhu, H. Pan, X. Zheng and C. Xia, *Adv. Energy Mater.*, 2018, **9**, 1803156.

296 C. Yang, Y. Tian, C. Yang, G. Kim, J. Pu and B. Chi, *Adv. Sci.*, 2023, **10**, 2304224.

297 Y. Zhang, Z. Zhu, Y. Gu, H. Chen, Y. Zheng and L. Ge, *Ceram. Int.*, 2020, **46**, 22787–22796.

298 C. Yang, Y. Tian, J. Pu and B. Chi, *ACS Sustainable Chem. Eng.*, 2022, **10**, 1047–1058.

299 Y. Wang, H. Wang, T. Liu, F. Chen and C. Xia, *Electrochem. Commun.*, 2013, **28**, 87–90.

300 Y. Xie, N. Shi, D. Huan, W. Tan, J. Zhu, X. Zheng, H. Pan, R. Peng and C. Xia, *ChemSusChem*, 2018, **11**, 3423–3430.

301 J. F. Shin, W. Xu, M. Zanella, K. Dawson, S. N. Savvin, J. B. Claridge and M. J. Rosseinsky, *Nat. Energy*, 2017, **2**, 1–7.

302 A. Demont, R. Sayers, M. A. Tsiamtsouri, S. Romani, P. A. Chater, H. Niu, C. Marti-Gastaldo, Z. Xu, Z. Deng, Y. Breard, M. F. Thomas, J. B. Claridge and M. J. Rosseinsky, *J. Am. Chem. Soc.*, 2013, **135**, 10114–10123.

303 Z. He, J. Nie, K. Liu, K. S. Ganesh, M. Akbar, C. Xia, X. Wang, W. Dong, J. Huang and B. Wang, *Int. J. Hydrogen Energy*, 2021, **46**, 9799–9808.

304 H. Lee, H. Jung, C. Kim, S. Kim, I. Jang, H. Yoon, U. Paik and T. Song, *ACS Appl. Energy Mater.*, 2021, **4**, 11564–11573.

305 L. Li, Y. Fan, C. Zhou, J. Zhou, M. Wang, L. Zhou, L. Zhang and J.-Q. Wang, *J. Phys. Chem. C*, 2023, **127**, 19107–19114.

306 M. Liang, Y. Song, D. Liu, L. Xu, G. Yang, W. Wang, W. Zhou, R. Ran, M. Xu and Z. Shao, *Appl. Catal., B*, 2022, **318**, 121868.

307 R. Song, X. Zhang, D. Huan, X. Li, N. Shi, C. Xia, R. Peng and Y. Lu, *Int. J. Hydrogen Energy*, 2023, **48**, 32943–32954.

308 J. H. Duffy, H. W. Abernathy and K. S. Brinkman, *J. Mater. Chem. A*, 2023, **11**, 8929–8938.

309 N. Wang, S. Hinokuma, T. Ina, C. Zhu, H. Habazaki and Y. Aoki, *J. Mater. Chem. A*, 2020, **8**, 11043–11055.

310 T. Zhu, H. E. Troiani, L. V. Mogni, M. Han and S. A. Barnett, *Joule*, 2018, **2**, 478–496.

311 L. Rioja-Monllor, C. Bernuy-Lopez, M.-L. Fontaine, T. Grande and M.-A. Einarsrud, *J. Mater. Chem. A*, 2019, **7**, 8609–8619.

312 S. Liu, K. T. Chuang and J.-L. Luo, *ACS Catal.*, 2015, **6**, 760–768.

313 J. H. Kim, J. K. Kim, H. G. Seo, D. K. Lim, S. J. Jeong, J. Seo, J. Kim and W. Jung, *Adv. Funct. Mater.*, 2020, **30**, 2001326.

314 W. Zhang, H. Wang, X. Chen, X. Liu and J. Meng, *Chem. Eng. J.*, 2022, **446**, 136934.

315 X. Zhang, W. Zhang, L. Zhang, J. Meng, F. Meng, X. Liu and J. Meng, *Electrochim. Acta*, 2017, **258**, 1096–1105.

316 H. Qi, F. Xia, T. Yang, W. Li, W. Li, L. Ma, G. Collins, W. Shi, H. Tian, S. Hu, T. Thomas, E. M. Sabolsky, J. Zondlo,

R. Hart, H. Finklea, G. A. Hackett and X. Liu, *J. Electrochem. Soc.*, 2020, **167**, 024510.

317 L. Adijanto, V. B. Padmanabhan, R. J. Gorte and J. M. Vohs, *J. Electrochem. Soc.*, 2012, **159**, F751–F756.

318 J. H. Kim, J. K. Kim, J. Liu, A. Curcio, J. S. Jang, I. D. Kim, F. Ciucci and W. Jung, *ACS Nano*, 2021, **15**, 81–110.

319 J. Wang, D. Kalaev, J. Yang, I. Waluyo, A. Hunt, J. T. Sadowski, H. L. Tuller and B. Yildiz, *J. Am. Chem. Soc.*, 2023, **145**, 1714–1727.

320 Y. S. Chung, T. Kim, T. H. Shin, H. Yoon, S. Park, N. M. Sammes, W. B. Kim and J. S. Chung, *J. Mater. Chem. A*, 2017, **5**, 6437–6446.

321 S. He, *Prog. Nat. Sci.: Mater. Int.*, 2021, **31**, 341–372.

322 C.-C. Chueh, A. Bertei and C. Nicolella, *J. Power Sources*, 2019, **437**, 226888.

323 K. Chen, *Int. J. Hydrogen Energy*, 2011, **36**, 10541–10549.

324 Y. Wang, W. Li, L. Ma, W. Li and X. Liu, *J. Mater. Sci. Technol.*, 2020, **55**, 35–55.

325 P. Lin, X. Xu, S. Yu, Y. Yin, M. Andersson and L. Bi, *J. Power Sources*, 2022, **551**, 232073.

326 Y. Wan, Y. Xing, Y. Li, D. Huan and C. Xia, *J. Power Sources*, 2018, **402**, 363–372.

327 P. L. Knöchel, P. J. Keenan, C. Loho, C. Reitz, R. Witte, K. S. Knight, A. J. Wright, H. Hahn, P. R. Slater and O. Clemens, *J. Mater. Chem. A*, 2016, **4**, 3415–3430.

328 Y. Xia, X. Xu, Y. Teng, H. Lv, Z. Jin, D. Wang, R. Peng and W. Liu, *Ceram. Int.*, 2020, **46**, 25453–25459.

329 X. Xu, H. Wang, J. Ma, W. Liu, X. Wang, M. Fronzi and L. Bi, *J. Mater. Chem. A*, 2019, **7**, 18792–18798.

330 T. Hu, F. Zhu, J. Xia, F. He, Z. Du, Y. Zhou, Y. Liu, H. Wang and Y. Chen, *Adv. Funct. Mater.*, 2023, **33**, 2305567.

331 H. Wang, C. Tablet, A. Feldhoff and J. Caro, *Adv. Mater.*, 2005, **17**, 1785–1788.

332 Z. Wei, Z. Li, Z. Wang, Y. Zhao, J. Wang and J. Chai, *Int. J. Hydrogen Energy*, 2022, **47**, 13490–13501.

333 J. Ma, F. Zhu, Y. Pan, H. Zhang, K. Xu, Y. Wang and Y. Chen, *Sep. Purif. Technol.*, 2022, **288**, 120657.

334 J. Jing, Z. Lei, Z. Wu, Z. Wang, H. Yu, Z. Yang and S. Peng, *J. Eur. Ceram. Soc.*, 2022, **42**, 6566–6573.

335 T. Hu, Y. Xu, K. Xu, F. Zhu and Y. Chen, *SusMat*, 2023, **3**, 91–101.

336 Y. Lu, N. Mushtaq, M. A. K. Y. Shah, M. S. Irshad, S. Rauf, M. Yousaf and B. Zhu, *Ceram. Int.*, 2023, **49**, 2811–2820.

337 Y. Xiao, D. Bao, Z. Wang, Y. Wang and T. He, *Int. J. Hydrogen Energy*, 2024, **57**, 880–888.

338 J. Jing, Z. Lei, Z. Zheng, H. Wang, Z. Yang and S. Peng, *Int. J. Hydrogen Energy*, 2022, **47**, 35449–35457.

339 J. Wang, Z. Li, H. Zang, Y. Sun, Y. Zhao, Z. Wang, Z. Zhu, Z. Wei and Q. Zheng, *Int. J. Hydrogen Energy*, 2022, **47**, 9395–9407.

340 C. Zhang and H. Zhao, *J. Mater. Chem.*, 2012, **22**, 18387–18394.

341 J. Jing, Z. Lei, Z. Zheng, H. Wang, P. Zhang, Z. Wang, H. Xu and Z. Yang, *Int. J. Hydrogen Energy*, 2023, **48**, 9037–9045.

342 L. Zhang, S. Yang and S. Zhang, *J. Power Sources*, 2019, **440**, 227125.

This journal is © The Royal Society of Chemistry 2025

Energy Environ. Sci., 2025, **18**, 4555–4595 | **4591**

343 J. Liu, Z. Jin, L. Miao, J. Ding, H. Tang, Z. Gong, R. Peng and W. Liu, *Int. J. Hydrogen Energy*, 2019, **44**, 11079–11087.

344 C. Yang, J. Li, A. Hu, J. Pu and B. Chi, *Trans. Tianjin Univ.*, 2023, **29**, 444–452.

345 Z. Wei, Z. Li, Z. Wang, Y. Zhao, J. Wang and J. Chai, *Int. J. Hydrogen Energy*, 2022, **47**, 13490–13501.

346 J. Ma, Y. Xu, F. Zhu and Y. Chen, *Sustainable Mater. Technol.*, 2024, **40**, e00888.

347 D. Zou, Y. Yi, Y. Song, D. Guan, M. Xu, R. Ran, W. Wang, W. Zhou and Z. Shao, *J. Mater. Chem. A*, 2022, **10**, 5381–5390.

348 J.-H. Kim and A. Manthiram, *J. Mater. Chem. A*, 2015, **3**, 24195–24210.

349 S. Yoo, J. Y. Shin and G. Kim, *J. Mater. Chem.*, 2011, **21**, 439–443.

350 J. Jiang, Y. Zhang, X. Yang, Y. Shen and T. He, *ACS Appl. Energy Mater.*, 2020, **4**, 134–145.

351 G.-M. Park, K. Park, M. Jo, M. Asif, Y. Bae, S.-H. Kim, A. K. Azad, S.-J. Song and J.-Y. Park, *J. Alloys Compd.*, 2023, **968**, 171987.

352 E. Vollestad, R. Strandbakke, M. Tarach, D. Catalan-Martinez, M. L. Fontaine, D. Beeaff, D. R. Clark, J. M. Serra and T. Norby, *Nat. Mater.*, 2019, **18**, 752–759.

353 H. Zheng, F. Han, N. Sata and R. Costa, *J. Energy Chem.*, 2023, **86**, 437–446.

354 Y. Gu, Y. Zhang, Y. Zheng, H. Chen, L. Ge and L. Guo, *Appl. Catal., B*, 2019, **257**, 117868.

355 C. Ferchaud, J.-C. Grenier, Y. Zhang-Steenwinkel, M. M. A. van Tuel, F. P. F. van Berkel and J.-M. Bassat, *J. Power Sources*, 2011, **196**, 1872–1879.

356 L. Jiang, F. Li, T. Wei, R. Zeng and Y. Huang, *Electrochim. Acta*, 2014, **133**, 364–372.

357 L. Zhao, J. Shen, B. He, F. Chen and C. Xia, *Int. J. Hydrogen Energy*, 2011, **36**, 3658–3665.

358 H. Ding, Y. Xie and X. Xue, *J. Power Sources*, 2011, **196**, 2602–2607.

359 L. Zhu, R. O'Hayre and N. P. Sullivan, *Int. J. Hydrogen Energy*, 2021, **46**, 27784–27792.

360 C. Zhu, X. Liu, C. Yi, D. Yan and W. Su, *J. Power Sources*, 2008, **185**, 193–196.

361 J. Li, L. Jia, B. Chi, J. Pu, J. Li and S. Wang, *Int. J. Hydrogen Energy*, 2019, **44**, 31525–31530.

362 J. L. García-Muñoz, C. Frontera, A. Llobet, A. E. Carrillo, A. Caneiro, M. A. G. Aranda, M. Respaud, C. Ritter and E. Dooryee, *J. Magn. Magn. Mater.*, 2004, **272–276**, 1762–1763.

363 K. Zhang, L. Ge, R. Ran, Z. Shao and S. Liu, *Acta Mater.*, 2008, **56**, 4876–4889.

364 G. Kim, S. Wang, A. J. Jacobson, Z. Yuan, W. Donner, C. L. Chen, L. Reimus, P. Brodersen and C. A. Mims, *Appl. Phys. Lett.*, 2006, **88**, 024103.

365 H. Gu, G. Yang, Y. Hu, M. Liang, S. Chen, R. Ran, M. Xu, W. Wang, W. Zhou and Z. Shao, *Int. J. Hydrogen Energy*, 2020, **45**, 25996–26004.

366 G. Kim, S. Wang, A. J. Jacobson, L. Reimus, P. Brodersen and C. A. Mims, *J. Mater. Chem.*, 2007, **17**, 2500.

367 P. Winiarz, E. A. Sroczyk, A. Brzoza-Kos, P. Czaja, K. Kapusta and K. Świerczek, *Acta Mater.*, 2024, **277**, 120186.

368 Y. Xie, N. Shi, S. Ricote and M. Chen, *Chem. Eng. J.*, 2024, **492**, 151939.

369 U. Anjum, M. Agarwal, T. S. Khan and M. A. Haider, *ECS Trans.*, 2017, **78**, 499–506.

370 Z. Du, F. He, H. Gao, Y. Xu, F. Zhu, K. Xu, J. Xia, H. Zhang, Y. Huang, Y. Liu and Y. Chen, *Energy Storage Mater.*, 2024, **68**, 103345.

371 U. Anjum, S. Vashishtha, N. Sinha and M. A. Haider, *Solid State Ionics*, 2015, **280**, 24–29.

372 S. Zhai, H. Xie, P. Cui, D. Guan, J. Wang, S. Zhao, B. Chen, Y. Song, Z. Shao and M. Ni, *Nat. Energy*, 2022, **7**, 866–875.

373 J. T. S. Irvine, D. Neagu, M. C. Verbraeken, C. Chatzi-christodoulou, C. Graves and M. B. Mogensen, *Nat. Energy*, 2016, **1**, 1–13.

374 D. Kim, A. Hunt, I. Waluyo and B. Yildiz, *J. Mater. Chem. A*, 2023, **11**, 7299–7313.

375 S. Koohfar, M. Ghasemi, T. Hafen, G. Dimitrakopoulos, D. Kim, J. Pike, S. Elangovan, E. D. Gomez and B. Yildiz, *Nat. Commun.*, 2023, **14**, 7203.

376 J. Pan, Y. Ye, M. Zhou, X. Sun and Y. Chen, *Energy Fuels*, 2022, **36**, 12253–12260.

377 W. Sun, Z. Shi, M. Liu, L. Bi and W. Liu, *Adv. Funct. Mater.*, 2014, **24**, 5695–5702.

378 L. Bi, S. Zhang, L. Zhang, Z. Tao, H. Wang and W. Liu, *Int. J. Hydrogen Energy*, 2009, **34**, 2421–2425.

379 Y. Ma, L. Zhang, K. Zhu, B. Zhang, R. Peng, C. Xia and L. Huang, *Nano Res.*, 2023, **17**, 407–415.

380 R. Murphy, Y. Zhou, L. Zhang, L. Soule, W. Zhang, Y. Chen and M. Liu, *Adv. Funct. Mater.*, 2020, **30**, 2002265.

381 T. Nagai, W. Ito and T. Sakon, *Solid State Ionics*, 2007, **177**, 3433–3444.

382 Y. Gao, M. Fu, S. Zhao, Z. Hou, K. Liu, X. Deng and Z. Tao, *Adv. Funct. Mater.*, 2025, **35**, 2416625.

383 Y. Niu, Y. Zhou, W. Lv, Y. Chen, Y. Zhang, W. Zhang, Z. Luo, N. Kane, Y. Ding, L. Soule, Y. Liu, W. He and M. Liu, *Adv. Funct. Mater.*, 2021, **31**, 2100034.

384 Y. Chen, Y. Choi, S. Yoo, Y. Ding, R. Yan, K. Pei, C. Qu, L. Zhang, I. Chang, B. Zhao, Y. Zhang, H. Chen, Y. Chen, C. Yang, B. deGlee, R. Murphy, J. Liu and M. Liu, *Joule*, 2018, **2**, 938–949.

385 G. Li, Y. Zhang, Y. Ling, B. He, J. Xu and L. Zhao, *Int. J. Hydrogen Energy*, 2016, **41**, 5074–5083.

386 D. Ding, W. Zhu, J. Gao and C. Xia, *J. Power Sources*, 2008, **179**, 177–185.

387 Z. Zhan, D. M. Bierschenk, J. S. Cronin and S. A. Barnett, *Energy Environ. Sci.*, 2011, **4**, 3951.

388 Y. Namgung, J. Hong, A. Kumar, D.-K. Lim and S.-J. Song, *Appl. Catal., B*, 2020, **267**, 118374.

389 J. A. Schuler, H. Yokokawa, C. F. Calderone, Q. Jeangros, Z. Wuillemin and A. Hessler-Wyser, *J. Power Sources*, 2012, **201**, 112–120.

390 L. Zhou, J. H. Mason, W. Li and X. Liu, *Renewable Sustainable Energy Rev.*, 2020, **134**, 110320.

391 B. Wei, M. Schroeder and M. Martin, *ACS Appl. Mater. Interfaces*, 2018, **10**, 8621–8629.

392 S. B. Adler, *Chem. Rev.*, 2004, **104**, 4791–4844.

4592 | *Energy Environ. Sci.*, 2025, **18**, 4555–4595

This journal is © The Royal Society of Chemistry 2025

393 W. Lee, J. W. Han, Y. Chen, Z. Cai and B. Yildiz, *J. Am. Chem. Soc.*, 2013, **135**, 7909–7925.

394 Z. Zhuang, Y. Li, R. Yu, L. Xia, J. Yang, Z. Lang, J. Zhu, J. Huang, J. Wang, Y. Wang, L. Fan, J. Wu, Y. Zhao, D. Wang and Y. Li, *Nat. Catal.*, 2022, **5**, 300–310.

395 W. Wu, H. Ding, Y. Zhang, Y. Ding, P. Katiyar, P. K. Majumdar, T. He and D. Ding, *Adv. Sci.*, 2018, **5**, 1800360.

396 F. Liu, H. Deng, D. Diercks, P. Kumar, M. H. A. Jabbar, C. Gumeci, Y. Furuya, N. Dale, T. Oku, M. Usuda, P. Kazempoor, L. Fang, D. Chen, B. Liu and C. Duan, *Nat. Energy*, 2023, **8**, 1145–1157.

397 D. Chen, R. Ran and Z. Shao, *J. Power Sources*, 2010, **195**, 4667–4675.

398 S. Im, J.-H. Lee and H.-I. Ji, *J. Korean Ceram. Soc.*, 2021, **58**, 351–358.

399 A. Seong, D. Jeong, M. Kim, S. Choi and G. Kim, *J. Power Sources*, 2022, **530**, 231241.

400 S. J. Yang, W. Chang, H. J. Jeong, D. H. Kim and J. H. Shim, *Int. J. Energy Res.*, 2021, **46**, 6553–6561.

401 J. S. Park, H. J. Choi, G. D. Han, J. Koo, E. H. Kang, D. H. Kim, K. Bae and J. H. Shim, *J. Power Sources*, 2021, **482**, 229043.

402 H. S. Park, H. J. Jeong, K.-H. Kim, W. Chang, Y. S. Kim, Y. S. Choi and J. H. Shim, *Appl. Surf. Sci.*, 2023, **612**, 155812.

403 W. Tang, H. Ding, W. Bian, W. Wu, W. Li, X. Liu, J. Y. Gomez, C. Y. Regalado Vera, M. Zhou and D. Ding, *J. Mater. Chem. A*, 2020, **8**, 14600–14608.

404 M. Choi, J. Paik, D. Kim, D. Woo, J. Lee, S. J. Kim, J. Lee and W. Lee, *Energy Environ. Sci.*, 2021, **14**, 6476–6483.

405 S. Bang, J. Lee and W. Lee, *J. Power Sources*, 2023, **553**, 232290.

406 J. Lee, S. Hwang, M. Ahn, M. Choi, S. Han, D. Byun and W. Lee, *J. Mater. Chem. A*, 2019, **7**, 21120–21127.

407 S. Choi, T. C. Davenport and S. M. Haile, *Energy Environ. Sci.*, 2019, **12**, 206–215.

408 J. Suntivich, H. A. Gasteiger, N. Yabuuchi, H. Nakanishi, J. B. Goodenough and Y. Shao-Horn, *Nat. Chem.*, 2011, **3**, 546–550.

409 J. Suntivich, K. J. May, H. A. Gasteiger, J. B. Goodenough and Y. Shao-Horn, *Science*, 2011, **334**, 1383–1385.

410 L. Wang, K. A. Stoerzinger, L. Chang, J. Zhao, Y. Li, C. S. Tang, X. Yin, M. E. Bowden, Z. Yang, H. Guo, L. You, R. Guo, J. Wang, K. Ibrahim, J. Chen, A. Rusydi, J. Wang, S. A. Chambers and Y. Du, *Adv. Funct. Mater.*, 2018, **28**, 1803712.

411 D. Chen, F. Wang, H. Shi, R. Ran and Z. Shao, *Electrochim. Acta*, 2012, **78**, 466–474.

412 H. Ding and X. Xue, *J. Power Sources*, 2010, **195**, 7038–7041.

413 H. Ding and X. Xue, *J. Power Sources*, 2010, **195**, 4139–4142.

414 Q. Yang, M. Chen, B. S. Teketel, D. Tian, Y. Ding, X. Lu, S. Zhu, Y. Chen and B. Lin, *J. Alloys Compd.*, 2022, **918**, 165368.

415 C. Wen, K. Chen, D. Guo, W. Yang, S. Gao, C. Lu, B. Niu and B. Wang, *Solid State Ionics*, 2022, **386**, 116048.

416 L. Wang, P. Xie, L. Bian, X. Liu and K. Chou, *Catal. Today*, 2018, **318**, 132–136.

417 B. Zhang, Y. Wan, Z. Hua, K. Tang and C. Xia, *ACS Appl. Energy Mater.*, 2021, **4**, 8401–8409.

418 C. Liu, F. Wang, Y. Ni, S. Wang, B. Qian, Q. Ni, Y. Zheng, H. Chen and L. Ge, *Int. J. Hydrogen Energy*, 2023, **48**, 9812–9822.

419 X. Mao, W. Wang and G. Ma, *Ceram. Int.*, 2015, **41**, 10276–10280.

420 H.-X. Zhang, J.-X. Yang, P.-F. Wang, C.-G. Yao, X.-D. Yu and F.-N. Shi, *Solid State Ionics*, 2023, **391**, 116144.

421 M. Zhang, Z. Du, Z. Sun and H. Zhao, *J. Mater. Chem. A*, 2023, **11**, 21645–21654.

422 A. Montenegro-Hernandez, J. Vega-Castillo, L. Mogni and A. Caneiro, *Int. J. Hydrogen Energy*, 2011, **36**, 15704–15714.

423 A. Tarancón, S. J. Skinner, R. J. Chater, F. Hernández-Ramírez and J. A. Kilner, *J. Mater. Chem.*, 2007, **17**, 3175.

424 J. M. Bassat, P. Odier, A. Villesuzanne, C. Marin and M. Pouchard, *Solid State Ionics*, 2004, **167**, 341–347.

425 D. Zhu, J. Yu, Y. Zhang, J. Liu, Y. Ouyang, J. Yu, Z. Liu, W. Fan, X. Bai, N. Wang, E. Bu and C. Zhu, *Int. J. Hydrogen Energy*, 2024, **92**, 1401–1408.

426 A. P. Tarutin, J. G. Lyagaeva, D. A. Medvedev, L. Bi and A. A. Yaremchenko, *J. Mater. Chem. A*, 2021, **9**, 154–195.

427 P. Zhong, K. Toyoura, L. Jiang, L. Chen, S. A. Ismail, N. Hatada, T. Norby and D. Han, *Adv. Energy Mater.*, 2022, **12**, 2200392.

428 M. Yashima, M. Enoki, T. Wakita, R. Ali, Y. Matsushita, F. Izumi and T. Ishihara, *J. Am. Chem. Soc.*, 2008, **130**, 2762–2763.

429 P. Kumar, N. K. Singh, G. Gupta and P. Singh, *RSC Adv.*, 2016, **6**, 22094–22102.

430 P. Kumar, P. Jena, P. K. Patro, R. K. Lenka, A. S. K. Sinha, P. Singh and R. K. Singh, *ACS Appl. Mater. Interfaces*, 2019, **11**, 24659–24667.

431 Y. Watanabe, Y. Hiruma, H. Nagata and T. Takenaka, *Ceram. Int.*, 2008, **34**, 761–764.

432 K. Koyama, T. Tange, T. Saito and K. Mizuno, *Phys. B*, 2000, **281–282**, 909–911.

433 Z. Wang, X. Miao, X. Zhu, S. Guo, D. Han, X. Ye and Z. Wen, *J. Power Sources*, 2024, **597**, 234141.

434 Y. Ling, T. Guo, Y. Guo, Y. Yang, Y. Tian, X. Wang, X. Ou and P. Feng, *J. Adv. Ceram.*, 2021, **10**, 1052–1060.

435 S. Yang, Y. Wen, J. Zhang, Y. Lu, X. Ye and Z. Wen, *Electrochim. Acta*, 2018, **267**, 269–277.

436 Q. Cao, R. Qiu, L. Lei, W. Zhang, S. Deng, J. Chen, L. He and J. Xu, *ACS Appl. Energy Mater.*, 2022, **5**, 11213–11222.

437 Z. Yang, J. Zhang, B. Wu, X. Zhao, X. Lu, Y. Zhao and Y. Li, *Ceram. Int.*, 2023, **49**, 25381–25388.

438 P. Batocchi, F. Mauvy, S. Fourcade and M. Parco, *Electrochim. Acta*, 2014, **145**, 1–10.

439 M. Laguna-Bercero, H. Monzón, A. Larrea and V. Orera, *J. Mater. Chem. A*, 2016, **4**, 1446–1453.

440 C. Lalanne, F. Mauvy, E. Siebert, M. L. Fontaine, J. M. Bassat, F. Ansart, P. Stevens and J. C. Grenier, *J. Eur. Ceram. Soc.*, 2007, **27**, 4195–4198.

441 E. Boehm, J. Bassat, P. Dordor, F. Mauvy, J. Grenier and P. Stevens, *Solid State Ionics*, 2005, **176**, 2717–2725.

442 C. Lalanne, G. Prosperi, J. Bassat, F. Mauvy, S. Fourcade, P. Stevens, M. Zahid, S. Diethelm, J. Vanherle and J. Grenier, *J. Power Sources*, 2008, **185**, 1218–1224.

This journal is © The Royal Society of Chemistry 2025

Energy Environ. Sci., 2025, **18**, 4555–4595 | **4593**

443 J. Wan, J. Goodenough and J. Zhu, *Solid State Ionics*, 2007, **178**, 281–286.

444 A. P. Tarutin, M. Y. Gorshkov, I. N. Bainov, G. K. Vdovin, A. I. Vylkov, J. G. Lyagaeva and D. A. Medvedev, *Ceram. Int.*, 2020, **46**, 24355–24364.

445 A. P. Khandale, J. D. Punde and S. S. Bhoga, *J. Solid State Electrochem.*, 2012, **17**, 617–626.

446 T. Nakamura, K. Yashiro, K. Sato and J. Mizusaki, *Solid State Ionics*, 2010, **181**, 402–411.

447 H. G. Seo, H. Kim, W. Jung and H. L. Tuller, *Appl. Catal., B*, 2024, **355**, 124172.

448 S. Choi, S. Park, J. Shin and G. Kim, *J. Mater. Chem. A*, 2015, **3**, 6088–6095.

449 S. Ingavale, M. Gopalakrishnan, C. M. Enoch, C. Pornrungroj, M. Rittiruam, S. Praserthdam, A. Somwangthanaroj, K. Nootong, R. Pornprasertsuk and S. Kheawhom, *Small*, 2024, **20**, 2308443.

450 Y. Zhu, Q. Lin, Z. Hu, Y. Chen, Y. Yin, H. A. Tahini, H. J. Lin, C. T. Chen, X. Zhang, Z. Shao and H. Wang, *Small*, 2020, **16**, 2001204.

451 X. Xu, Y. Pan, L. Ge, Y. Chen, X. Mao, D. Guan, M. Li, Y. Zhong, Z. Hu, V. K. Peterson, M. Saunders, C. T. Chen, H. Zhang, R. Ran, A. Du, H. Wang, S. P. Jiang, W. Zhou and Z. Shao, *Small*, 2021, **17**, 2101573.

452 M. B. Liu and B. Yildiz, *Chem. Mater.*, 2024, **36**, 10571–10582.

453 H. G. Seo, A. Staerz, D. S. Kim, D. Klotz, C. Nicollet, M. Xu, J. M. LeBeau and H. L. Tuller, *Energy Environ. Sci.*, 2022, **15**, 4038–4047.

454 H. G. Seo, A. Staerz, D. S. Kim, J. M. LeBeau and H. L. Tuller, *Adv. Mater.*, 2023, **35**, 2208182.

455 Y. Chen, S. Yoo, X. Li, D. Ding, K. Pei, D. Chen, Y. Ding, B. Zhao, R. Murphy, B. deGlee, J. Liu and M. Liu, *Nano Energy*, 2018, **47**, 474–480.

456 M. Perz, E. Bucher, C. Gspan, J. Waldhäusl, F. Hofer and W. Sitte, *Solid State Ionics*, 2016, **288**, 22–27.

457 S. P. Jiang, J. P. Zhang and X. G. Zheng, *J. Eur. Ceram. Soc.*, 2002, **22**, 361–373.

458 Y. Zhen, *Solid State Ionics*, 2008, **179**, 1459–1464.

459 J. Hong, S. J. Heo, A. N. Aphale, B. Hu and P. Singh, *J. Electrochem. Soc.*, 2019, **166**, F59–F65.

460 B.-K. Park, R.-H. Song, S.-B. Lee, T.-H. Lim, S.-J. Park, W. Jung and J.-W. Lee, *J. Power Sources*, 2017, **348**, 40–47.

461 J. Huang, Q. Liu, S. P. Jiang, L. Zhao, N. Ai, X. Wang, Y. Shao, C. Guan, H. Fang, Y. Luo and K. Chen, *Appl. Catal., B*, 2023, **321**, 122080.

462 H. A. Ishfaq, M. Z. Khan, Y. M. Shirke, S. Qamar, A. Hussain, M. T. Mehran, R.-H. Song and M. Saleem, *Appl. Catal., B*, 2023, **323**, 122178.

463 Y. Chen, W. Zhou, D. Ding, M. Liu, F. Ciucci, M. Tade and Z. Shao, *Adv. Energy Mater.*, 2015, **5**, 1500537.

464 Y. Li, W. Zhang, Y. Zheng, J. Chen, B. Yu, Y. Chen and M. Liu, *Chem. Soc. Rev.*, 2017, **46**, 6345–6378.

465 Y. Chen, Y. Choi, S. Yoo, Y. Ding, R. Yan, K. Pei, C. Qu, L. Zhang, I. Chang and B. Zhao, *Joule*, 2018, **2**, 938–949.

466 S. J. Kim, T. Akbay, J. Matsuda, A. Takagaki and T. Ishihara, *ACS Appl. Energy Mater.*, 2019, **2**, 1210–1220.

467 R. Zhang and G. Azimi, *Ind. Eng. Chem. Res.*, 2023, **62**, 13117–13132.

468 M. S. I. Sozal, W. Tang, S. Das, W. Li, A. Durygin, V. Drozd, C. Zhang, B. Jafarizadeh, C. Wang and A. Agarwal, *Int. J. Hydrogen Energy*, 2022, **47**, 21817–21827.

469 Z. Zhang, C. Yao, H. Zhang, Y. Sun, B. Xia, W. Liu, J. Ding, L. Zhang, X. Lang and K. Cai, *ACS Sustainable Chem. Eng.*, 2025, **13**, 3234–3246.

470 G. Pacchioni, *Nat. Rev. Mater.*, 2022, **7**, 751.

471 Z. Luo, X. Hu, Y. Zhou, Y. Ding, W. Zhang, T. Li and M. Liu, *Adv. Mater.*, 2024, **36**, 2311159.

472 J. Wei, X. Chu, X. Y. Sun, K. Xu, H. X. Deng, J. Chen, Z. Wei and M. Lei, *InfoMat*, 2019, **1**, 338–358.

473 G. H. Gu, C. Choi, Y. Lee, A. B. Situmorang, J. Noh, Y. H. Kim and Y. Jung, *Adv. Mater.*, 2020, **32**, 1907865.

474 M. Zhong, K. Tran, Y. Min, C. Wang, Z. Wang, C.-T. Dinh, P. De Luna, Z. Yu, A. S. Rasouli, P. Brodersen, S. Sun, O. Voznyy, C.-S. Tan, M. Askerka, F. Che, M. Liu, A. Seifitokaldani, Y. Pang, S.-C. Lo, A. Ip, Z. Ulissi and E. H. Sargent, *Nature*, 2020, **581**, 178–183.

475 Y. Chen, Y. Huang, T. Cheng and W. A. Goddard, 3rd, *J. Am. Chem. Soc.*, 2019, **141**, 11651–11657.

476 K. H. Tu, H. Huang, S. Lee, W. Lee, Z. Sun, A. Alexander-Katz and C. A. Ross, *Adv. Mater.*, 2020, **32**, 2005713.

477 C. Rao and Y. Liu, *Comput. Mater. Sci.*, 2020, **184**, 109850.

478 K. Choudhary and B. DeCost, *npj Comput. Mater.*, 2021, **7**, 185.

479 J. Schmidt, M. R. G. Marques, S. Botti and M. A. L. Marques, *npj Comput. Mater.*, 2019, **5**, 83.

480 A. Chen, X. Zhang and Z. Zhou, *InfoMat*, 2020, **2**, 553–576.

481 N. Wang, B. Yuan, C. Tang, L. Du, R. Zhu, Y. Aoki, W. Wang, L. Xing and S. Ye, *Adv. Mater.*, 2022, **34**, 2203446.

482 A. M. Deml, V. Stevanović, C. L. Muhich, C. B. Musgrave and R. O'Hayre, *Energy Environ. Sci.*, 2014, **7**, 1996.

483 R. B. Wexler, G. S. Gautam, E. B. Stechel and E. A. Carter, *J. Am. Chem. Soc.*, 2021, **143**, 13212–13227.

484 Y.-L. Lee, J. Kleis, J. Rossmeisl and D. Morgan, *Phys. Rev. B: Condens. Matter Mater. Phys.*, 2009, **80**, 224101.

485 M. T. Curnan and J. R. Kitchin, *J. Phys. Chem. C*, 2014, **118**, 28776–28790.

486 W. Li, R. Jacobs and D. Morgan, *Comput. Mater. Sci.*, 2018, **150**, 454–463.

487 S. Nie, Y. Xiang, L. Wu, G. Lin, Q. Liu, S. Chu and X. Wang, *J. Am. Chem. Soc.*, 2024, **146**, 29325–29334.

488 A. Talapatra, B. P. Uberuaga, C. R. Stanek and G. Pilania, *Chem. Mater.*, 2021, **33**, 845–858.

489 K. Yang, J. Liu, Y. Wang, X. Shi, J. Wang, Q. Lu, F. Ciucci and Z. Yang, *J. Mater. Chem. A*, 2022, **10**, 23683–23690.

490 A. K. Padinjarethil, S. Pollok and A. Hagen, *Fuel Cells*, 2021, **21**, 566–576.

491 X. Li, Z. Chen, D. Huan, B. Qiu, K. Zhu, Z. Qi, H. Liu, C. Xia, R. Peng and Y. Lu, *ACS Mater. Lett.*, 2023, **5**, 2896–2905.

492 K. Saito and M. Yashima, *Nat. Commun.*, 2023, **14**, 7466.

493 F. He, F. Zhu, D. Liu, Y. Zhou, K. Sasaki, Y. Choi, M. Liu and Y. Chen, *Mater. Today*, 2023, **63**, 89–98.

4594 | *Energy Environ. Sci.*, 2025, **18**, 4555–4595

This journal is © The Royal Society of Chemistry 2025

494 Z. Sun, Z. Shen, Z. Du, Y. Zhang, Y. Gong, M. Zhang, K. Wang, K. Świerczek, J. Zeng and H. Zhao, *Adv. Funct. Mater.*, 2024, **34**, 2403312.

495 R. Jacobs, J. Hwang, Y. Shao-Horn and D. Morgan, *Chem. Mater.*, 2019, **31**, 785–797.

496 L. Tang, Y. Yang, H. Guo, Y. Wang, M. Wang, Z. Liu, G. Yang, X. Fu, Y. Luo, C. Jiang, Y. Zhao, Z. Shao and Y. Sun, *Adv. Funct. Mater.*, 2022, **32**, 2112157.

497 Y. Choi, M. C. Lin and M. Liu, *J. Power Sources*, 2010, **195**, 1441–1445.

498 Z. W. Seh, J. Kibsgaard, C. F. Dickens, I. Chorkendorff, J. K. Norskov and T. F. Jaramillo, *Science*, 2017, **355**, 146.

499 T. Chen, G. Zhang, K. Liu, C. Wang, G. Zheng, Z. Huang, N. Sun, L. Xu, J. Zhou, Y. Zhou and S. Wang, *Adv. Funct. Mater.*, 2024, **34**, 2316485.

500 A. P. Tarutin, J. G. Lyagaeva, D. A. Medvedev, L. Bi and A. A. Yaremchenko, *J. Mater. Chem. A*, 2021, **9**, 154–195.

501 R. K. Lenka, P. K. Patro, V. Patel, L. Muhmood and T. Mahata, *J. Alloys Compd.*, 2021, **860**, 158490.

502 N. Yu, I. T. Bello, X. Chen, T. Liu, Z. Li, Y. Song and M. Ni, *Nano-Micro Lett.*, 2024, **16**, 177.

503 X. Li, Z. Chen, Y. Yang, D. Huan, H. Su, K. Zhu, N. Shi, Z. Qi, X. Zheng, H. Pan, Z. Zhan, C. Xia, R. Peng, S. Wei and Y. Lu, *Appl. Catal., B*, 2022, **316**, 121627.

504 Q. Hassan, P. Viktor, T. J. Al-Musawi, B. M. Ali, S. Algburi, H. M. Alzoubi, A. K. Al-Jiboory, A. Z. Sameen, H. M. Salman and M. Jaszczur, *Renewable Energy Focus*, 2024, **48**, 100545.

505 https://www.renews.biz/96664/european-energy-opens-first-green-hydrogen-plant/.

506 https://energynews.pro/en/totalenergies-and-morocco-launch-green-hydrogen-production-project-for-the-european-market/.

507 https://www.offshore-energy.biz/germany-opens-test-field-for-hydrogen-fuel-cell-propulsion-systems/.

508 A. Hauch, R. Küngas, P. Blennow, A. B. Hansen, J. B. Hansen, B. V. Mathiesen and M. B. Mogensen, *Science*, 2020, **370**, eaba6118.

509 M. Tsuchiya, B.-K. Lai and S. Ramanathan, *Nat. Nanotechnol.*, 2011, **6**, 282–286.

510 S. Robinson, A. Manerbino, W. Grover Coors and N. Sullivan, *Fuel Cells*, 2013, **13**, 584–591.

511 M. Li, J. Wang, Z. Chen, X. Qian, C. Sun, D. Gan, K. Xiong, M. Rao, C. Chen and X. Li, *Energies*, 2024, **17**, 1005.

512 S. Pirou, Q. Wang, P. Khajavi, X. Georgolamprou, S. Ricote, M. Chen and R. Kiebach, *Int. J. Hydrogen Energy*, 2022, **47**, 6745–6754.

513 H. An, H.-W. Lee, B.-K. Kim, J.-W. Son, K. J. Yoon, H. Kim, D. Shin, H.-I. Ji and J.-H. Lee, *Nat. Energy*, 2018, **3**, 870–875.

514 R. J. Braun, A. Dubois, K. Ferguson, C. Duan, C. Karakaya, R. J. Kee, H. Zhu, N. P. Sullivan, E. Tang and M. Pastula, *ECS Trans.*, 2019, **91**, 997.

515 L. Q. Le, C. H. Hernandez, M. H. Rodriguez, L. Zhu, C. Duan, H. Ding, R. P. O'Hayre and N. P. Sullivan, *J. Power Sources*, 2021, **482**, 228868.

516 J. Dailly and M. Marrony, *J. Power Sources*, 2013, **240**, 323–327.

517 S. Nien, C. Hsu, C. Chang and B. Hwang, *Fuel Cells*, 2011, **11**, 178–183.

518 A. R. Hanifi, N. K. Sandhu, T. H. Etsell, J.-L. Luo and P. Sarkar, *J. Power Sources*, 2017, **341**, 264–269.

519 T. Amiri, K. Singh, N. K. Sandhu, A. R. Hanifi, T. H. Etsell, J.-L. Luo, V. Thangadurai and P. Sarkar, *J. Electrochem. Soc.*, 2018, **165**, F764.

520 C. Chen, Y. Dong, L. Li, Z. Wang, M. Liu, B. H. Rainwater and Y. Bai, *J. Electroanal. Chem.*, 2019, **844**, 49–57.

521 D. Cao, M. Zhou, X. Yan, Z. Liu and J. Liu, *Electrochem. Commun.*, 2021, **125**, 106986.

522 Y. Pan, H. Zhang, K. Xu, Y. Zhou, B. Zhao, W. Yuan, K. Sasaki, Y. Choi, Y. Chen and M. Liu, *Appl. Catal., B*, 2022, **306**, 121071.

523 R. I. Walton, *Chem. – Eur. J.*, 2020, **26**, 9041–9069.

524 K.-Y. Park, Y. Seo, K. B. Kim, S.-J. Song, B. Park and J.-Y. Park, *J. Alloys Compd.*, 2015, **639**, 435–444.

525 L. Vradman, E. Friedland, J. Zana, R. Vidruk-Nehemya and M. Herskowitz, *J. Mater. Sci.*, 2017, **52**, 11383–11390.

526 D. Navas, S. Fuentes, A. Castro-Alvarez and E. Chavez-Angel, *Gels*, 2021, **7**, 275.

527 S. Sharma, V. Singh, R. Kotnala and R. K. Dwivedi, *J. Mater. Sci.: Mater. Electron.*, 2014, **25**, 1915–1921.

528 R. R. Suresh, M. Lakshmanakumar, J. Arockia Jayalatha, K. Rajan, S. Sethuraman, U. M. Krishnan and J. B. B. Rayappan, *J. Mater. Sci.*, 2021, **56**, 8951–9006.

529 X. Gao, S. Zhang, P. Wang, M. Jaroniec, Y. Zheng and S.-Z. Qiao, *Chem. Soc. Rev.*, 2024, **53**, 1552–1591.

530 G. Liu, W. Zhao, Z. Li, Z. Xia, C. Jiang, J. Kupecki, S. Pang, Z. Deng and X. Li, *Energy Convers. Manage.*, 2022, **255**, 115318.

531 G. Liu, Z. Wang, X. Liu, J. Kupecki, D. Zhao, B. Jin, Z. Wang and X. Li, *J. Cleaner Prod.*, 2023, **425**, 139000.

532 M. Mogensen, M. Chen, H. Frandsen, C. Graves, J. Hansen, K. Hansen, A. Hauch, T. Jacobsen, S. Jensen and T. Skafte, *Clean Energy*, 2019, **3**, 175–201.

533 G. Yang, C. Su, H. Shi, Y. Zhu, Y. Song, W. Zhou and Z. Shao, *Energy Fuels*, 2020, **34**, 15169–15194.

534 D. Nath, Ankit, D. R. Neog and S. S. Gautam, *Arch. Comput. Methods Eng.*, 2024, 1–40.

535 B. Timurkutluk and E. Ucar, *J. Power Sources*, 2025, **625**, 235715.

536 H. Sun, X. Xu, H. Kim, W. Jung, W. Zhou and Z. Shao, *Energy Environ. Mater.*, 2023, **6**, e12441.

This journal is © The Royal Society of Chemistry 2025

Energy Environ. Sci., 2025, **18**, 4555–4595 | **4595**